NOTE TO USERS

This reproduction is the best copy available.

RIGID-PLASTIC IMPACT OF SINGLE ANGULAR PARTICLES

By

Sandeep Dhar

Bachelor of Engineering (Mechanical)
Karnatak University, India, 2000

A thesis
Presented to Ryerson University
In Partial Fulfillment of the
Requirements for the Degree of
Master of Applied Science
In the program of
Mechanical Engineering

Toronto, Ontario, Canada, 2004

BORROWER'S PAGE

Ryerson University requires the signature of all the persons using or photocopying this thesis. Please sign below, and give address and date.

NAME	ADDRESS	DATE

ABSTRACT

RIGID-PLASTIC IMPACT OF SINGLE ANGULAR PARTICLES

Master of Applied Science
In the program of Mechanical Engineering
Ryerson University,Toronto

The trajectory of an angular particle as it cuts a ductile target is, in general, complicated because of its dependence not only on particle shape, but also on particle orientation at the initial instant of impact. This orientation dependence has also made experimental measurement of impact parameters of single angular particles very difficult, resulting in a relatively small amount of available experimental data in the literature. The current work is focused on obtaining measurements of particle kinematics for comparison to rigid plastic model developed by Papini and Spelt. Fundamental mechanisms of material removal are identified, and measurements of rebound parameters and corresponding crater dimensions of single hardened steel particles launched against flat aluminum alloy targets are presented. Also a 2-D finite element model is developed and a dynamic analysis is performed to predict the erosion mechanism. Overall, a good agreement was found among the experimental results, rigid-plastic model predictions and finite element model predictions.

ACKNOWLEDGEMENTS

I would like to take this opportunity to thank my supervisor, Dr. Marcello Papini for his support, trust, guidance, motivation, ideas and above all, generosity throughout the research. His qualities of intelligence, encouragement, friendliness and teamwork make him the ideal supervisor. 'Certainly, it's not the ability of a person that makes people trust in him but it's the trust of people that makes a person able.' I consider myself extremely lucky to have such an able mentor. Thank you, Marcello!

Thanks are also due to all my friends and colleagues in the lab over the years. Everyone has helped me at one time or another. I would like to especially thank, in particular, David Ciampini for helping with the catapult design, and Tom Krajac and George Barbuc for helping with the experiments.

I would also like to thank the Natural Sciences and Engineering Research Council of Canada, and Ryerson University for financial support.

Finally, I am grateful to my parents and sister for their motivation, support and encouragement during this work.

Maa, Baba, Didi, and to my God 'Sai'

TABLE OF CONTENTS

LIST OF TABLES

LIST OF FIGURES

NOMENCLATURE

Due to large number of variables used in this thesis and to comply with the standard conventions used in the literature, it was necessary to occasionally use the same variables in different contexts. To avoid confusion, the nomenclature has been divided into that used in each chapter.

Chapter 2

a,b.....	exponent defining type of particle
A.....	angularity of the particle
A_c.....	current contact area
c_r	size of the radial crack
D.....	diameter of particle
E	plastic true strain
E_a	modulus of elasticity of the target
E_r	erosion rate of the target material
F_x, F_x, F_y,.....	inertial X and Y components of the total contact force
F_{Y_L},F_{z_L},F_{Y_R},F_{Z_R}	normal forces in Y and Z directions acting on the left and right side of the particle
h.....	length of a side of the particle
k_1	constant of proportionality
k_r, A_r, B_r, C_r, n1, n2	constants having dependence on the impact conditions
m.....	mass of the particle
m_0.....	Weibul constants
M_X	total moment per unit particle thickness acting about the center of mass of the particle.
M_{X_L},M_{X_R}	moments in the *X* direction acting on left and right sides of the particle respectively
P.....	normal contact force
P_d.....	dynamic hardness of the target material
P_h.....	horizontal component of the flow pressure
p,q.....	constants for typical ductile material

r	particle size
t	time
V_x	horizontal component of the velocity
V_y	vertical component of velocity
V_i	incident velocity of the particle
W	erosion of material expressed in Weibull distribution
x,y,z	body fixed co-ordinate system
x',y',z'	coordinate system fixed at center of mass and remaining parallel to inertial coordinate system
X, Y, Z	inertial coordinate system
X_0, Y_0, Z_0	inertial co-ordinates of the center of mass of the particle
$\ddot{Y}_0, \ddot{Z}_0$	accelerations of the center of mass of the particle in the Y and Z directions
α	incident angle of attack
θ	orientation angle
θ_c	current angle of impact
$\ddot{\theta}$	angular acceleration of the particle about the X axis
σ	flow stress
σ_w	Weibul constants
φ, ψ	erosion constant
ρ	density of the particle/ball
υ	volume of material removed
Δ	depth of penetration of the particle
μ	friction coefficient

Chapter 4

A	angularity of the particle
A_{cr}	cross sectional area of the particle
h	length of a side of the particle
$i,f,$	conditions at initial (at the end of the first impact) and final (at the onset of the second impact) respectively

KE_i	incident kinetic energy of the particle
KE_{loss}	kinetic energy loss
L.....	length of the crater
m.....	mass of the particle
P.....	normal contact force
P_d	dynamic hardness of the target material
t.....	time
V_i	incident velocity of the particle
V_r	rebound velocity
w.....	width of the angular particle
x,y,z.....	body fixed co-ordinate system
x',y',z'	coordinate system fixed at center of mass and remaining parallel to inertial coordinate system
X, Y, Z.....	inertial coordinate system
X_0, Y_0, Z_0.....	inertial co-ordinates of the center of mass of the particle
Z_{ver}	Z-coordinate of the adjacent vertex
α_i, α_r.....	incident angle of attack and rebound angle respectively
θ_{adj}.....	adjusted orientation angle for secondary impact
θ_i.....	incident orientation angle of the angular particle
θ_i^{crit}	orientation angle at transition
$\dot{\theta}_i$, $\dot{\theta}_r$	incident angular velocity and rebound angular velocity respectively
θ_f	Orientation of angular particle for the secondary impact.
δ.....	depth of penetration by the angular particle into the target
δ_{max}.....	maximum depth of penetration of the particle into the target
π_1, π_2.....	dimensionless parameters
ρ.....	density of the particle
μ.....	friction coefficient

Chapter 5

A.....	angularity of the particle
h.....	length of a side of the particle

KE_i	incident kinetic energy of the particle
KE_{loss}	kinetic energy loss
L	length of the crater
P_d	dynamic hardness of the target material
t	time
V_i	incident velocity of the particle
V_r	rebound velocity
w	width of the angular particle
X, Y, Z	inertial coordinate system
α_i, α_r	incident angle of attack and rebound angle respectively
θ_i	incident orientation angle of the angular particle
θ_i^{crit}	orientation angle at transition
θ_{adj}	adjusted orientation angle for secondary impact
$\dot{\theta}_i$, $\dot{\theta}_r$	incident angular velocity and rebound angular velocity respectively
δ	depth of penetration by the angular particle into the target
π_1, π_2	dimensionless parameters
ρ	density of the particle
μ	friction coefficient
ε_f	failure strain
σ	flow stress
σ_0	yield stress

Chapter-1

Introduction

1.1. Motivation

Solid particle impact, erosion-corrosion, and liquid drop impact can all result in target material loss due to erosion, but the mechanism of solid particle erosion is of particular interest due to its application in a wide variety of industrial processes. Erosion due to the impact of solid particles can either be constructive (material removal desirable) or destructive (material removal undesirable), and therefore, it can either be desirable to minimize or maximize erosion, depending on the application.

Constructive applications include sand blasting, high-speed water-jet cutting, blast stripping of paint from aircraft and automobiles, blasting to remove the adhesive flash from bonded parts, erosive drilling of hard materials, and most recently, in the micro-mechanical etching (abrasive jet micromachining) of Si and glass substrates for opto-electronic applications, and the fabrication of components for MEMS and micro-fluidic applications. Solid particle erosion is destructive in industrial applications such as erosion of machine parts, surface degradation of steam turbine blades, erosion of pipelines carrying slurries, and particle erosion in fluidized bed combustion systems. For these reasons, the understanding of fundamental erosion mechanisms (i.e. the mechanisms by which the target material is removed) is of great interest.

The fundamental understanding of the mechanism of material removal due to the impact of particles has received a considerable amount of attention since the advent of improved measuring techniques. In the case of erosion by solid particles, the trajectory of the particle while impacting the material surface has been of prime interest in predicting the material loss on ductile targets, since this determines the manner in which a crater is carved out.

Erosion due to particle streams involves a large number of parameters that can be varied to affect the material removal for a specific target material. These include particle velocity, angle of impact (also known as angle of attack), particle concentration, shape, density, orientation (also known as rake angle) and size, along with target material properties (Young's modulus, Poisson's ratio, microstructure, hardness, and toughness). Various mechanisms including cutting, plowing, fragmentation, extrusion, elastic-plastic fracture and melting are also responsible for potential material loss. There have been analytical and semi-empirical erosion models proposed in the past (see Chapter 2, Literature Review, for a detailed treatment) that attempts to predict the amount of material removed, but these generally have restrictions in implementation.

For ductile erosion mechanisms, Hutchings [1] proposed a rigid plastic theory which was later generalized by Papini and Spelt [2, 3] for impact of particles of arbitrary shape against targets of arbitrary dynamic hardness and dynamic friction coefficient. Due to lack of available experimental data and the difficulties associated in performing angular particle experiments, the proposed model lacked, until the present work, detailed verification.

This thesis is thus motivated by a need to generate experimental data with various diamond shaped angular particles to measure impacting particle kinematics and target material loss for comparison with a computer simulation program developed by Papini, based on the rigid-plastic theory of single particle impact, so that a detailed verification of the generalized model proposed by Papini and Spelt can be made.

1.2. Thesis Objectives

As a first step to understanding how material is removed in streams of incident particles, this thesis focuses on the impact of single, diamond shaped particles of various angularities on ductile target materials. The aim of this work is to understand the fundamental erosion mechanisms for this case. The specific objectives were:

- Design and construction of an experimental apparatus capable of launching various single diamond shaped angular particles at velocities capable of eroding

the target material (Al alloy plates) and measurement of the kinematics (i.e. tumbling behaviour, rebound velocity and angle, and energy loss) of the particles, along with the size of the associated erosion craters.

- Varying the physical, mechanical and dynamic factors affecting erosion and comparing the experimental results with the computer simulation program developed by Papini, and subsequently validating the rigid-plastic model developed by Papini and Spelt.

- Identification of the fundamental mechanisms involved in erosion behaviour by single angular particles, and the prevailing nature of the erosion mechanism (i.e. ploughing, cutting, indentation).

1.3 Thesis Organization:

- Chapter 1 presents a brief introduction to the problem, and the motivations of the thesis.
- In Chapter 2, the information available in the literature about the erosion process is discussed in detail.
- Chapter 3 describes the experimental set up for conducting the single angular particle collision experiments.
- Chapter 4 describes the results and discussions of the experiments conducted to validate the generalized Rigid-Plastic theory proposed by Papini and Spelt.
- In Chapter 5 the methodology used to simulate single angular particle erosion process, and the associated particle kinematics, using finite element analysis is discussed in detail.
- Conclusions and recommendations for future work are discussed in Chapter 6.

Chapter 2

Literature Review

2.1 Single Particle Erosion

Investigators (e.g., [1-27]) in the past have attempted to model ductile and brittle erosion mechanisms in materials based on experimental results. In ductile erosion, considerable plastic deformation precedes or accompanies the material loss from the surface of the target material; whereas in the brittle erosion case, little or no plastic flow occurs, but cracks form that eventually intersect to create erosion fragments. Fig. 2.1 describes the manner in which volume removal varies with the angle of attack.

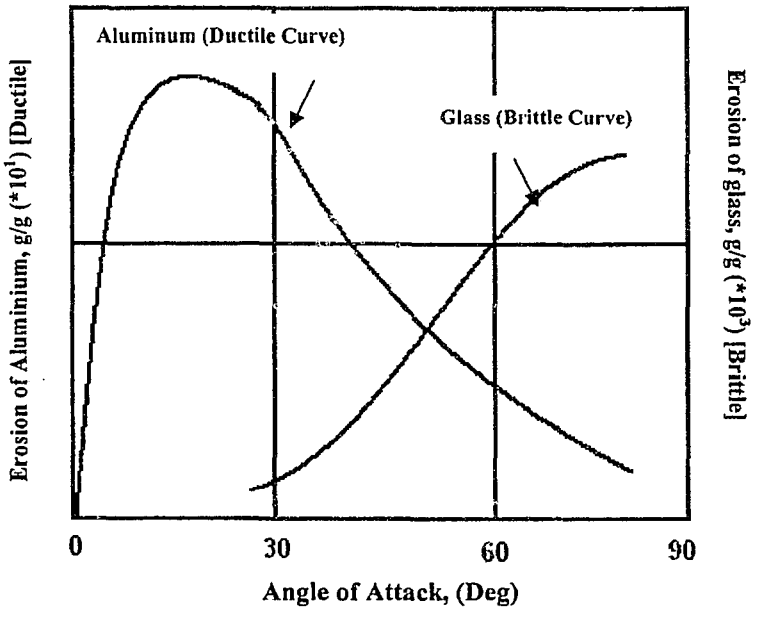

Fig.2.1: Erosion behaviour of brittle and ductile materials.
From Ref. [28].

The ductile materials show maximum volume removal for angles near 20° to 30°, in contrast to near 90° for brittle erosion. These empirical model predictions were based on the assumption that the volume of material actually removed is a result of the cumulative damage of non-interacting single particles.

2.2 Brittle Erosion Models

For systems undergoing brittle erosion, a number of investigators [4,5] have predicted erosion rates in terms of both particle (e.g. size, density, velocity etc) and target (e.g. hardness, density, fracture toughness) properties. In a brittle material, erosion rates are found to be highest for the particles impacting at higher angles of incidence (Fig. 2.1). Sheldon and Finnie [4] proposed a theory for brittle erosion, based on the assumption of Hertzian contact stresses that cause cracks to grow from pre-existing flaws in the target material during the impact. The crack propagation that occurs from the load is related to the distribution of surface flaws through the Weibull distribution. The erosion of the material (expressed in terms of grams lost per gram of impacting particle) W, is a function of the particle size r, the particle velocity V_i, and Weibull constants m_o and σ_w:

$$W=k_1 r^a V_i^{\ b} \tag{2.1}$$

The exponents a and b are given by [4]:

$a = 3(m_o - 0.67) / (m_o - 2)$ for round particles
$a = 3.6(m_o - 0.67) / (m_o - 2)$ for angular particles
$b = 2.4(m_o - 0.67) / (m_o - 2)$ for either shape

The constant k_1 is given by the expression [4]:

$$k_1=E_a^{\ 0.8(m_o+1)/(m_o-2)}\rho^{1.2(m_o-0.67)/(m_o-2)}\sigma_w^{\ -2/(m_o-2)} \tag{2.2}$$

where E_s is defined as the modulus of elasticity of the target and ρ is the density of the particle. The value of k_1 is defined for particles much stiffer than the target material.

Sheldon [6] compared experimental and theoretical values of k_1 and found reasonable agreement between theory and experiment; however, the agreement was not as good as that for the exponents, a and b. Ruff and Wiederhorn [5] developed a similar theory, except that in their theory, the erosion occurs by both crack propagation and plastic deformation of the target. They believed that lateral crack formation was the main cause of material removal during erosion and questioned the physical basis of Finnie and Sheldon model, since they assumed Hertzian crack formation. Fig. 2.2 shows the typical cracking patterns seen in brittle erosion mechanisms, as opposed to the lips/pileup of material at the edge of crater in ductile erosion mechanism (Fig. 2.3).

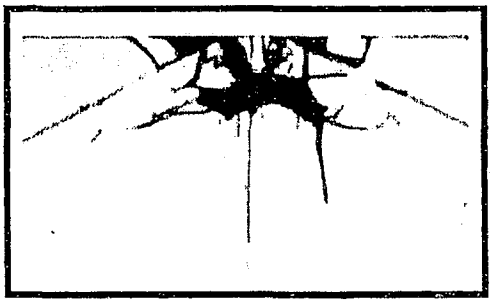

Fig. 2.2: Brittle erosion forming cracks .From Ref. [4]

The volume of material removed has been modeled by Evans, et al. [8], taking into account the lateral crack formation during erosion. The volume of material removed by each impact event is given by:

$$\upsilon \approx \pi c_r^2 \Delta \tag{2.3}$$

where the volume, υ, removed, per particle impact, is calculated from the maximum size of the lateral cracks, c_r, (i.e. the radial crack) formed during impact and the depth, Δ, of the penetration of the particle in the target material.

2.3 Ductile Erosion

Ductile erosion is characterized by plastic deformation of the target material resulting in a considerable amount of material loss from its surface. Hutchings and co-workers [1, 9-11] reported that, in ductile erosion, the particle impacts an initially stress-free surface, causing three typical modes of erosion: ploughing, and two types of cutting (Type I and Type II). In type-I cutting, the particle tumbles forward after impacting the target resulting in deep craters. In type-II cutting, the particle rotates backwards, and the impact ends in machining or cutting the target material, resulting in a long and shallow crater. The dominant mode of erosion depends on particle shape, angle of attack, and initial orientation angle; however, in erosion due to particle streams, in general, each of these modes is present, irrespective of the angle of incidence of the particle stream. This is because there is generally a rotational component of the particles that causes the effective orientation angle to be different for each impacting particle in the stream. The experiments by Hutchings revealed that, at shallow angles of attack (glancing impact), the cutting mechanisms are dominant, characterized by long and shallow craters, which are cut out of the target material (i.e. actual target material is removed by each impact).

As the incidence angle is increased, a combination of both cutting and ploughing exists. In the ploughing mechanism, the eroded material is pushed to the edge of the crater, resulting in the formation of the lips or pileups (see Fig. 2.3). At very high incidence angles, the resulting craters are deep, and large localized plastic stresses exist, causing the displaced indented material to flow to the edge of the crater in the form of lips. Actual material removal only occurs when the lips or pileups at the edge of the craters are removed by subsequent impacts.

Finnie [12, 13] considered the trajectory of an impacting particle, as it is resisted by a force, proportional to a constant flow stress multiplied by the contact area. The resulting crater was predicted by assuming that no rotation of the particle occurred throughout its trajectory while cutting the target material. A similar mechanism of metal removal was also studied in detail by Hutchings et al. [10] for impinging particles at various angles of impact, where the rotation of the particle was taken in consideration

while defining the trajectory during cutting. The material removal was assumed to be by plastic deformation, resulting in shearing of the surface layers of the target in the direction of motion of the projectile [14-16]. It was observed that, above a critical velocity, the material lip is detached from the surface of the metal by the propagation of ruptures at the base of the lip, which is a characteristic of the particular material. A similar mechanism was also seen during oblique impacts by irregularly shaped particles at small angles between the leading edge of the particle and the target surface [17].

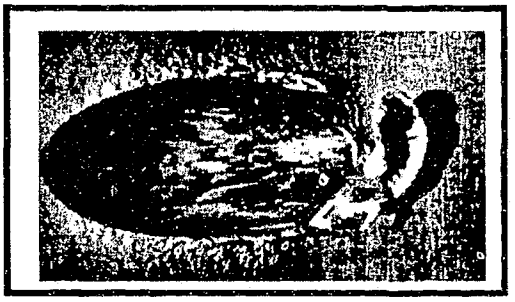

Fig. 2.3: Ductile erosion forming lips at the crater edge .From Ref. [4].

2.3.1 Rigid plastic theory

Rigid plastic erosion models have been proposed by investigators [1-3, 9-14, 16, 18] by assuming the target to be fully plastic in behaviour and the impacting particle to be rigid. This assumption has been central to all the model predictions where the elastic properties of the target are ignored in modeling ductile erosion.

2.3.1.1 Model of Finnie

Finnie's analysis [12,13] of the cutting action of a single particle launched against a ductile target was the first model of solid particle erosion capable of predicting material removal rate. In this model, erosion is considered to consist of two simultaneous processes: cutting wear and deformation wear. The phenomenon of cutting wear predominates at low angles of impact, whereas deformation wear predominates at higher angles of impact for the ductile metal.

The volume, υ, of the material removed was predicted by considering the trajectory of the tip of a single eroding particle of mass, m, which cuts the surface of the ductile metal:

$$\upsilon \approx mV_i^2 f(\alpha)/P_h \tag{2.4}$$

Where V_i is particle velocity, $f(\alpha)$, is function depending on α, the angle of attack, measured from the plane of the target surface to the particle velocity vector, and P_h is the horizontal component of the flow pressure.

In Finnie's scheme, the particles were assumed to be non-deforming and impacting a target, which was assumed to reach a constant flow pressure (i.e. the target is assumed perfectly plastic) immediately upon impact. The particle was assumed to be under the action of a resisting force vector of constant direction. By assuming that no rotations of the particle occur during the impact process, Finnie was able to solve for the trajectory of the particle in closed form as it cuts the surface, and thus predict the material removal rate.

Some of the predictions in Finnie's model have been criticized by other investigators. The model predicts the volume eroded by the particle at $\alpha<45^\circ$, but is incapable of predicting the erosion observed for the higher values of α. The theoretical treatment also tends to overestimate erosion rates, and a factor was introduced to allow for the, as stated by Hutchings [9], 'considerable proportion, perhaps 90% of the particles which do not cut in the idealized manner visualized by Finnie.' However, this theory formed the foundation for later rigid-plastic models.

A model similar to Finnie was suggested by Sheldon and Kanhare [19]. The model is based on energy balance between the kinetic energy of the particle and the work expended during the indentation. The volume of material, υ, eroded, is given as a function of the impacting particle velocity V, as well as particle diameter D, (eq.2.5);

$$\upsilon = CV^p D^q \tag{2.5}$$

Where V can be considered as the erosion wear per impacting particle. Values of the constants, p and q, for typical ductile materials, are given in Ref. [19].

2.3.1.2 Model of Hutchings

Where material removal due to impact of hard single spherical particles is concerned, a rigid-plastic theory originally developed by Hutchings and co-workers [1, 9-11] can be used to predict collision kinematics and crater dimensions for impacts on ductile targets. The theory assumes that elastic effects can be neglected, and predicts the kinematics of the particle as it ploughs through the target, under the assumption that the instantaneous resisting force can be calculated by multiplying a constant plastic flow pressure (also called the dynamic hardness) by the instantaneous contact area. Thus, the model is similar to that of Finnie, except that the contact area is permitted to change at any instant, depending on the instantaneous orientation of the particle. This theory was later improved by Rickerby and Macmillan [20], to include a more accurate calculation of contact area, and to account for the effect of pileup of material at the edge of the crater on resisting force. The modified model successfully predicted the energy absorbed during the impact and the rebound velocity (except for normal incidence), but failed to show good consistency for the shallow angles of attack. Recently, the range of application of the model was extended by Papini and Spelt to predict erosion in coated targets, by accounting for the elastic spring-back of the craters [16]. In most cases, comparisons of the theory to experiments yielded reasonable agreement.

Where impact involving single angular particles is concerned, the rigid-plastic theory is less well-developed, and lacks rigorous experimental verification. In modeling the impact of square plates with ductile targets, Hutchings [9] removed the requirement in Finnie's model [13] that particles not rotate during impact, so that the force resisting particle motion could change direction and magnitude, depending on the instantaneous contact area. Because Finnie assumed a constant force vector, this had the effect of averaging all possible orientation or rake angles (see Fig. 2.4) of the particles, and hence his model could not predict the specific tumbling behaviour (i.e. forward or backward

rotation, as reported by Hutchings) of the particles. Hutchings' rigid-plastic theory, however, could predict these effects. The resulting equations of motion of the particle, however, had to be solved numerically in time steps, but comparison with experimental measurements revealed good agreement.

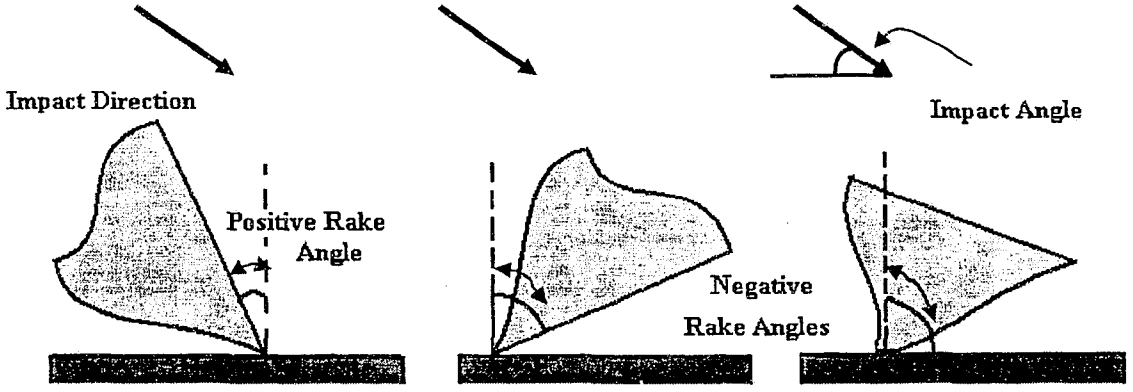

Fig.2.4: The Rake Angle defined by Hutchings is illustrated as the orientation of the particle with the surface of the target material .From Ref. [21].

2.3.1.3 Model of Sundararajan

Sundararajan [18] also used rigid plastic theory to model ductile erosion. Similar to Finnie [12,13] and Hutchings [1, 9-11], Sundararajan made an attempt to correlate the erosion resistance of metallic materials with their strength, ductility, toughness or parameters involving such properties in combinations. The main difference was the modeling of the nature and size of the plastic zone that exists beneath the eroded surface, and the possible interrelationship between the plastic zone and the erosion rate, which was not considered by both Hutchings and Finnie. He explained that the plastic zone is the primary parameter which determines the magnitude of the energy dissipated through plastic deformation during the erosion process. Additional major assumptions of the model are as follows:

a) Erosion occurs by lip extrusion and subsequent fracture.

b) Lip formation rather than fracture controls the erosion rate, and the localization of plastic deformation is responsible for lip formation.

c) The deformation of the eroding material underneath the impacting particle is adiabatic.

A good summary of the assumptions of rigid plastic theory and the ranges of applicability can be found in Ref. [22], which describes a method for characterizing the dynamic hardness of a material. Sundarajan and Shewmon [14] developed a model for the oblique impact of a hard ball against ductile target materials. According to the model (eq. 2.6), a frictional force, μ, acting on the contact surfaces is assumed to be constant and insensitive to strain, strain rate and temperature. The model also makes the assumption that the deformation of the target material due to normal and tangential forces can be treated as independent of each other, and that the total deformation is given by the superposition of the two. The contact geometries of the particle at two different time intervals, used to predict the crater area and volume, are illustrated in Fig. 2.5. Once the initial impact velocity V, current angle of impact θ_C, mass of the particle m, dynamic hardness of the target material, P_d, and the friction coefficient, μ, are specified, the numerical model (see Ref. [14]) can be used to predict the crater profile, crater volume, rebound angle ,rebound velocity, and energy absorbed during the impact. The best fit values were obtained for dynamic hardness P_d and the friction coefficient, μ from the predicted and experimental results. Unfortunately, the rigid plastic model of Sundararajan was unable to correctly predict the energy absorbed per impact, and the rebound angle of the impact.

$$\frac{dV_x}{dt} = -(\mu P_d A_c/m)\cos\gamma - (P_d A_c/m)\sin\gamma \qquad (2.6\ (a))$$

$$\frac{dV_y}{dt} = (P_d A_c/m)\cos\gamma - (\mu P_d A_c/m)\sin\gamma \qquad (2.6\ (b))$$

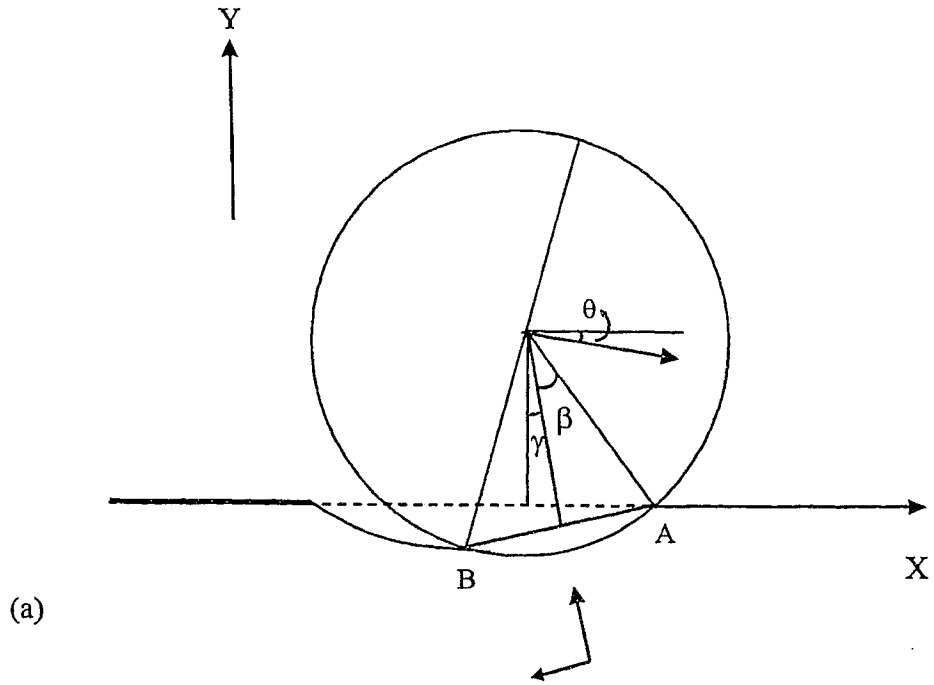

(a)

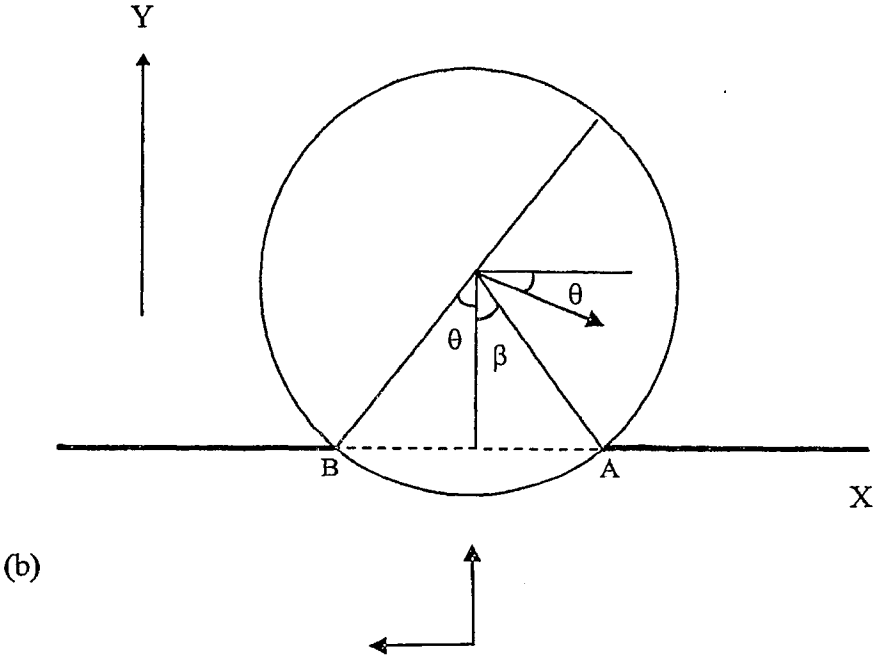

(b)

Fig. 2.5:(a) Shows the contact geometry when the ball has penetrated to a depth after time interval 't' ,(b) shows the contact geometry at an earlier time when the ball completely filled the crater

where

V_x= the horizontal component of the velocity= $V_i \cos\theta$

V_y=the vertical component of velocity = $V_i \sin\theta$

θ_c = current angle of impact; γ= angle defined in Fig. 2.5 (a)

V_i=the current velocity,

t= time

P_d=dynamic Hardness (a constant); μ= friction coefficient (a constant)

A_c=current contact area

m= mass of the ball=$4/3\pi r^3\rho$; (r=radius of the particle/ball, ρ = particle/ball density)

Plastic Deformation underneath the Impact Crater

As explained in the previous section, Sundararajan and co-workers [14, 18, 22] developed model based on the assumption that the plastic deformation directly underneath the impact site influenced the particle trajectory and crater formation. Fig. 2.6 illustrates the deformation of a plastic region underneath the impact crater by an eroding spherical particle of finite mass that leads to the formation of lips and craters. The impact site contains two distinct regions of plastic deformation.

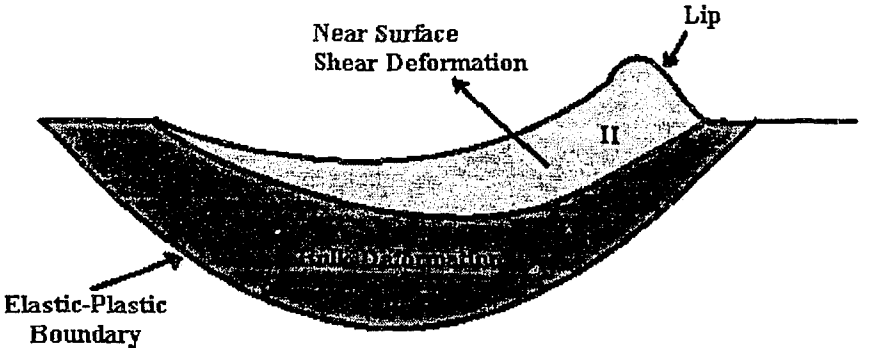

Fig. 2.6: Schematic view of the nature of plastic deformation underneath the impact crater. From Ref. [18].

Region I is the bulk deformation region, which is mainly responsible for the crater formation, and the magnitude of the strains encountered in this region is quite low (10-

20%). A similar deformation region is obtained in case of a simple quasi-static hardness test. In the region II, however, the deformation is seen as nearly pure shear. The tangential force component, $\mu P_d A_c$, is mainly responsible for the near surface shear deformation, which results in formation of lips. Since both the component of deformation, $P_d A_c$, due to the normal force, and the shear component, $\mu P_d A_c$, due to the tangential force, are function of dynamic hardness, P_d, the dimension of the crater formed largely depends on this factor. The effect of friction coefficient, μ, was thus assumed to be insensitive when compared to hardness.

Sundararajan (and all other models based on rigid plastic theory) assumed that the target material to be perfectly plastic with no elastic spring back, but in reality the target material is elastic plastic, and the particle is elastic. Under such conditions, a velocity component vector (the elastic rebound velocity), normal to the instantaneous contact surface, that influences the rebound angle of the impinging particle, is introduced. Hence, the discrepancy of experimental rebound angle with that predicted could be eliminated once the corrections in the elastic rebound factor were considered in the rigid plastic model.

The localization model for solid particle erosion proposed by Sundararajan and Shewmon [14], takes into account the actual mode of material removal. The features of high strain rate, adiabatic and constrained deformation conditions not only cause the lip to form, but also effectively limit the deformation capability of the material [18, 22]. The nature of subsurface deformation underneath the impacting particle is illustrated for three cases; (1) strain hardening, (2) perfectly plastic and (3) strain hardening-softening (see Fig. 2.7)

(i) Condition of strain hardening:

When an impacting particle strikes a target material having a high and positive strain hardening capacity ($\partial\sigma/\partial E > 0$) with σ =flow stress, E = plastic true strain, the plastic deformation beneath the particle spreads uniformly over a large volume (Fig. 2.7.a). No localization of strain is observed and the formation of a lip of material is rare.

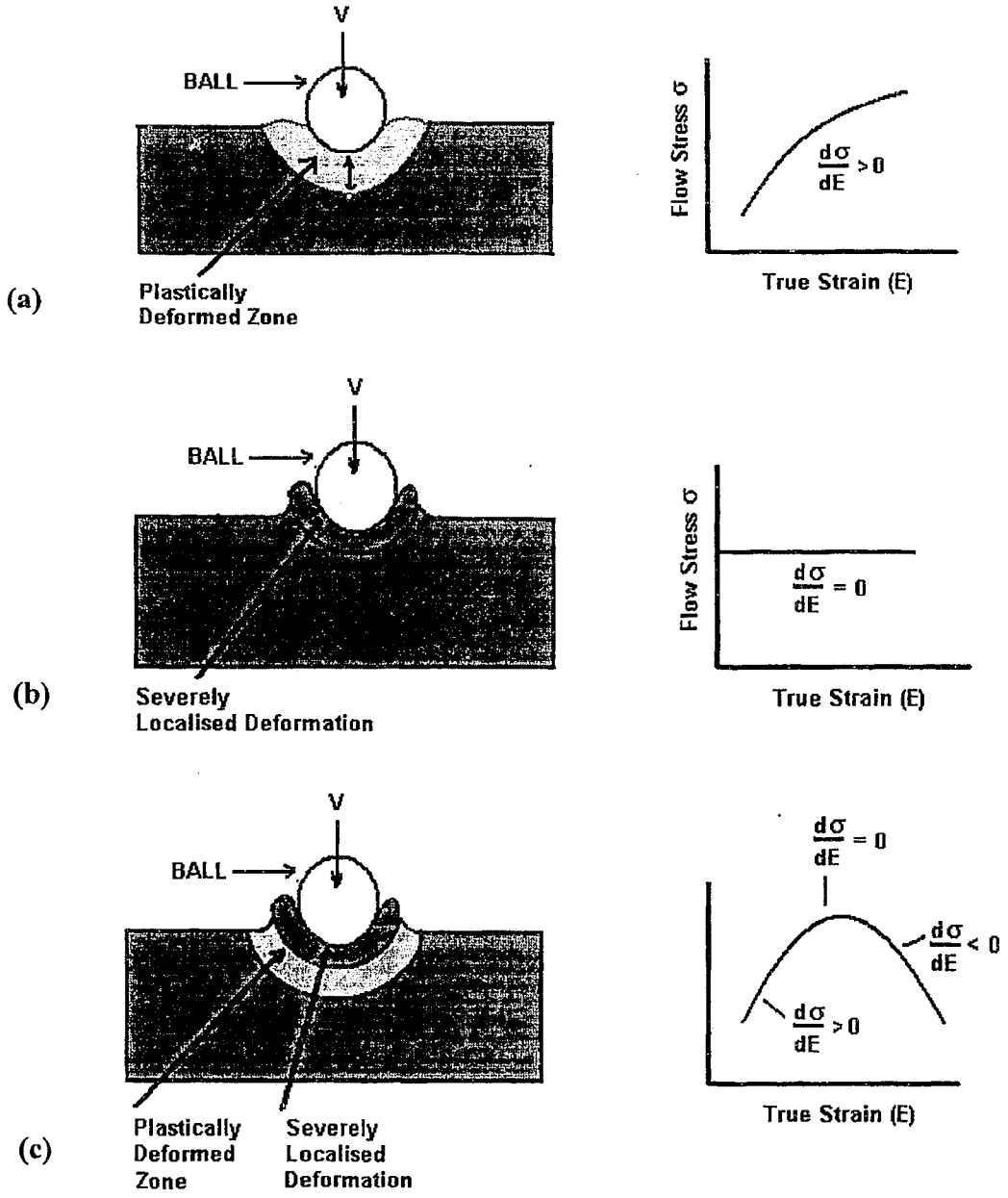

Fig.2.7: Schematic illustration of the interrelationship between the flow stress – strain behaviour of a material and its tendency to undergo localization of plastic flow during dynamic indentation. (a) Strain Hardening, (b) Perfectly Plastic and Fig.2.7 (c) Strain Hardening and Softening From Ref. [18].

The condition with no ability to strain or work harden ($\partial\sigma/\partial E = 0$), i.e. perfectly plastic material zone, is reported with the deformation underneath the particle (Fig. 2.7.b). The immediate localization to the near-surface layers leads to lip formation resulting in significant increase in the eroded volume of material.

(iii) Condition of strain hardening-softening:

The behaviour of strain hardening and softening are exhibited with strain hardening at low strain and strain softening behaviour at higher strain. The reason for this unusual stress-strain behaviour is the temperature rise in the deforming material, caused by plastic deformation at the high strain rates. Under such a condition, the material deforms homogeneously up to a critical strain, $\partial\sigma/\partial E = 0$. The plastic deformation starts at $\partial\sigma/\partial E < 0$ to form lips (Fig. 2.7.c).The critical strain thus represents the strain beyond which lip formation, induced by localization of plastic deformation, occurs.

Type of Impacts influencing Material removal:

(i) Normal Impact:

Sundararajan [18] considered that the critical strain is required for localization and lip formation and not fracture. If the fracture of the lip occurred readily, then the strain induced could be equated to critical strain of the eroding material. For normal impacts, the average strain induced per impact is usually very small, in the range of a few per cent of the critical strain. Hence a number of impacts are required at a given location before the critical strain is reached resulting in lip formation and its subsequent fracture.

(ii) Oblique impact

During oblique impact, a significant amount of plastic deformation occurs in the near-surface shear layer due to the tangential frictional force which exists at the contact surface between the particle and the eroding material. Very high shear strains are accumulated in this region, resulting in the formation of lips on the exit side of the crater.

The major difference between erosion at normal impact and oblique impact is the attainment of this critical strain for the fracture of the material to occur.

In the case of angular particles impacting at oblique angles, the frictional force between the particle and the eroding material induces very high levels of shear strain in the near-surface regions of the eroding material. The shear strains induced are usually high in magnitude and exceed the critical strain even during the first impact, leading to lip formation. Thus, the formation of lips occurs during each impact in the case of oblique impact. Further, the lip detachment from the crater edge is also easier in the case of oblique impact since the protruding lip is impacted from side in the subsequent impact. In case of spherical particles, the extent of shear deformation is very high at very oblique impact angles (e.g. less than 30°).

(iii) Combined impact:

The combined impact situation is the summation for both the normal and the oblique impacts. The impact angles which are very near to the transition range show both kind of behaviour, and hence the crater formed can be analyzed by summing the characteristic of both the normal and oblique impact.

2.3.1.4 Model of Papini and Spelt

A rigid plastic theory developed by Papini and Spelt [2, 3] generalized Hutchings' [1,9] rigid-plastic theory for square particles, so that arbitrarily shaped particles impacting against targets of arbitrary dynamic hardness and dynamic friction coefficient, could be treated. The specific case of two-dimensional 'diamond shaped' particles of various angularities was studied in detail by constructing a computer program capable of describing the trajectory of particles as they form impact craters, as well as the size and shape of the craters [2]. A parametric study of possible input parameters using this computer program predicted fundamental cutting mechanisms of erosion similar to those observed by Hutchings in his experiments with square plates. Unfortunately, because of the lack of available experimental data, and the difficulties associated with performing

angular particle experiments, only the particular case of square particles (i.e. A=45°) was verified experimentally, by comparison with the data of Hutchings [1].

Impact due to two-dimensional diamond shaped particles – analytical model:

The model predicts the impact of diamond shaped particles (see Fig. 2.8) having angularity A, launched at incident angle of attack α, having an orientation angle (analogous to Hutchings' rake angle [1] for square particles), θ_i, arriving at the surface with an incident velocity V_i. Implementation of the rigid plastic theory in a computer simulation, for impact of particles of this type, has already been explained in detail by Papini and Spelt elsewhere [2, 3]. Only the main points of the theory are summarized here.

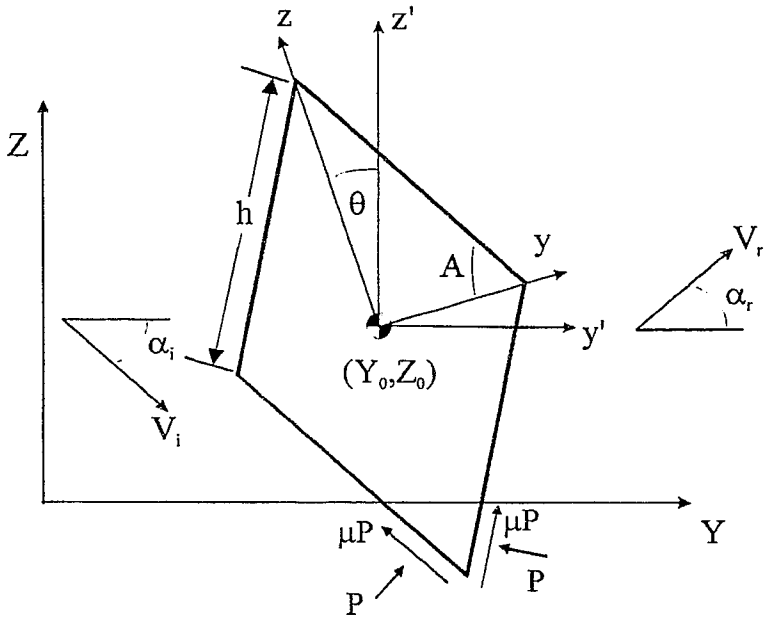

Fig.2.8: Two-dimensional diamond shaped particle parameters, with point of first impact at origin of inertial (Y, Z) coordinate system. Particle has a uniform thickness, w, in the XZ plane. Forces acting on particle edges are shown. From Ref. [2].

It is most convenient to determine the kinematics of the particle during impact using an XYZ inertial frame of reference shown in Fig. 2.8. Only collisions where the half of the particle below the centre of mass (i.e. below the Z=0 plane) makes contact are considered explicitly in this analysis. The shape of the lower half of the particle can thus

be defined as [2]:

$$\begin{aligned} &Z(X,Y)=Z_0+(Y-Y_0)\tan(\theta\pm A)\pm\frac{h\sin(2A)}{2\cos(\theta\pm A)} \\ &Y_0-h\cos(A)\cos(\theta)\le(Y)\le Y_0\mp h\sin(A)\sin(\theta) \\ &Z(X,Y)=Z_0+(Y-Y_0)\tan(\theta\mp A)\pm\frac{h\sin(2A)}{2\cos(\theta\mp A)} \\ &Y_0\mp h\sin(A)\sin(\theta)\le(Y)\le Y_0+h\cos(A)\cos(\theta) \end{aligned} \tag{2.7}$$

with Y_0 and Z_0 locating the centre of mass of the particle. The differential equations governing the motion of the diamond-shaped particle (Fig. 2.8) in the YZ plane are [2]:

$$\begin{aligned} &m\ddot{Y}_0=F_Y \\ &m\ddot{Z}_0=F_Z \\ &\frac{1}{6}mh^2\ddot{\theta}=M_X \end{aligned} \tag{2.8}$$

where m is the mass of the particle, $\ddot{Y}_0$ and $\ddot{Z}_0$ are the accelerations of the center of mass of the particle in the Y and Z directions, $\ddot{\theta}$ is the angular acceleration of the particle about the X axis, F_Y and F_Z are the Y and Z components of the total forces per unit particle thickness (i.e. in the X direction) acting on the particle, and M_X is the total moment per unit particle thickness acting about the center of mass of the particle. The forces and moment in eq. (2.8) are a result of both friction and dynamic contact acting on the portions of the left and right side of the particle in contact with the surface (see Fig. 2.8).

At any instant during the contact, it can be shown that the total forces acting on the left and right side of the surface of the particle in contact with the target are [2]:

$$
\begin{aligned}
F_{Y_L} &= -p_d \int_{Z_C} dZ \pm \mu p_d \int_{Y_C} dY \\
F_{Z_L} &= p_d \int_{Y_C} dY \pm \mu p_d \int_{Z_C} dZ \\
F_{Y_R} &= -p_d \int_{Z_C} dZ \mp \mu p_d \int_{Y_C} dY \\
F_{Z_R} &= p_d \int_{Y_C} dY \mp \mu p_d \int_{Z_C} dZ
\end{aligned}
\tag{2.9}
$$

where P_d is the dynamic hardness of the target, μ is the friction coefficient, the subscripts L and R refer to the portions of the left and right side of the particle (Fig. 2.8) in contact with the surface, and the quantities represented by the integral are the instantaneous contact area per unit thickness. The upper sign in eq. (2.9) indicates friction towards the vertex of the particle, and the lower one, friction away from the vertex. The moments due to forces acting on the left and right side of the particle, tending to rotate the particle about an axis X through the centre of mass, can be obtained by multiplying the differential forces in eq. 2.9 by their appropriate moment arms, and integrating over the contact area [2]:

$$
\begin{aligned}
M_{X_L} = -p_d \int_{Z_C} (Z_0 - Z)\,dZ \pm \mu p_d \int_{Z_C} \frac{(Z_0 - Z)}{\tan(\theta - A)}\,dZ + \\
+ p_d \int_{Y_C} (Y - Y_0)\,dY \pm \mu p_d \int_{Y_C} (Y - Y_0)\tan(\theta - A)\,dY \\
M_{X_R} = -p_d \int_{Z_C} (Z_0 - Z)\,dZ \mp \mu p_d \int_{Z_C} \frac{(Z_0 - Z)}{\tan(\theta + A)}\,dZ \\
+ p_d \int_{Y_C} (Y - Y_0)\,dY \mp \mu p_d \int_{Y_C} (Y - Y_0)\tan(\theta + A)\,dY
\end{aligned}
\tag{2.10}
$$

where Y and Z locate points on the particle surface in contact with the target.

Substitution of eqs. (2.9) and (2.10) into eq. (2.8) results in a system of three coupled

differential equations describing the motion of the center of mass of the particle (Y_0, Z_0) and the orientation of the particle, θ, at any time during the impact. While the particle is in full contact with the target (i.e. both the left and right sides contact over contiguous areas), the equations can be solved in closed form. However, in most cases, at some point during the impact, portions of the particle lose contact with the surface as the particle rotates and forms the crater. The particle can make simultaneous contact over more than one contiguous area, so that the instantaneous contact area described by the integrals in eqs. (2.9) and (2.10) not only is a function of time, but also often must be split into distinct intervals on each side of the particle. This makes closed form solution of the differential equations impossible. The equations are thus best solved numerically in time steps, with the above forces and moments assumed constant over each small time interval. In this scheme, the second order differential equations describing the particle dynamics, eq. (2.8), are reduced to a set of six first-order differential equations, which are integrated numerically for each time step.

The crater shape and the particle centre of mass position, orientation, linear and angular velocity and acceleration are updated at the end of each time step, and used as initial conditions for the following time step. The calculation continues in this manner until contact between the lower half of the particle and the crater is no longer possible. Details of the procedure, and its implementation in a computer simulation, are given in Refs. [2] and [3].

2.4. Parameters affecting erosion

A number of investigators [1-18] have attempted to present erosion models based on the influence of various parameters affecting the erosion mechanism. A simplified approach to the problem consists of separating the effects of the individual variables. An attempt has been made to group the variables affecting the erosion into three types: impingement variables describing the particle flow, particle variables, and material variables [Fig. 2.9].

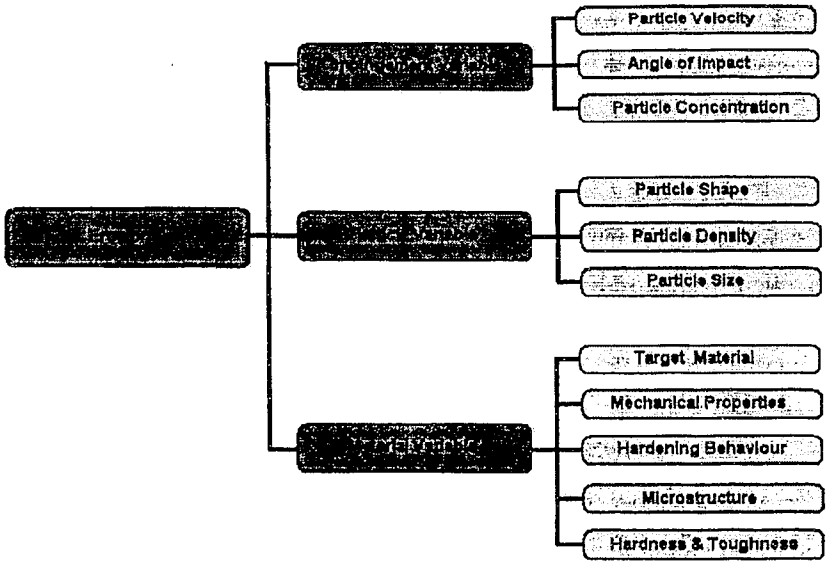

Fig.2.9 Factors affecting erosion mechanism

2.4.1 Erodent Velocity

Finnie [13] reported that erosion is proportional to a simple power of velocity. The equation, based on his work on SAE 1010 Steel, is given as:

$$\upsilon \propto V_i^{\varphi} \tag{2.11}$$

Where, V_i is the velocity of erodent and φ was 2.0. However, his work on other materials gives a range of φ between 2.04 and 2.44. A similar study was conducted by Goodwin et al. [23] eroding steel at normal impact angles (i.e. incident angle at 90°) with quartz media in the size range from 25-210 μm at velocities ranging from 200 to 1800 ft/s. They proposed an equation based on the results that erosion (υ) is dependent upon a simple power of velocity (V_i), i.e.

$$\upsilon \propto V_i^{\psi} \tag{2.12}$$

where the exponent ψ varies from 2.0 to 2.3 for 25 μm to 125 μm, respectively.

Bitter [24] reported a threshold velocity below which no erosion occurs. Hutchings [1,9] conducted experiments by impacting steel targets with square angular

particles and noticed that for the same rake angle (i.e. the orientation of the particle with the target surface) the volume of material removed increased with increase in the impacting velocity of single particle. The experimental data of Hutchings were later compared with the predicted results of a rigid plastic model, developed by Papini and Spelt [2,3] for the identical conditions of impact, and a good agreement was found.

2.4.2 Angle of Attack

Angle of incidence or angle of attack of the erodent particle stream significantly affects the amount of erosion of the target material, particularly in the case of ductile materials. Finnie [12,13] predicted the material removal dependence on angle of impingement of erodent particles.

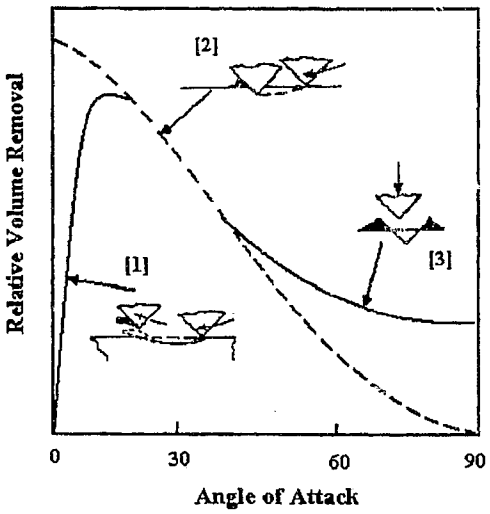

Fig.2.10: Variation of volume removal with angle curves 1, 2 and 3.
From Ref [25].

Experimental data for the ductile metal eroded by rigid abrasive grains was plotted by Sheldon and Finnie [25], with the assumption of constant plastic flow pressure behaviour in the ductile material. The experimental results demonstrated that the dependence of volume removal on angle of impingement was similar for wide variety of ductile metals, having a wide range of thermal and mechanical properties. This was noticeable from the similar nature of material removal curves for glass and untempered martensite.

Fig. 2.10 shows the ductile material removed by the particle at various angles of attack [25]. The curve (1) represents the erosion at very shallow angles where the target material is completely removed from the surface of the target material. At angles impacting near the curve (2) range, the particle ploughs the material to the crater edge, which is removed by a subsequent incoming particle. The indentation feature is predominant at normal angles of impact, i.e. the curve (3) range. It was thus concluded that angle of impact has a significant effect on the mechanism of erosion and material removal, irrespective of the nature of target material. Most investigators demonstrated similar erosion curves for ductile materials and observed that peak erosion loss occurs at around 20° and 90° (normal incidence) for brittle materials.

Sundararajan [18] illustrated relative erosion rates of Nickel alloys at various impact angles and impact velocities with the use of SiC erodent particles, and obtained higher erosion rates for shallow impact angles, compared to normal or near normal angles of incidence.

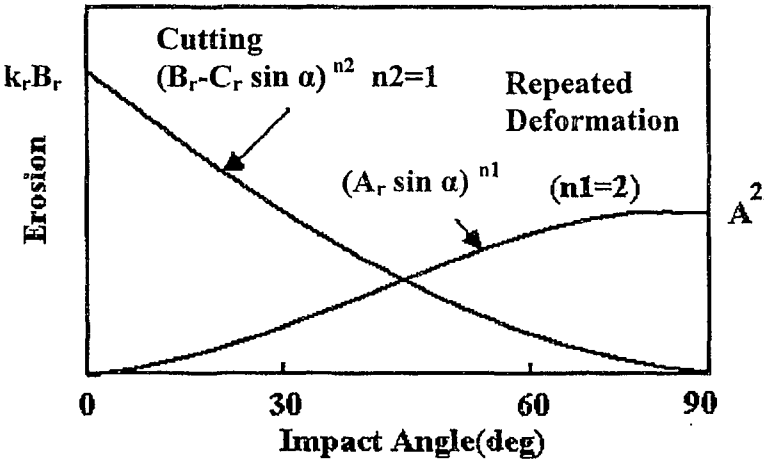

Fig.2.11: Repeated deformation and cutting action expressed by trigonometric functions. From Ref. [14].

Oka et al. [17] developed a trigonometric function model to predict erosion, which involves the product of two factors, one for the cutting action, and the other for the repeated deformation (see Fig. 2.11).

$$E_r = k_r (A_r \sin \alpha)^{n1} (B_r - C_r \sin \alpha)^{n2} \quad (2.13)$$

Where E_r is the erosion rate expressed in units of mm^3kg^{-1}, α is the angle of impact and k_r, A_r, B_r, C_r, n1, n2 are constants having dependence on the impact conditions. The first group of parameters in the trigonometric function represents the vertical component of the impact energy approximating repeated plastic deformation, and the second group of parameters is responsible for the cutting action by the horizontal component of impact energy. Separate plots of cutting and deformation parameters are demonstrated in Fig. 2.11, approximating the predictions obtained by other investigators. Aquaro and Fontani [7] reported the change in shape of the crater (Fig. 2.12) with varying angle of attack of the impacting spherical particles. They successfully simulated crater shapes and predicted the material removed.

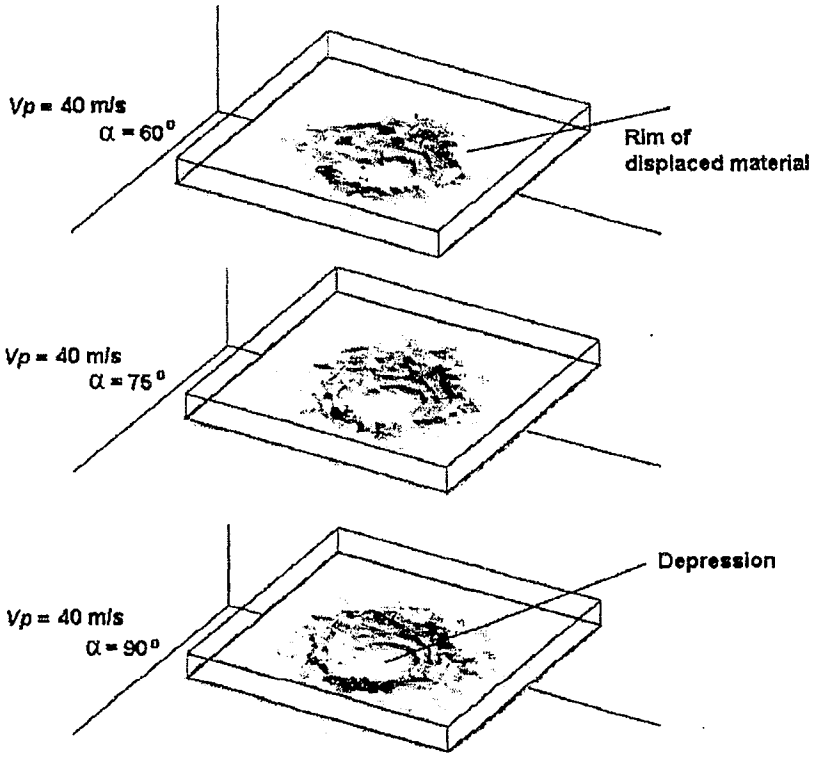

Fig.2.12: Craters formed by impacts of spherical particles at different angles of attack. From Ref. [7].

2.4.3 Orientation angle/rake angle

This parameter is studied only in ductile cases, where erosion due to angular particles is involved. Hutchings [9] was one of the first investigators to study the effect of variation of rake angle on the volume of material removed, involving square particles. Papini and Spelt [2,3] studied the effect of orientation angle in detail, and concluded that, for a given angle of attack, the crater volume increases with an increase in orientation angle, until a transition angle is reached, wherein the crater volume is highest. At this transition angle, the rotation of the rebounding particle changes from forwards to backwards. The crater volume drops drastically above this transitional orientation angle.

2.4.4 Material properties

Target Material Hardness

Material hardness is the most important property influencing the nature of ductile erosion. Hutchings and co-workers (1, 9-11) characterized the influence of dynamic hardness on erosion due to impact of angular square particles. Sundararajan and co-workers [14,15,18,22] noticed that the dynamic hardness greatly influenced the formation of localized plastic zones in the eroding material underneath the particle that affected the formation of lips, and subsequent material removal from the surface. As expected, both investigators reported a higher resistance to erosion for harder materials.

Strain rate sensitivity

In studying the erosion of ductile materials by impacting square angular plates, very high strain rates in the range of 10^5/s to 10^7/s were reported by Hutchings [9]. Sundararajan [14,18] also reported high strains at oblique impacts. Similar observations were also reported by Aquaro and Fontani [7] for spherical particles, where strains often reached the critical level in oblique impacts as compared to normal impacts and therefore, more than one impact was often required to remove target material in cases of normal impacts.

Erodent hardness

Theories related to ductile erosion have specified that little effect of hardness on erosion rate should be expected, as long as the impacting particle hardness is greater than the target hardness. Finnie [12,13] noticed that the heat treatment of steel had no effect on their erosion resistance as hardness of eroding particles such as SiC and Al_2O_3 was much greater than the ductile target material. The rigid plastic models of Hutchings [1, 9-11], Papini and Spelt [2,3], and Sundararajan [14, 18] have considered particles to be rigid and thus that a change in the erodent hardness has the least influence on the magnitude of erosive wear.

2.4.5 Erodent Shape

The nature of the crater profile and the rate of erosion also greatly depend on the shape of the erodent. When ductile erosion dominates, it has been demonstrated that the rate of erosion is higher for angular particles than spherical particles, the mass of the particles and all other parameters being equal. Erosion by spherical particles develops 'hill and valley' crater profiles. For impacts with square angular plates, Hutchings [9] found deep craters cut by forward rotating particles with materials pileup at the crater edge, and long and shallow craters cut by backward rotating particles. The degree of angularity of the particles is also important in determining the effective material removal rate. Papini and Spelt [2,3], conducted parametric studies of various symmetric angular particles and found that erosion was highest in case of 80° particles, all other conditions being equal.

2.4.6 Erodent Size

Kosel [26] found that for the ductile materials, the size of erodent particles has a very low effect on the erosion rate for the particles sizes above 100 μm, but the erosion rate decreases rapidly with particle sizes below 100 μm. For sizes greater than this critical value, the relative erosion is essentially independent of the particle size. It has also been suggested [26] that for ductile erosion to be effective there exists a threshold size (≅5 μm) of the particle, below which no erosion is possible.

Chapter 3

Experimental Apparatus and Procedure

This chapter describes the experimental set up used to launch single angular particles against ductile target materials, and to measure the rebound kinematics. Note that portions of this chapter will soon been published in a refereed journal paper [27].

3.1 Background

A number of authors have performed experiments involving the impact of single spherical particles. For example, Tirupataiah et al. [15] constructed a gravity drop system to measure the normal impacts by hard balls, impacting the samples with velocities of 10 m/s. The system released one ball at a time, dropping freely under the influence of the gravity on the target material fixed rigidly to the target holder. To measure the velocity of the incident and the rebound ball, two photodiode emitters and sensors separated by known distance were used.

In a similar experiment for the oblique impact of hard balls against a ductile material, Sundararajan and Shewmon [14] used a single stage helium gas gun to accelerate steel balls through a one meter long barrel. A target holder held the eroding material at any desired angle. The velocities were measured using a photodiode timer system, and the angle of the rebounding ball was measured using an aluminum foil system. The foil system consisted of two separate units separated by a fixed distance, with each unit containing two aluminium foils separated by an insulating paper. The timer was activated as the ball pierced the first unit and stopped when the ball pierced the second unit. The elapsed time was then used to calculate the rebound velocity and the holes left by the ball back tracked the path of the rebounding ball, thus allowing for estimation of the rebound angles.

Impact experiments of single glass spheres on coated surfaces were performed by Papini and Spelt [12], who used a gas gun to launch the particles, and flash photography to measure the particle kinematics. In their setup, a single glass sphere was loaded into a cylindrical urethane sabot, which, in turn, was loaded into a long steel barrel. A solenoid valve serving as a trigger was attached to the barrel via a breech, and was connected to a compressed air cylinder. The air accelerated the sabot and the glass sphere to the end of the barrel where a ring stopped the sabot and allowed the sphere to exit, and impact the target material. The acceleration was regulated by the air pressure. CCD cameras, in conjunction with high speed flashes, and an infrared sensitive trigger were used to take images of the incident and the rebounding sphere at the instant of impact. This allowed both the incident and rebound velocities and angles to be determined.

Until the present work, the only existing measurement of single angular particles was performed by Hutchings [9]. The reason for such a limited experimental database is that obtaining repeatable data with angular particles is extremely challenging. Hutchings accelerated square plates to velocities of 200 m/s using a compressed gas gun with a barrel of rectangular cross section. Each of the plates was held in a paxolin sabot, which was a sliding fit in the gun barrel. At the muzzle of the gun, the sabot was arrested and the plates were allowed to fly freely to impact the target material. The velocity of the plates was determined by interruption of two light beams, and a high speed camera recorded the impact. The orientation angle, i.e. the rake angle as defined by Hutchings [9], (see section 2.3.1.2), of the angular particle impacting the target material could be varied by adjusting the orientation of the slot in the sabot. The plates, however, were very large compared to those used in the present study, and only square particles could be launched in the rectangular bore gun.

3.2 Particle and Target Material Properties

The diamond-shaped particles to be launched were cut from thick hardened AISI A2 tool steel using a CNC end mill, and heat-treated in a furnace for 10 minutes at 843 °C and finally, quenched in oil. Particular care was taken to ensure that all the edges were machined as square as possible, and were left sharp to ensure that out-of-plane effects

would be minimized. The side edge length h defined in Fig. 2.7 (see section 2.3.1.4), and the width w, for each type of particle of specific angularity, as shown in Fig. 3.1, is presented in Table 3.1.

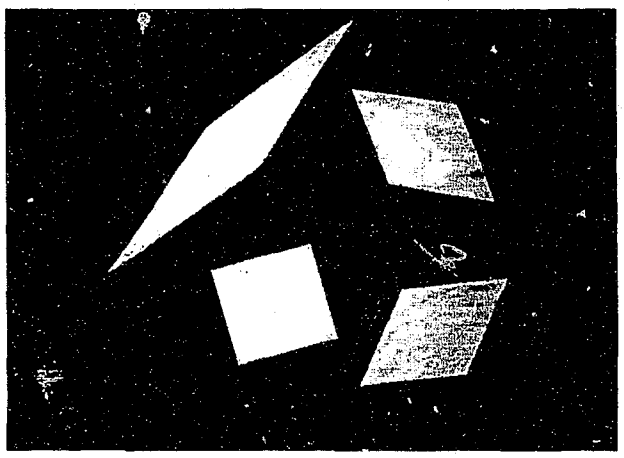

Fig. 3.1: Sample particles with various angularities (i.e. A=30°, 45°, 60°, 90°)

The target material was 3003 aluminum alloy plate stock of 6.35 mm (0.250") thickness x 30.15 mm (1.187") x 152.40 mm (6.000"), so chosen because of its low hardness, and closeness to perfectly plastic behaviour. The static hardness of the particles was Brinell hardness-752, which is sufficiently larger than that of the target (i.e. Brinell hardness- 35) to ensure that deformation of the particle during impact was negligible. To ensure a flat target surface, the specimens were faced using a three-insert carbide cutter on a vertical end mill.

A (deg.)	**h** (mm)	**w** (mm)
30	6.35	3.20
45	5.94	2.92
60	6.35	3.20
80	11.14	2.93

Table 3.1 Dimension of the particles used in the study of erosion

The chemical composition of aluminum 3003 and its physical and mechanical properties are tabulated in Tables 3.2 and 3.3, respectively. The eroding particles were machined from high strength tool steel with a uniform thickness, and were thus considered non–deforming (i.e. rigid).

Component	Wt. %
Al	96.7 - 99
Mn	1 - 1.5
Fe	Max 0.7
Cu	0.05 - 0.2
Si	Max 0.6
Zn	Max 0.1

Table 3.2 Chemical composition of constituents in Aluminium 3003 alloy
From Ref. [29]

Physical Properties	
Density	2730 kg/m^3
Mechanical Properties	
Hardness, Brinell	35
Ultimate Tensile Strength	131 MPa
Tensile Yield Strength	124 MPa
Modulus of Elasticity	68.9 GPa
Poisson's Ratio	0.33
Shear Modulus	25 GPa
Shear Strength	82.7 MPa

Table 3.3: Physical and mechanical properties of aluminium-3003 alloy.
From Ref. [29].

3.3 Design Requirements of the Apparatus

Impact experiments involving angular particles are extremely difficult to perform in a repeatable fashion. If particles of uniform thickness are launched, then the impact must occur in a single plane, perpendicular to the target surface. This means that the particle must be launched in a manner such that it arrives at the target with its velocity vector in the plane of the particle itself. If not, the particle will rebound out-of-plane, and measurement of rebound parameters using a high speed camera (which is placed with its lens in the same plane as the launched particle) will be impossible. The present author initially attempted to launch via a gas gun/sabot setup similar to that of Hutchings [9] and Papini and Spelt [2,3], but found problems with particles arriving at the surface in a non-planar orientation due to excess deformation of the carrying sabot upon hitting the stopping ring. In order to overcome these problems, and to address the criteria described above, a catapult apparatus was designed and built such that it be capable of launching single angular particles of the type shown in Fig. 3.1 while ensuring:

a) Only 2-dimensional surface contact in Y-Z plane, (see Fig. 2.7 in Section 2.3.1.4) occurred
b) The apparatus be capable of measuring the particle kinematics (i.e. the incident and rebound linear and angular velocities) for determining the energy loss during the collision
c) The apparatus be adjustable so that the angle of attack, initial particle orientation, and velocity could be varied, and particle of various angularities could be accommodated.

3.4 Catapult/FlashCam Setup

The catapult apparatus shown in Fig. 3.2 was found to be the best solution. The catapult was loaded manually by pressing the launching end of the lever arm down until it was locked to the release mechanism. The locking key of the release mechanism locked the lever arm in place while the two springs (19 mm tempered steel cot spring,

Cat# 1832K21 McMaster-Carr, Chicago, IL, USA, k=19 KN/m) coupled in series attached to the other end of the lever arm, were kept loaded. The particle was then loaded into the holder, and released, as seen in Fig. 3.3. After its release, the loaded lever arm was stopped by an adjustable pad made of high density rubber.

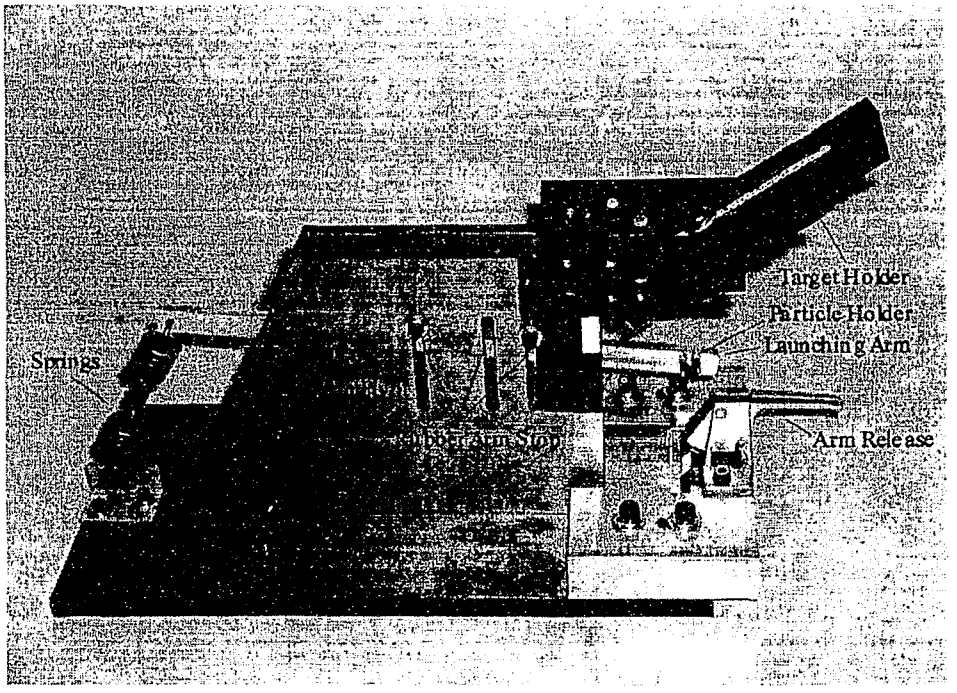

Fig. 3.2: Catapult apparatus designed to launch single angular particles .From Ref. [27]

The aluminium particle holder specifically designed and manufactured for each type of angular particle, was attached to the launching end of the lever arm that could be rotated about the X-axis allowing the variation of the initial orientation angle θ_i. An adjustable target holder was securely attached to the frame of the catapult so that the angle of incidence, α, could be varied, and that the plane of the target was always perpendicular to the plane of the launched particle. Proper care was taken to minimize the possibility of misalignment between the particle velocity vector and the target; i.e. to minimize the out of plane effects. With the described lever arm length and spring setup,

particle velocities in the range 25-30 m/s were obtained.

To obtain pictures of the incident and rebound linear and angular velocities, and the trajectory of the angular particle in the perpendicular plane, a FlashCam high-speed digital camera (Cooke Corp., Auburn Hills, MI, USA) was used. The setup is detailed in Fig. 3.4. The FlashCam is a digital camera with a high speed electronic shutter capable of taking 10 exposures in a standard video frame with a minimum separation between each exposure and exposure time of 1 μs.

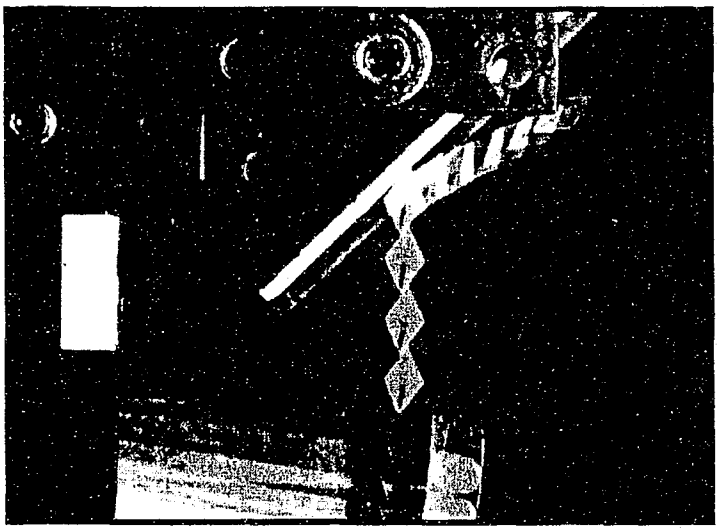

Fig. 3.3: Sample Image obtained from experimental setup. The image shows a 60° angular particle released by the particle holder of the catapult and impacting a target. Incident angle =45°, incident velocity =25 m/s.

The camera was triggered via the flash output signal from a MultiTRIG (Cooke Corp., Auburn Hills, MI, USA) multi-sensor triggering system. The trigger was activated by the sound generated by the release of the lever arm of the catapult which, in turn, triggered the FlashCam to stop acquiring frames. A frame grabber stored the frame which contained the multiple images of the particle in both incident and rebound flight. An adjustable delay on the MultiTrig, along with the delays on the FlashCam allowed for proper timing of the process so that the correct frame was grabbed. Images of the particle in flight just before, and just after the impact, were obtained, so that the orientation and

the trajectory of the particle could be determined accurately. Impact experiments, at various combinations of A, θ, and α, involving angular particles were performed to obtain the experimental data.

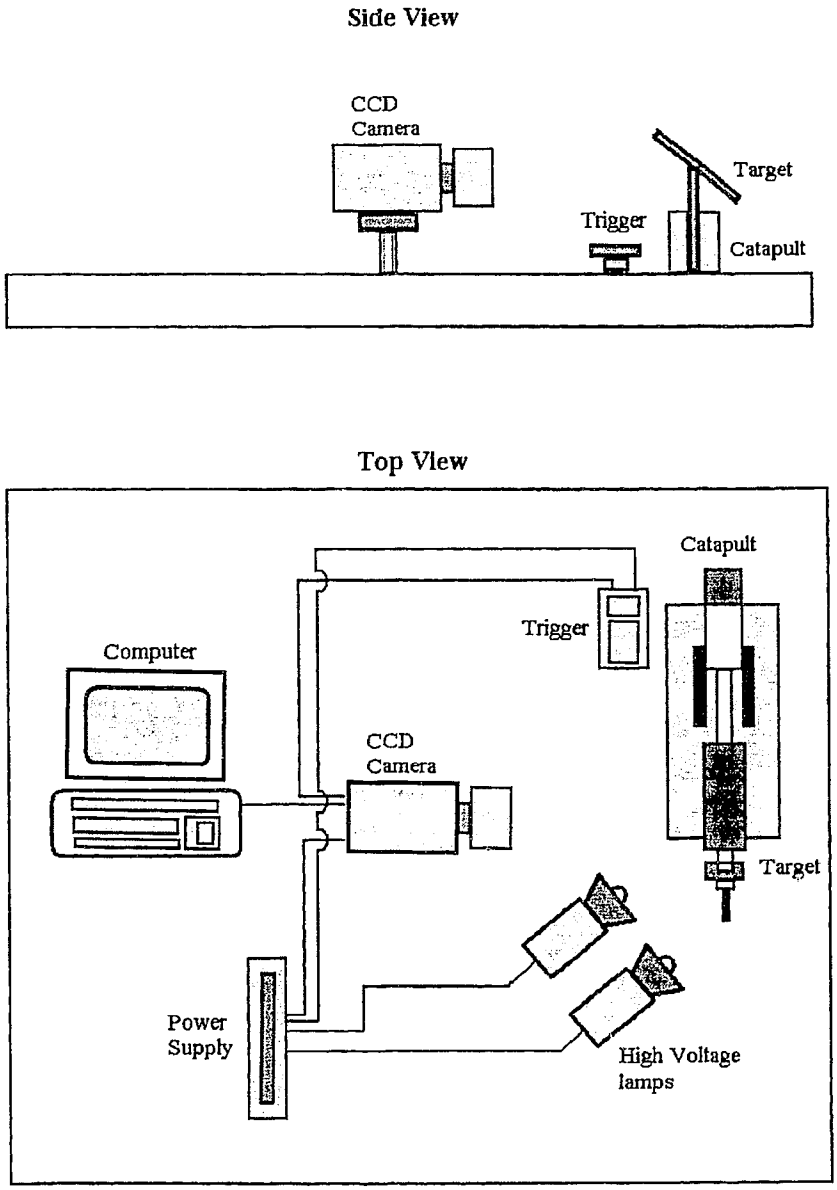

Fig.3.4: Schematic view of the Catapult/Flashcam experimental setup

3.5 Analysis of Images to Determine Particle Kinematics

The images of the collision trajectories of type shown in Fig. 3.3 were analysed using image analysis software (Scion Image Beta, Scion Corporation, Maryland) to measure the angle of attack and the angle of rebound, the particle orientation angle at the instant of impact, and the linear and angular velocities of the incident and the rebounding particle. The incident and rebound linear velocities were obtained by measuring the distance between two successive exposure images, divided by the delay between exposures. Due to blurring of the images, the following uncertainties were encountered: on the order of ± 0.2 mm for the linear measurement, and $\pm 0.8°$ for the angular measurement. These uncertainties resulted in a maximum error of 1 m/s in measurement of linear velocity, and 40 rad/s in measurement of angular velocity.

3.6 Measurement of crater dimensions

Replica casting was used to measure the volume of the crater formed by the impacting particle. Reprorubber (Flexbar Machine Corporation, Islandia, NY), which was used in this replication technique, is a metrology-grade rubber that provides virtually a perfect replica casting of internal and external forms. The castings are green in color and have excellent dimensional and deformation stability up to a temperature of 60°C. A mix of Reprorubber that is self curing in minutes was poured on the target surface, completely filling the bare craters. After 15 to 20 minutes, the self cured rubber was then carefully peeled off from the target surface with the help of forceps.

A protruding surface profile, which is an exact reverse replica of the actual crater, appears on the surface of the Reprorubber facing the target surface. A cross section of the crater replica was then cut out by a razor blade and placed on a white paper with a calibrated scale and examined under a microscope. A 5-mega pixel digital camera (Canon Inc, Tokyo, Japan), attached to the eye piece of the microscope was used to take the image of the crater replica, which was later analyzed using image analysis software to examine the nature of crater profile and measure its volume. To measure the crater volume, the image analysis software counts the number of pixels in the given area. The

scale of the software was first calibrated using predefined area of an image and then the cross sectional area of the crater was measured and multiplied with the width of the particle to calculate the volume.

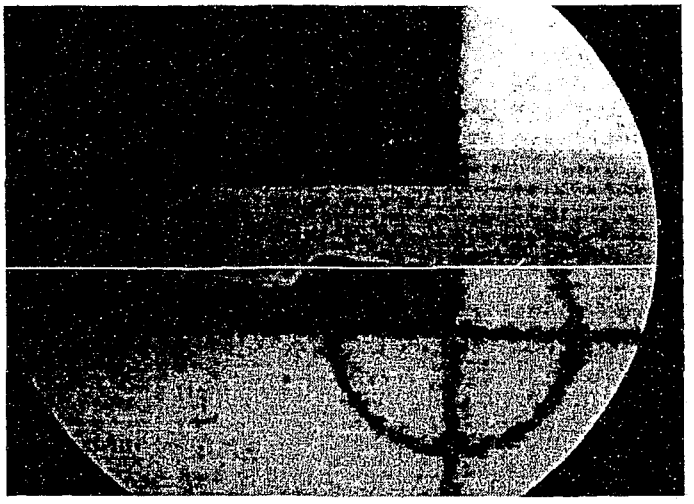

Fig 3.5: Sample of rubber casting of a crater. The crater dimensions are measured below the marked line neglecting the pile up material at the crater edge above the marked line.

Earlier, unsuccessful attempts were made to measure the crater volume by using an optical profilometer, which is based on the principle of measuring the surface profile by light reflection and interference. Due to low amount of light reflecting from the crater surface, the optical profilometer was unable to measure deep craters resulting from the forward rotations. An attempt was also made to analyse the Reprorubber replicas with the optical profilometer, but similar problems of low reflectivity were encountered from the rubber surface.

Chapter 4

Results and Discussion

As mentioned in Chapter 3, impact experiments involving single angular particles of various angularities were performed for two reasons: first to identify the mechanism by which metal is removed from the surface, and second to compare with the rigid plastic theory developed by Papini and Spelt [2,3]. Impact experiments using the setup described in Chapter 3 were performed using diamond shaped particles of the type shown in Fig 4.1. A part of this chapter will soon be published in a refereed journal [27].

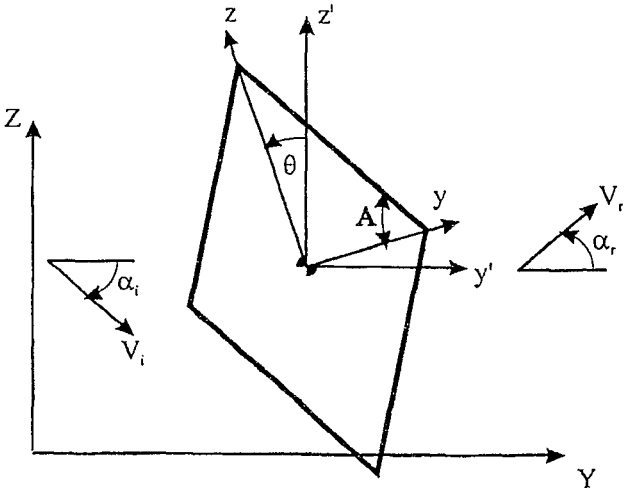

Fig.4.1: Symmetric angular particle parameter definition

The experimental results were obtained for particles with different angularities (i.e. A=30°, 45°, 60°, 80°) with known particle side length h. The incident impact parameters of angle of attack α, particle orientation angle θ_i, incident velocity V_i, incident angular

velocity $\dot{\theta}_i$, were varied to understand their effect on the rebound particle kinematics and crater volume. Note that the sign convention for angular velocity $\dot{\theta}$, is the same as that for the orientation angle θ_i, (i.e. a positive $\dot{\theta}$ implies a counter-clockwise or backward rotation).

Impacts were analyzed for only those conditions where the impact occurred in the Y-Z plane (see Fig. 4.1) (i.e. a 2-dimensional impact), perpendicular to the target surface. The 2-D nature of the impact could be confirmed by examination of the impact photographs. Note that each tabulated experimental data point (see Tables in appendix) represents the average of at least three experiments at nominally identical input conditions.

The crater volumes were measured, in the manner explained in Chapter 3 for the plowed target material below the Z=0 plane. The lips (i.e. the pileup) of the target material formed at the end of the crater edges were not considered for measurement, as the model is incapable of accounting for this.

4.1 Typical erosion mechanisms

Generally, two types of erosion mechanism were identified, depending on whether the particle rotated forwards or backwards. When the particle rotated forwards, target material was plowed into a lip at the edge of the crater, but no target material was actually removed. When the particle rotated backwards, in most cases, a pure cutting or machining action was observed, resulting in removal of a chip of material. This typical behaviour was also observed by Hutchings for experiments involving the impact of square particles [9]. These two mechanisms are considered in more detail below.

4.1.1 Impact involving forward rotation of the particle

The typical characteristic of these impacts involved forward tumbling of the particle after striking the target material. High-speed photographs in Fig. 4.2 show that the particle rebounded from the surface with an appreciable rotational velocity in the

direction. The indentation formed by the forward impact had the characteristic triangular shape shown in Fig.4.3. Obviously, the incident particle parameters which influenced the particle kinematics also significantly affected the nature of crater profile.

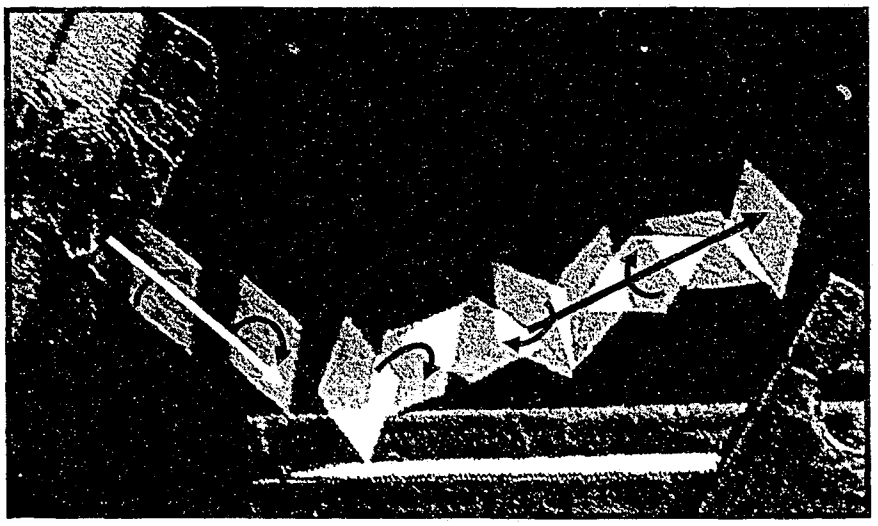

Fig.4.2: Impact of an angular particle (A=60°) that undergoes forward rotation (incident conditions: α=30°, θ_i=19°, V_i=24.5 m/s, $\dot{\theta}_i$ =-170 rad/s) leading to a single impact. Shown are the directions of impact (white arrow), rebound (black arrow) and the forward rotation of the particle

Under the plane strain conditions, all the metal displaced from the indentation was The target material is pushed forward, leading to the formation of a short and shallow crater, with the material piled up at the edge of the crater as shown in Fig.4.4. When the particles are launched in streams, material removal is thought to occur this by subsequent impacts of particles on this lip of piled up material. Previous studies involving impact of square plates [9] have also reported this behaviour.

For forward rotating particles with steeper angles of attack, and especially when the initial orientation angle θ_i (Fig. 4.1) was negative, an initial forward impact was often followed by multiple forward secondary impacts, as the particle skipped across the surface. An example is shown in Fig. 4.5, where the primary impact is by the leading 60°

60° vertex, followed by two successive secondary impacts: the first by the adjacent 120° vertex, followed by the 60° vertex opposite to the leading vertex.

Fig 4.3: Profile of the crater formed by impact of forward rotating angular particle resulting in formation of lip at the end of crater edge.

Fig 4.4: Top view of crater left by an angular particle (A=60°) that underwent forward rotation

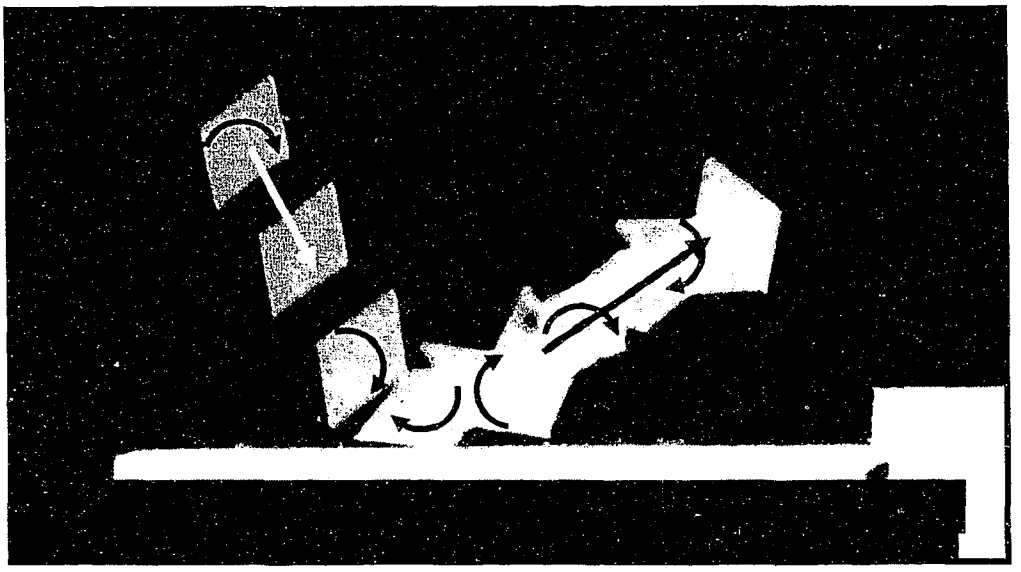

Fig. 4.5: Forward rotations resulting in three impacts of the particle, the first by the 60° vertex, the second by the adjacent 120° vertex, and the third by the 60° vertex opposite to the first impacting vertex. Incident conditions: α =68°, θ_i =-21°, V_i=25 m/s and $\dot{\theta}_i$ =-40 rad/s.

4.1.2 Impacts Involving Backwards Rotation

Particle impacts which involved backward rotation of the particle resulted in machining and/or cutting of the target material, giving a long and shallow crater, as shown in Fig 4.6. Rather than extruded material appearing at the lip of the crater, as was the case with forward rotating particles, actual material loss, in the form of a machined metal chips, sometimes occurred with backwards rotating particles. Fig.4.7 shows the machining action, with an ejected chip of the metal clearly visible. When streams of particles are involved, such cut surfaces are left exposed to subsequent impacts.

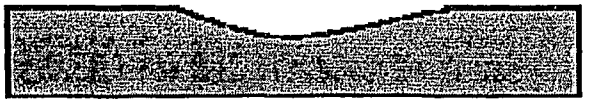

Fig 4.6: Profile of the crater formed by impact of backward rotating angular particle resulting in removal of target material

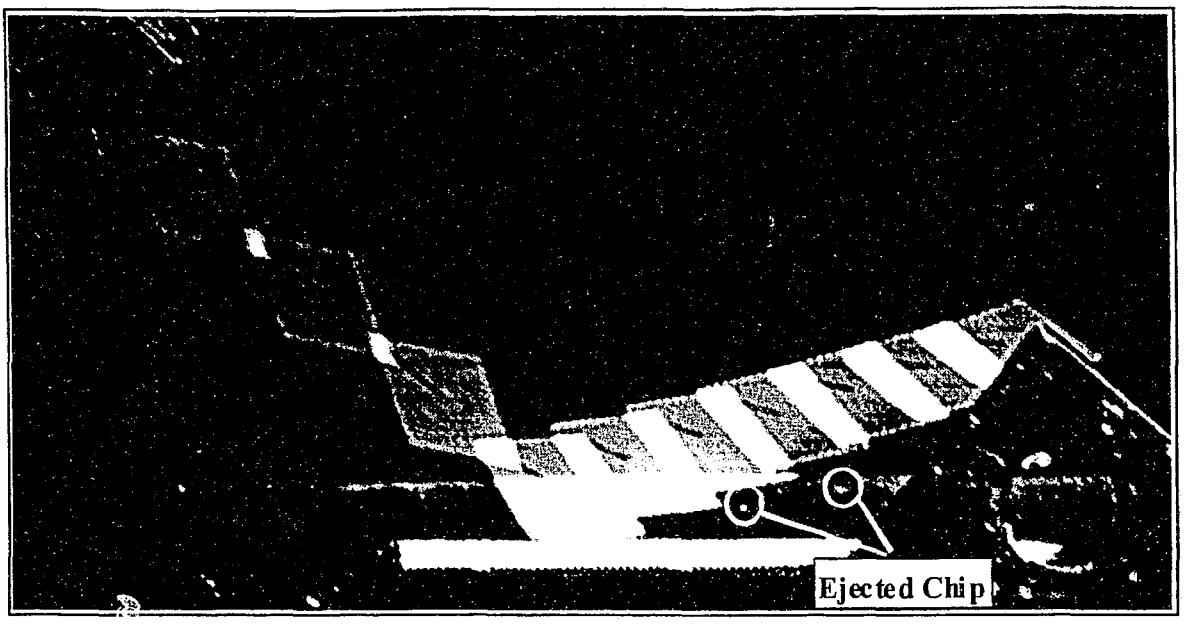

Fig 4.7: Impact of an angular particle (A=60°) that undergoes a backwards rotation (incident conditions: α_i=40°, θ_i = 55°, V_i=25 m/s, $\dot{\theta}_i$ =120 rad/s) leading to two impacts, the first by the 60° vertex, and the second by the adjacent 120° vertex

In the case of backwards rotating particles, almost all of the experiments involved multiple impacts, the first, a pure machining action by the leading 60° vertex as the particle rotates backwards, followed almost immediately by a secondary impact (backwards rotating) by the adjacent 120° vertex. The secondary crater profile is smaller in both depth and length than the primary crater profile (Fig. 4.8).

Previous studies involving impact of square plates [9] have also reported the removal a machined chip for backwards rotating particles, and attributed the behaviour to a pure micro-machining mechanism involving the cutting of the entire chip by the leading edge of the particle. In the present study, however, this pure cutting action occurred only up to a point. Sometimes, the chip appeared to break off prior to completion of the cutting action, resulting in the jagged crater edge seen in Fig. 4.8.

This behavior is most likely related to the fact that particles with high angularity (i.e. A>45°) launched at shallow incidence tend to "tunnel" below the surface; i.e. both of the

leading edges of the impacting particle vertex in Fig. 4.9 b are below the undisturbed surface. As the particle rotates, it tends to "pry off" a chip of material, which suddenly breaks off at some point during the impact (Fig.4.9.c).

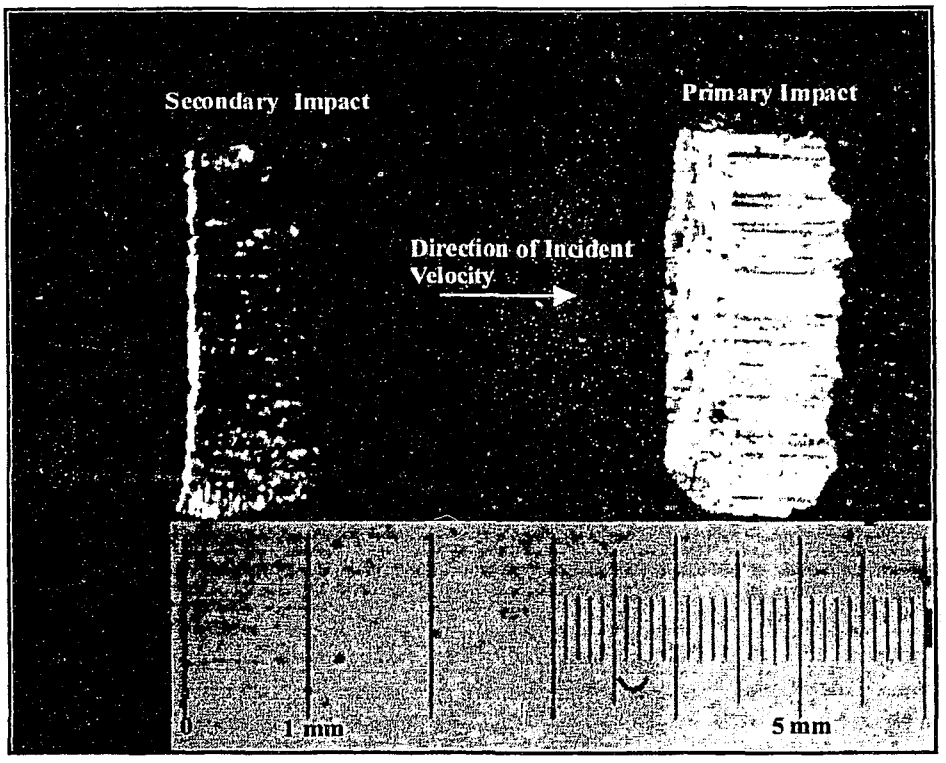

Fig 4.8: Craters left by an angular particle (A=60°) that underwent backward rotation. The bigger crater was the primary crater cut by the leading edge followed by the smaller crater cut by the adjacent edge

The collision kinematics thus become very sensitive to the point at which chip removal occurs. This tunneling action has not been previously reported, most likely because impacts with only square particles, for which tunneling is virtually impossible, have been previously studied.

Another example of this behaviour is shown in Fig.4.10 (a), where it can be seen that, while the particle did indeed rotate backwards, it did not, however, result in a pure machining action of the type reported by Hutchings [9], and seen in Fig. 4.7 (i.e. the cutting of a smooth crater as the particle swept along the surface resulting in a rebound

angle less than 90°). Rather, the leading vertex of the particle tunneled into the target, and when it rotated to the point where it was lying on its side, a chip was ejected at approximately 90° to the leftmost edge. The rebound angle of the particle was greater than 90°, and the resulting crater is shown in Fig. 4.10(b). Raised target material can be seen at the leading edge of the crater, where the leading vertex of the impacting particle tunneled below the surface.

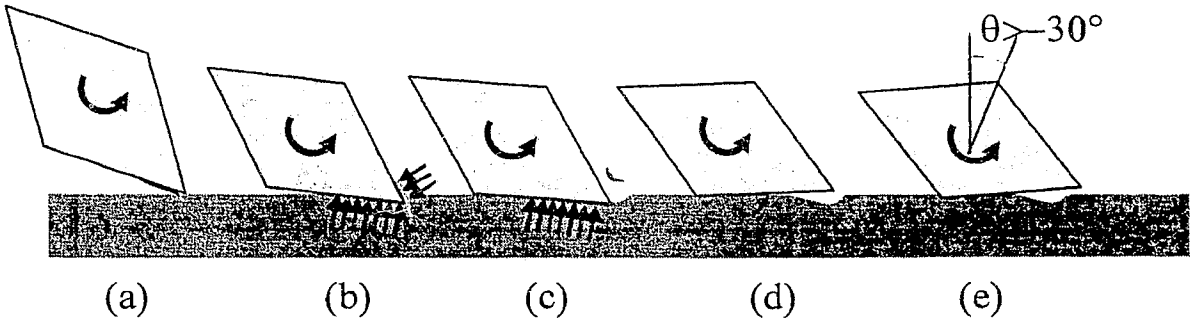

Fig. 4.9: Typical backwards rotating impact: (a) Incident condition (b) Particle tunnelling below the surface; and both the top and bottom leading edges of the particle are subject to contact forces (c) Chip breaks off at a certain point during impact, and only one contact force remains (d) Particle rotates freely (e) Secondary impacts occurs with an orientation slightly shallower than predicted.

A typical case of particle embedding at transition for A=60° particle is shown in Fig. 4.11 (a) where the particle losses all its kinetic energy in the plastic deformation of the target material, thus creating craters of maximum volume. A detailed study on the crater volumes is discussed in section 4.6. It is evident from Fig. 4.11 (b) that with a small change in the orientation angle θ_i, the rotation of the particle changes from forward to backward. The tunneling of the particle below the chip does not always result in chip removal. Fig. 4.12 illustrates the sequence of impacts at same angle of attack, but different orientation angles for A=80° particles. While tunneling appears to occur in all the three cases shown in Fig. 4.12, the chip remains attached. The high angularity associated with the A=80° particles, results in a very deep indentation, and the chip slides over the top face of the particle, which resists the rebound motion of the particle and influences the rebound kinematics.

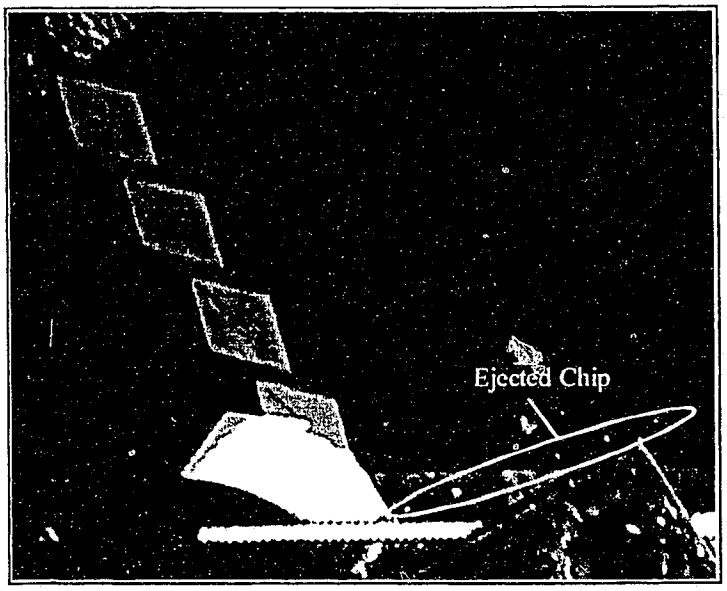

(a)

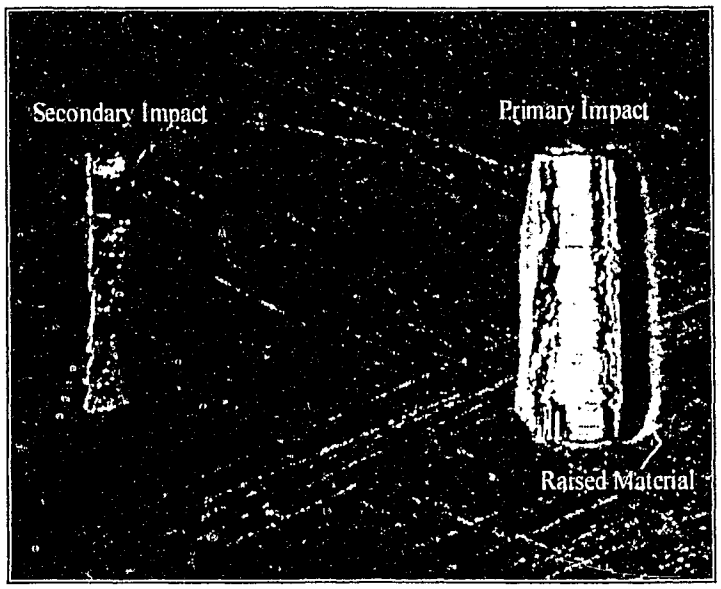

(b)

Fig 4.10: (a) Backwards rotating impact with a rebound angle greater than 90°. Chip is ejected perpendicular to the leading edge. (b) Crater corresponding to impact of Fig. 10 (a). Note the raised material ahead of the primary crater above where the particle leading edges had tunneled below the surface.

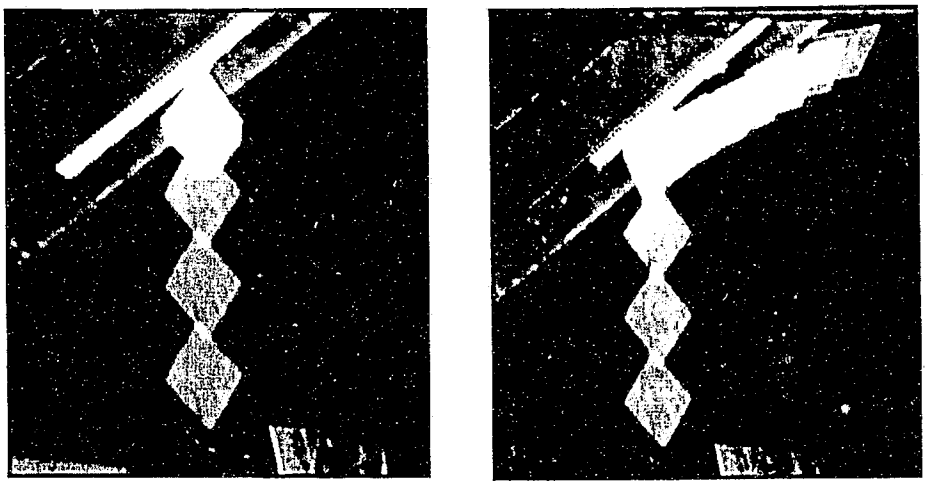

(a) (b)

Fig. 4.11: Impact near the transition between forward and backward rotation: (a) Embedding at θ_i=43.7°, and (b) Backward rotation of particle at θ_i=47.6°. In both cases A=60°, α_i=44° and V_i=24.5 m/s.

(a) (b) (c)

Fig. 4.12: Tunneling effect for A=80° particle: (a) forward rotation, (θ_i=59°), (b) at transition (θ_i=60°), and (c) backward rotation (θ_i=61°). In all cases, α_i =30° and V_i=24 m/s

4.2 Condition for Particle Embedding

Papini and Spelt [2, 3] noted that the energy consumption increases at high angles of attack. At angles of attack close to α=90°, a particle is likely to lose all its energy at some point during the impact and remain embedded. This, of course, assumes that there is no spring back of the target material. Papini and Spelt developed conditions for angular particle embedding into the target material, based on the principle of conservation of energy, where all the incident kinetic energy is converted to plastic work (i.e. crater formation). They suggested that the embedding condition, neglecting friction, gives that the product of dynamic hardness, P_d, and final crater volume (cross sectional area A_{cr} times unit thickness of the particle) is approximately equal to the total incident energy of the particle, or on a per unit width basis, given by [2, 3] :

$$P_d A_{cr} = \frac{1}{2} m V_i^2 \tag{4.1}$$

The mass per unit width of the particle, m, is [2, 3]

$$m = 2\rho h^2 \cos(A)\sin(A) \tag{4.2}$$

where, ρ is the density, A is the particle angularity, and h is the particle width .

However, in reality, frictional forces resist the motion of the particle as it moves through the target, forming the crater, and a part of the incident energy is lost in overcoming friction. The above equations can be rewritten for particle embedding conditions taking frictional forces into account.

$$P_d A_{cr} + \text{Frictional Energy Loss} = \frac{1}{2} m V_i^2 \tag{4.3}$$

Embedding could be noticed in cases where the particle struck the target surface at incident angles close to normal to the surface [3]. The embedding condition is useful for measurement of the dynamic hardness P_d, of the target (see Section 4.3).

4.3 Measurement of dynamic hardness and friction coefficient

The previously developed computer simulation [2,3] requires both the dynamic hardness, P_d, and friction coefficient, μ, as inputs. Dynamic hardness depends on the plastic flow field in the target material below the impact, and is a measure of the resistance to plastic indentation [9, 14, 18]. In rigid-plastic theory, an average value of dynamic hardness, assumed constant, is assumed to adequately describe the force resisting the indentation. The dynamic hardness is, of course, much higher than the quasi-static indentation hardness of the target; however, it is assumed that at such high rates of strain, the value remains relatively constant over the range of strains and strain rates occurring during the impact.

In the past, for impacts involving spherical particles, these parameters have either been chosen to best fit the experimental data (e.g. [18]), or by using an energy balance method [10] that involves the measurement of crater dimensions for embedding impacts performed at normal incidence. In the present work, a combination of the two methods was used. For a two-dimensional diamond shaped particle launched at normal incidence (α=90°) and θ=0°, with zero rotational velocity, the particle will stay in full contact with the target for the duration of the impact, and, neglecting elastic effects, lose all of its kinetic energy to plastic work. Referring to Fig. 4.13, setting the incident kinetic energy equal to the plastic work done in deforming the target, gives:

$$\frac{1}{2}mV^2 = \int_0^{\delta_{max}} 2P\left[\cos A + \mu\cos\left(\frac{\pi}{2}-A\right)\right]d\delta \qquad (4.4)$$

where P is the normal contact force developed on each face, m is the mass of the particle, V is the incident particle velocity, δ_{max} is the maximum penetration of the particle, and A is the angularity of the particle. The assumptions of rigid plastic theory give that $P=P_dLw$, where w is the thickness of the particle (out of plane), and geometry gives that $L=\delta/\cos(\pi/2-A)$. Substituting these expressions into eq. 4.4, integrating, and solving for the dynamic hardness, P_d, gives:

$$P_d = \frac{1}{2}\frac{mV^2}{w\delta_{max}^2\left[\tan\left(\frac{\pi}{2}-A\right)+\mu\right]} \tag{4.5}$$

In contrast to impacts involving spherical particles which gave, at normal incidence, a unique P_d for a given crater dimension, eq. 4.5 shows that there are an infinite number of combinations of P_d and μ that might result in a given crater dimension for impacts of two-dimensional diamond shaped particles at normal incidence. Neglecting pileup at the edge of the craters, the relationship between the maximum depth, δ_{max} and the length of the crater, 2d, is $\delta_{max}=d/\tan(\pi/2-A)$, so that a measurement of the length of the crater will give the possible combinations of P_d and μ via eq. 4.5. Impact experiments performed using A=60° particles gave a crater depth of 0.48 mm (average of 5 measurements) leading to the curve in Fig. 4.14. A single combination of P_d=440 MPa and μ=0.3 was thus chosen from Fig. 4.14 such as to give a best fit to all the experimental results. Similarly, this methodology was applied for determining the combination of coefficient of friction and dynamic hardness for particles with angularities A=30°, 45°, 80°. The calculated values of coefficient of friction μ, for dynamic hardness P_d = 440 MPa corresponding to particles with angularities A=30°, 45°, 80° were: 0.42, 0.39, 0.21 respectively.

In all cases, regardless of angularity, the value of P_d was kept constant and the fiction coefficient μ, was varied to fit the experimental results with the model predictions. This methodology was also tested by keeping the friction coefficient μ, constant and varying the dynamic hardness P_d. It was noticed that both methods yielded reasonable experimental and model agreement. Furthermore, the dynamic coefficient of sliding friction μ, is a function of the local sliding velocity, which changes with the angularity of the particles, a fact also noted in the results of the finite element model predictions (see Chapter 5). Taking all these facts in consideration, the P_d was kept constant, and the friction coefficient μ, was varied with angularity, for all calculations.

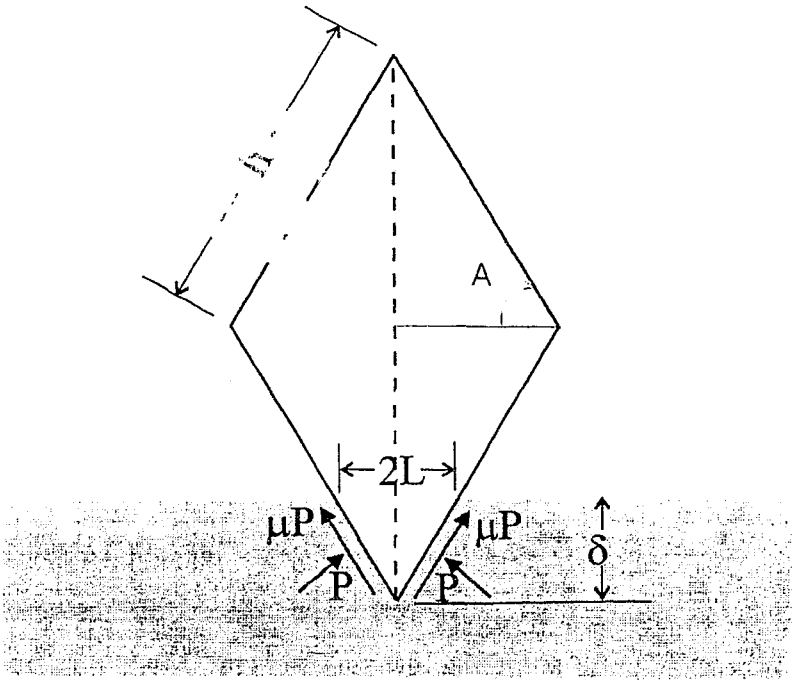

Fig. 4.13 Forces acting on particle when impacting at normal incidence (α=90°) with θ_i=0°, at =0 rad/sec

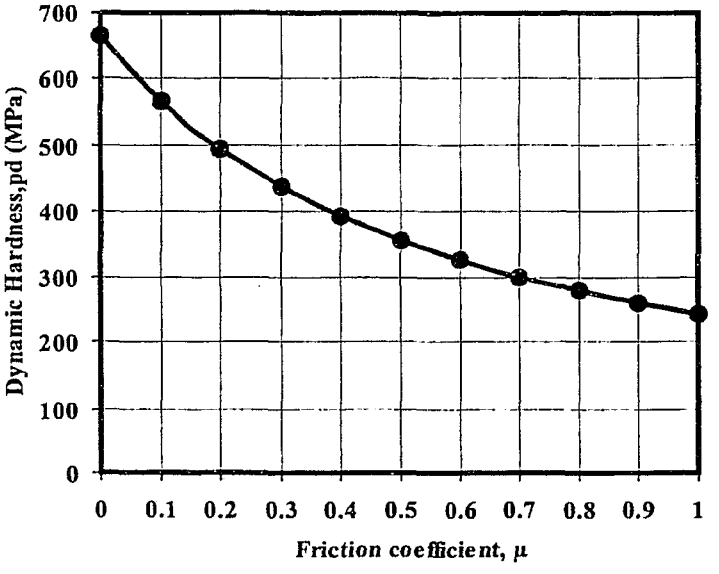

Fig. 4.14 Combinations of p_d, dynamic hardness, and μ, friction coefficient (see eq.4.5), which give predicted crater dimensions that fit measured ones for experiments of the type depicted in Fig. 4.13

4.4 Simulation of Experiments Using Rigid Plastic Model

The material properties of the target material,. the dynamic hardness, P_d = 440 MPa, the density of steel particle, ρ=8028.5 kg/m^3, and the friction coefficient, μ (which depended on the angularity of the particle) were inserted into the computer model developed by Papini [2, 3] implemented in MathCAD 11 (Mathsoft Inc, Cambridge, MA), to simulate the particle impact and predict the particle trajectory, crater profile and volume. A description of the model is given in Chapter 2, (section 2.3.1.4).

As the model is based on solving the differential equations of motion in time steps, the required time step was determined by decreasing it until the model showed convergence, i.e. the difference in rebound parameters between successive runs of the model, was less than 1%. The final time step used in all simulated results varied between 0.01 and 0.2 μs, which corresponds to approximately 0.5% of the impact duration, but this of course depends on the particular input parameters. A detailed algorithm describing the simulation program is given in reference [2].

The crater volume per unit width (A_c) was examined as a function of particle side length, h, angularity A, initial particle orientation θ_i, initial velocity V_i, target dynamic hardness P_d, and friction coefficient μ. The results, together with the results obtained via the rigid plastic theory are presented in Tables A.1-A.23 in the Appendix.

4.4.1 Simulation of forward impacts: particle trajectory and crater profiles

A typical particle trajectory, obtained with the computer implementation of the model for a forward rotating 60° particle, is shown in Fig. 4.15. The position of the particle is shown every 2 μs, as the particle travels from left to right. Similar simulations were also conducted for particles of 45°, 30°and 80° angularity (see Fig.4.16 for A=80° particle). As was discussed in Section 4.1.1, simulated collisions in which forward rotation occurred resulted in deeper craters and greater crater volumes, a result also noted by Hutchings [9].

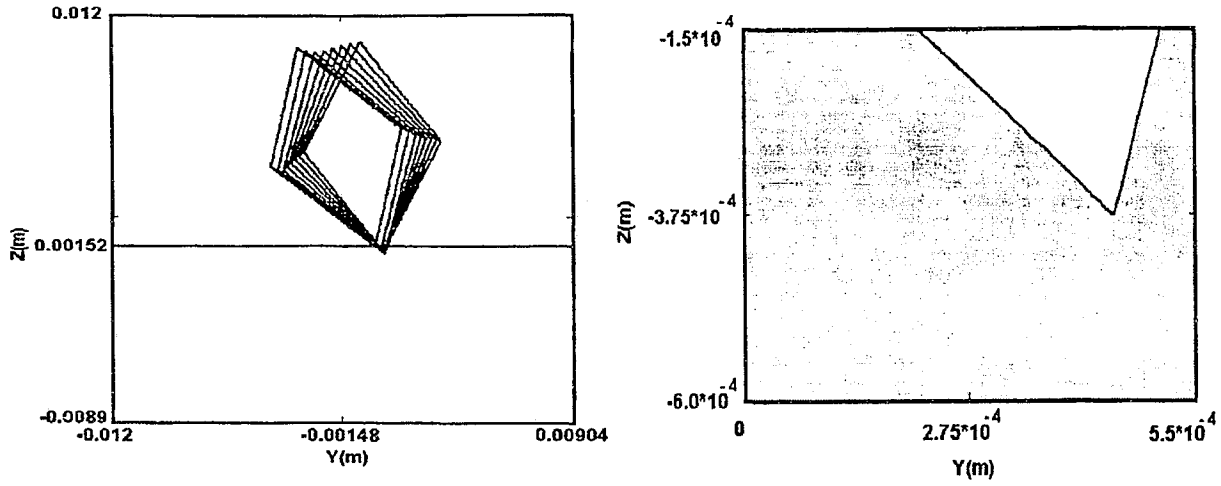

Fig. 4.15: (a) Particle trajectories and (b) crater profile at 0.2 μs intervals, obtained for forward rotation of A=60° particle (with impact conditions of α=30°, θ_i = 18.9°, $\dot{\theta}_i$ =0, V_i =24.5 m/s, and particle side length, h=6.36 mm, P_d=440 MPa and μ=0.32)

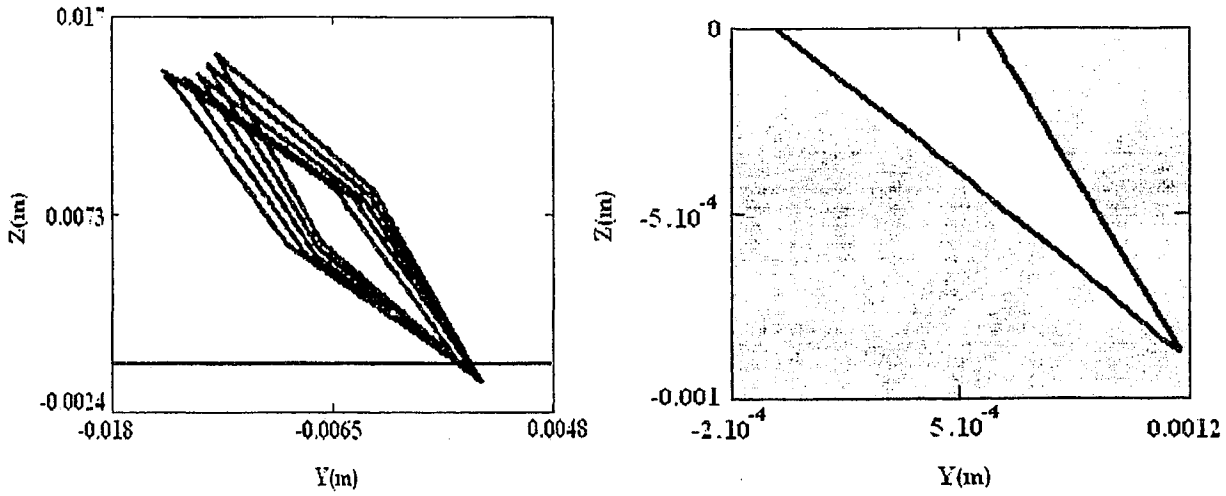

Fig. 4.16: (a) Particle trajectories and (b) crater profile at 0.2 μs intervals, obtained for forward rotation of A=80° particle (with impact conditions of α=30°, θ_i = 47°, $\dot{\theta}_i$ =0, V_i =25 m/s, and particle side length, h=10.68 mm, Pd=440 MPa and μ=0.21)

4.4.2 Simulation of backwards impacts: particle trajectory and crater profiles

Simulations of the backward impacts were conducted in a similar manner to that as explained in section 4.1.2. Fig. 4.17 illustrates backward rotation of the particle. It can be noticed that the particle machines the target with complete removal of material from its surface, resulting in long and shallow craters similar to the experimental behavior.

In most of the impact cases involving backward rotations, the simulated impact consisted of two collisions, the primary crater cut by the leading edge followed by the secondary crater cut by the adjacent vertex of the angular particle. The simulation predicted the magnitude of length and depth for the primary crater to be greater than the secondary crater, just as was seen with the experiments (Fig.4.17).

4.4.2.1 Simulation of multiple impacts: Particle Trajectory and Crater Profile

The computer model as presented in Refs. [2, 3] considered only a single impact at a time, and thus could be used to directly predict the rebound kinematics of the particle, for comparison with the experimental results, only in the case of single impacts.

In some experimental cases, multiple impacts occurred, and one or more secondary impacts occurred by the adjacent vertex of the particle. The adjacent vertex that impacted next depended on the type of rotation of the particle i.e. forward or backward. The computer simulation computed the direction of the components of the resultant linear velocity vectors obtained at the end of primary impact and successfully predicted if the particle was heading towards or away from the target material. Secondary impacts in the case of forward rotations could be mostly seen in conditions where the initial orientation angle was negative for the particle impacting the target material. Examples of such impacts are given in Table A.1 (see appendix).

The rebound angular and linear velocities, and the orientation at the end of the first impact could be used to calculate the trajectory and rotation of the particle as it traveled through the air between impacts, so that the orientation, velocity and angle of attack of the particle upon secondary impact, could be predicted, and used as input conditions in the model to calculate the kinematics of the secondary impact.

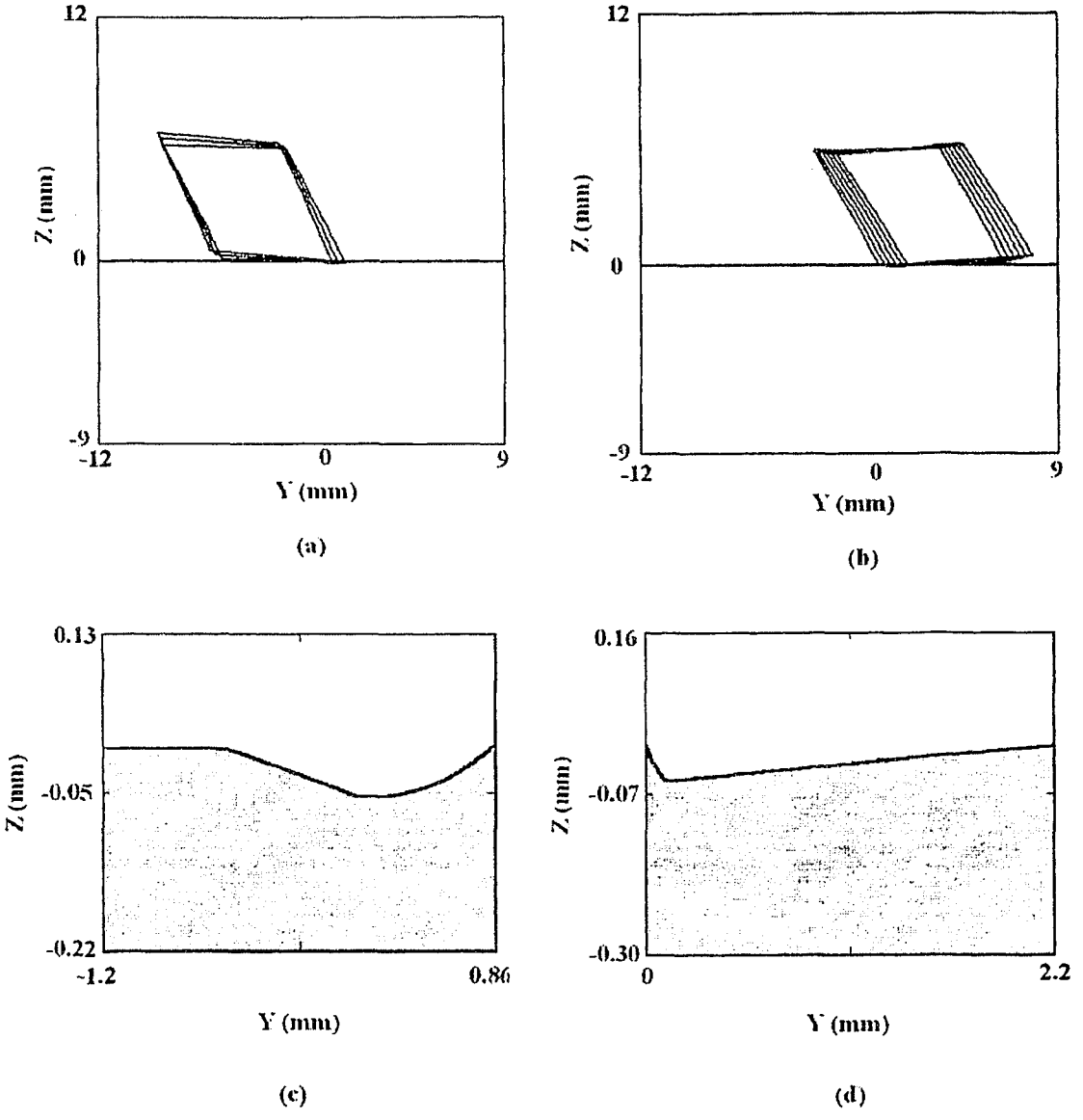

Fig. 4.17: Simulated particle impacts for experiment shown in Fig.4.7: (a) First impact (particle drawn every 12 μs) (b) Second impact (particle drawn every 16 μs) (c) Crater for first impact (d) Crater for second impact

The incident angle of attack and velocity of the particle upon secondary attack could be obtained directly from the conditions at the end of the first impact. However the orientation upon second impact required calculation. Equations 4.6 (a) and (b) govern the movement of the particle through the air at constant velocity.

$$[Z_{ver}]_f = [Z_{ver}]_i + \frac{d}{dt}[Z_{ver}] \times t \qquad (4.6).a$$

$$\theta_f = \theta_i + \dot{\theta} \times t \qquad (4.6).b$$

Where Z_{ver} is Z-coordinate of the adjacent vertex, and the subscripts i and f, refer to initial (at the end of the first impact) and final (at the onset of the second impact) conditions, respectively, and t, the time the particle rotated freely in the air between impacts. $[Z_{ver}]i$ can be obtained by inserting the first impact rebound parameters into the inertial frame coordinate equation eq. 2.7 (Section 2.3.1.4), while θ_i and $\dot{\theta}$, are obtained directly from the first impact rebound condition. An expression for the velocity of the vertex, $\frac{d}{dt}[Z_{ver}]$, was obtained by differentiating eq. (2.7). Because, at the moment of secondary impact, the condition $[Z_{ver}]_f = 0$ holds, eq. 4.6(a) can be solved for t, and inserted into eq. 4.6 (b) to obtain θ_f, the orientation for the secondary impact.

Impacts subsequent to secondary, if any, were calculated in the same manner, so that the full trajectory of the particle as it skipped across the surface could be obtained. As an example, Fig 4.18 shows the simulated trajectory of the particle and the resulting craters for conditions corresponding to those shown in Fig. 4.5. Noting that the scales on these diagrams are different, it is evident that the largest crater is the primary, followed by the secondary, and finally the third. It is worth noting that in all cases where secondary impacts were seen experimentally, the model also predicted a trajectory after initial impact that indicated a subsequent impact with an adjacent particle vertex.

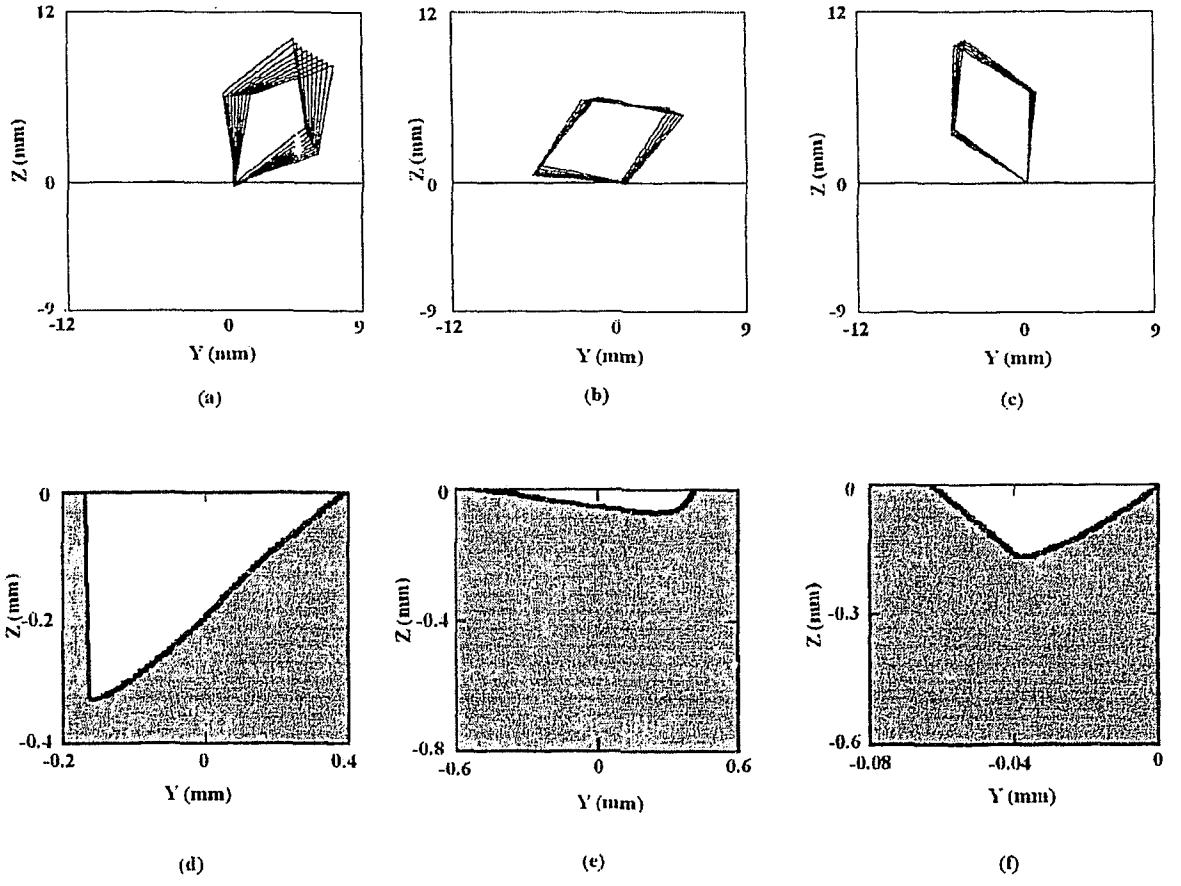

Fig. 4.18 :Simulated particle impacts for experiment shown in Fig. 4.5: (a) First impact (particle drawn every 14 μs) (b) Second impact (particle drawn every 16 μs) (c) Third impact (particle drawn every 10 μs) (d) Crater for first impact (e) Crater for second impact (f) Crater for third impact.

4.4.3 Simulation of experiments involving chip break off/tunneling

For certain impacts, there were inconsistencies in break off point of the machined target material chip, as the particle tunneled below the surface, as explained in Section 4.1.2. This presented considerable difficulties when using the rigid plastic model, because it assumes that chip break off can only occur when the particle vertex has traveled through the surface and exited at Z=0 in Fig .4.1, and that the full contact force could always be supported by the chip that was being machined. This implies that the

force on the top of the particle in Fig.4.9a would exist for the entire duration of the impact. In this case, the secondary impact of the 120° vertex is predicted by the model to begin with the lower edge of the particle parallel to, and in full contact with, the target surface (i.e. at a secondary impact initial orientation angle of θ=-30°), and examination of the impact site should reveal some evidence of the impacting particle having contacted the surface along its entire lower edge. However, examination of Fig. 4.8 reveals two distinct impact sites. Moreover, were a pure machining action to be responsible for chip removal, one would expect the secondary crater to be located a distance h=6.36 mm away from the primary crater. Figure 4.8, however, shows that the distance between the craters is approximately 5.3 mm, which indicates that some free rotation of the particle must have occurred in the time between impacts.

In reality, it is unlikely that this full force would be supported by such a small piece of material, and the chip was thus likely to break off earlier. If earlier chip break off were to occur, there would instantaneously only be the force due to the lower contact segment (Fig.4.9c), resulting in an instantaneous increase in rotational velocity. This would lead to some free rotation of the particle prior to the onset of the secondary impact, and result in a slightly larger orientation angle than would have been predicted by assuming the chip stayed attached for the duration of the impact (i.e. θ >-30°), as demonstrated in Fig.4.9e. The actual change in orientation angle depends not only at which point the chip breaks off, but also the rotational velocity at that point, both of which are difficult to predict. However, it was found that by using the rebound conditions assuming no chip break off, but adjusting the initial orientation angle (θ_{adj}) for the secondary impact in the small range of -30°<θ<-28°, the data generated by the model, generally agreed well with experimental results, as shown in Table A.3. Figure 4.17 shows the simulated trajectory of the particle and the resulting craters, for conditions corresponding to those shown in Fig. 4.7, using the described technique.

In addition to the chip break off, sliding of lower edge of the particle over the material piled up at the edge of the primary crater may also increase the orientation angle for the secondary impact. It is however unfortunately not possible to quantify this effect. The conditions leading to chip break off are also discussed in detail in Chapter 5.

4.5 Particle Kinematics: Comparison of Simulated and Experimental Results

In this section a detailed study is undertaken to compare the experimental and model predicted data obtained for various impact conditions for particles with different angularities. In general, a good agreement is found between the actual and the predicted results. For all the angularity particles, the forward rotations were successfully obtained. The backward rotations, which occurred over only a limited range of incident conditions, were obtained for A=45° and A=60° particles only, because of difficulties in obtaining 2D planar impacts for A=30° and A=80° particles.

4.5.1 Rebound Angle (α_r) and Rebound Velocity (V_r)

Figures 4.19-4.22, compare predicted (i.e. from the rigid plastic model) and experimental rebound angles, for A=60°, 45°, 80° and 30° particles, using the data from Tables A.1, A.3, A.13, A.15, A.19, and A.21 given in the Appendix. The rebound angle predicted by the model was typically shallower (average of 3° for forward rotating particles and 10° for backwards rotating particles) than that measured for A=60° particle (Fig. 4.19 a and Fig. 4.19b). Similar observations where the rebound angles were comparatively greater for the experimental results as compared to their corresponding model predictions were seen for A=45° (Fig. 4.20), A=80° (Fig. 4.21) and A=30° (Fig. 4.22). This phenomenon was also noted in the rigid-plastic simulation of spherical impacts by a number of investigators (e.g. [10, 14, 22]), and is likely due to a combination of two effects:

(i) The target material is plastically deformed, and the volume of material indented by the impacting particle is ploughed to the edges of the crater in form of a lip (Figs. 4.3 and 4.4). The actual instantaneous contact area between the leading edge of the particle and the target material would thus be higher than that seen in the model, which cannot account for this pileup. This would deflect a forward rotating particle at a steeper angle than the model, which cannot account for this pileup effect.

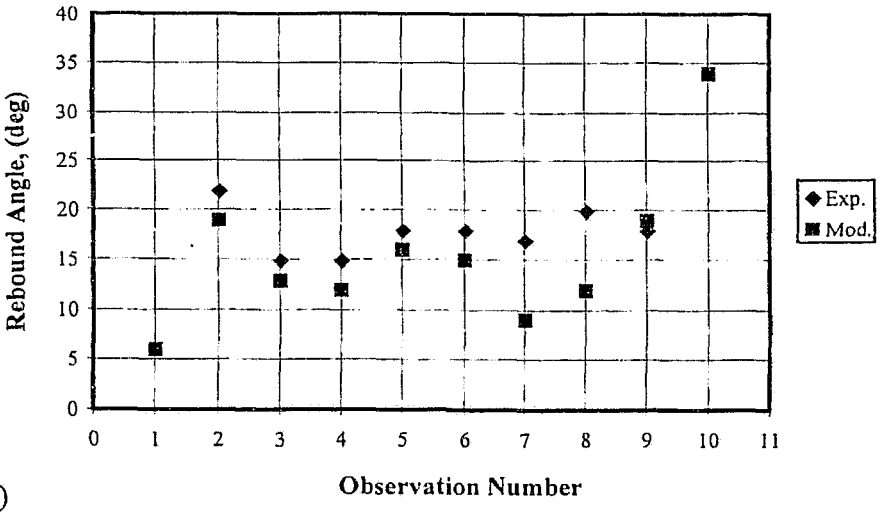

(a)

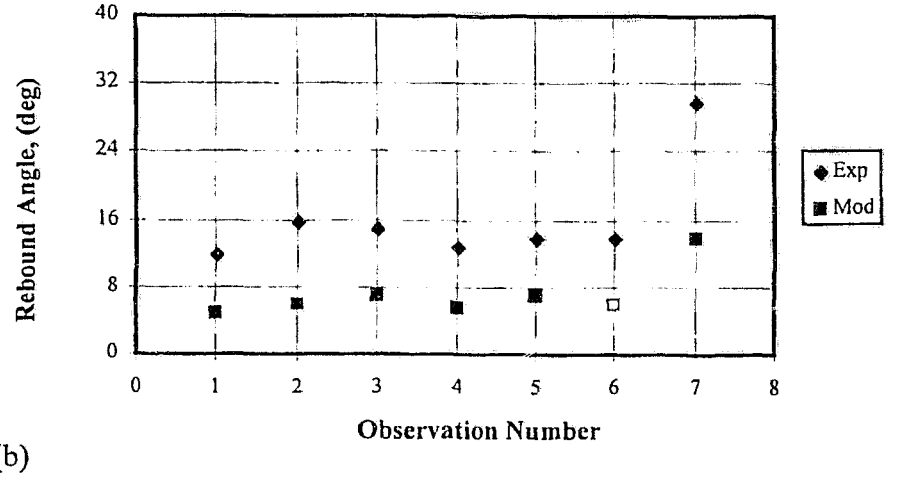

(b)

Fig.4.19: Comparison of predicted rigid plastic model (Mod) (■) and Experimental, (Exp) (♦) rebound angle α_{reb}, for A=60° particles, for (a): forward rotating particles, and. (b) backward rotating particles. Data is taken from Table A.1 and Table A.3.

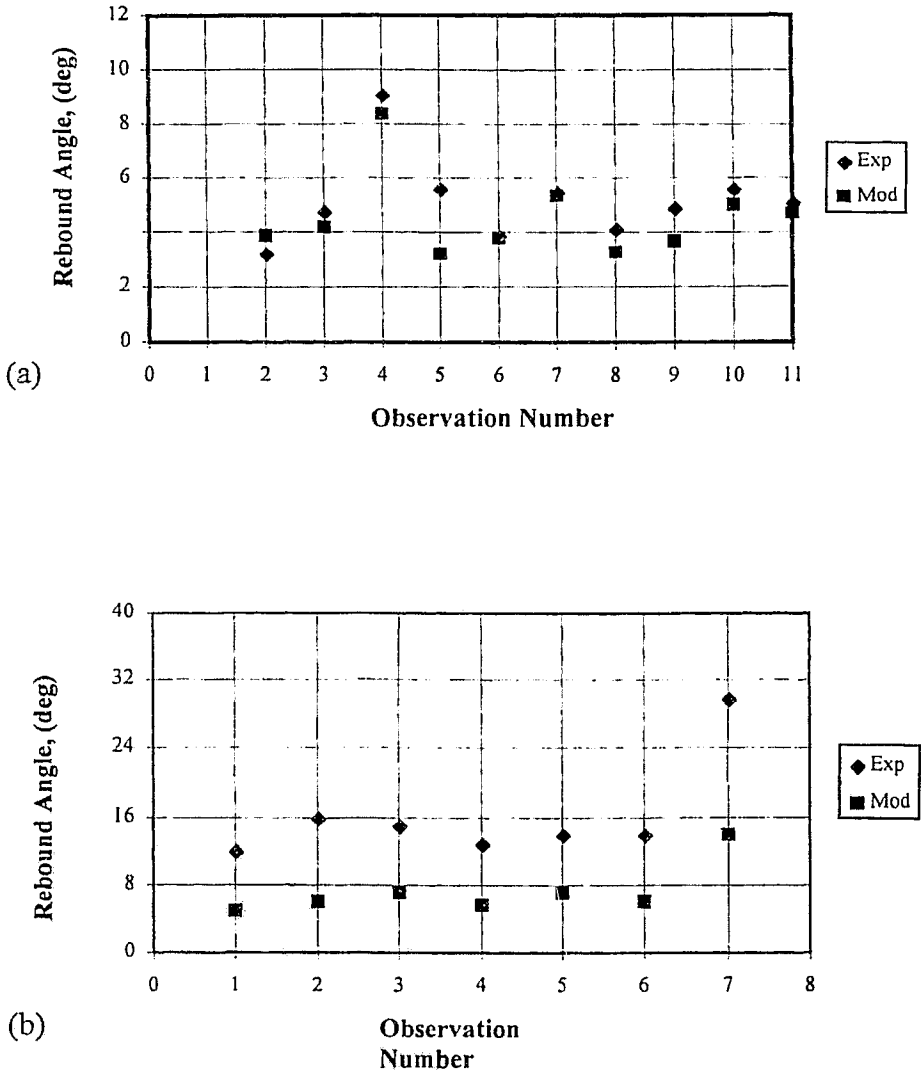

Fig. 4.20: Comparison of predicted rigid plastic model, (Mod) (■) and experimental, (Exp) (♦) rebound angle α_r, for A=45° particles, for (a): forward rotating particles, and. (b) backward rotating particles. Data is taken from Table A.13 and Table A.15.

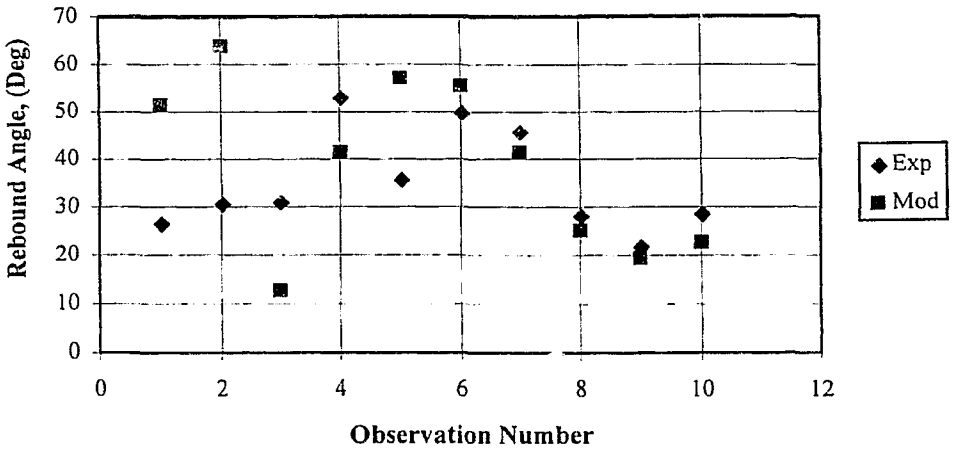

Fig.4.21: Comparison of predicted rigid plastic model, (Mod) (■) and Experimental, (Exp) (♦) rebound angle α_r, for forward rotating particles for A=80°. Data is taken from Table A.19.

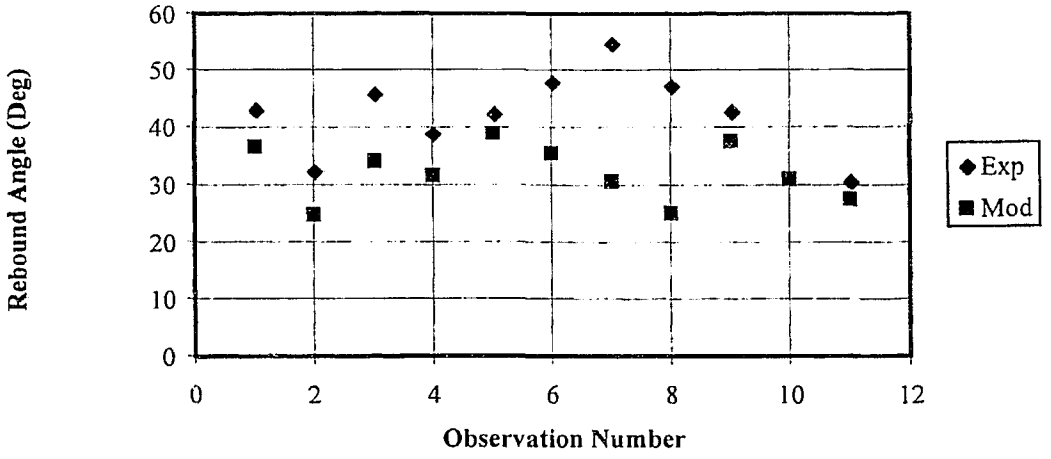

Fig.4.22: Comparison of predicted rigid plastic model (Mod) (■) and Experimental, (Exp) (♦) rebound angle α_r, for forward rotating particles for A=30° .Data is taken from Table A.21.

(ii) Elastic spring-back in the material is likely to give the rebounding particle additional velocity normal to the surface [9] which cannot be accounted for in the rigid-plastic model. It is noteworthy that the greatest error in rebound angle is found for backward rotating particles, which give long and shallow craters, which would be most susceptible to the effects of elastic spring-back.

Tables A.2, A.4, A.14, A.16, A.21 and A.23 show the percentage difference between the experimental and the model predictions. In case of A=60° particle (Table A.2 and Table A.4), for all experiments, the average percentage difference was 25% for forward rotations, and 102% for the backward rotations for A=60°. For A=45° particle (Table A.14 and Table A.16), the percentage error for backward rotations was higher (27.6%) as compared to forward rotation (20%).

Figure 4.23 compares the predicted (i.e. from the rigid plastic model) and experimental rebound velocities, for an A=80° particle, using the data from Table A.20. Similarly, the comparison of results for the various angularity particles are shown in Figs. 4.24 –4.26.

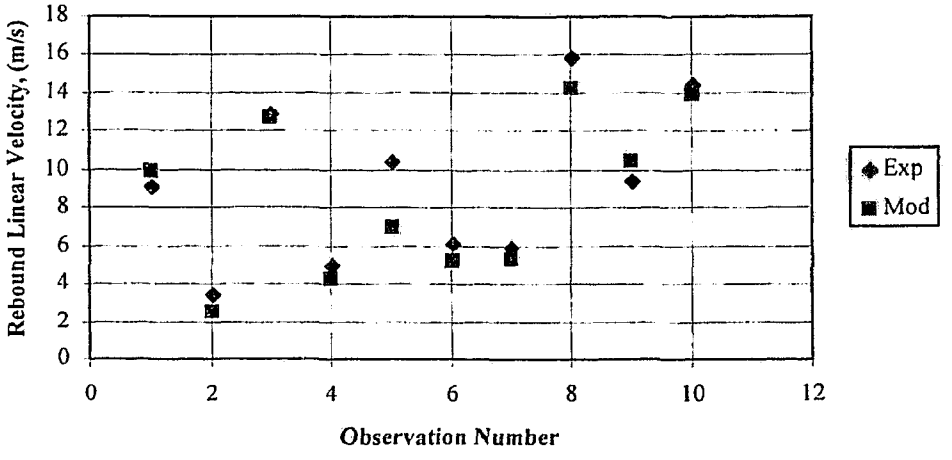

Fig. 4.23. Comparison of predicted rigid plastic model, (Mod) (■) and experimental, (Exp) (♦) rebound linear velocity V_r, for forward rotating particles for A=80°. Data is taken from Table A.19

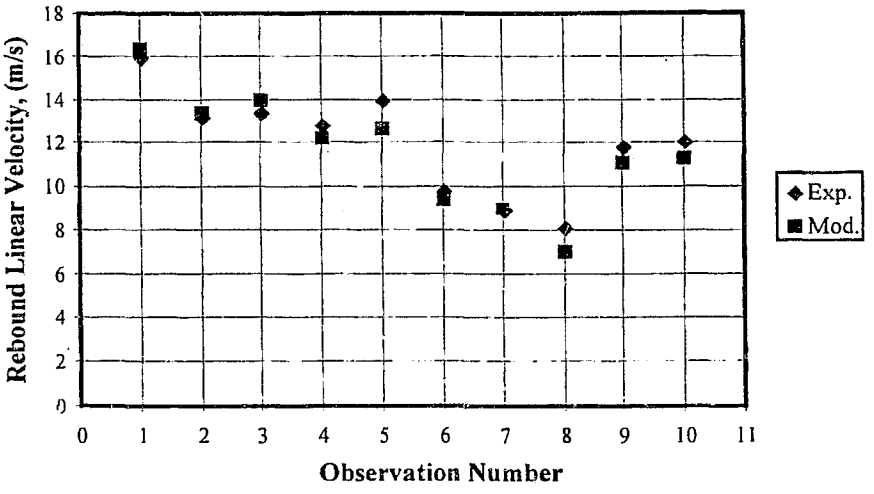

(a)

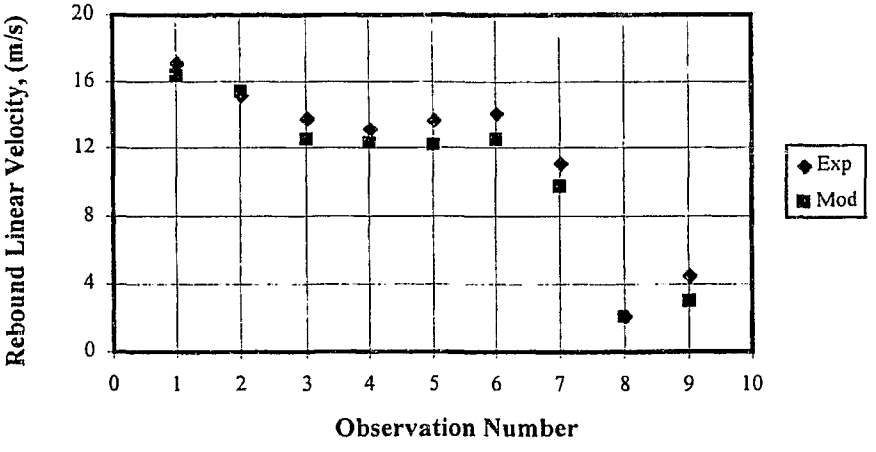

(b)

Fig.4.24: Comparison of predicted rigid plastic model (Mod) (■) and Experimental, (Exp) (♦) rebound linear velocity, V_r, for A=60° particles, for (a): forward rotating particles, and. (b) backward rotating particles. Data is taken from Tables A.1 and A.3.

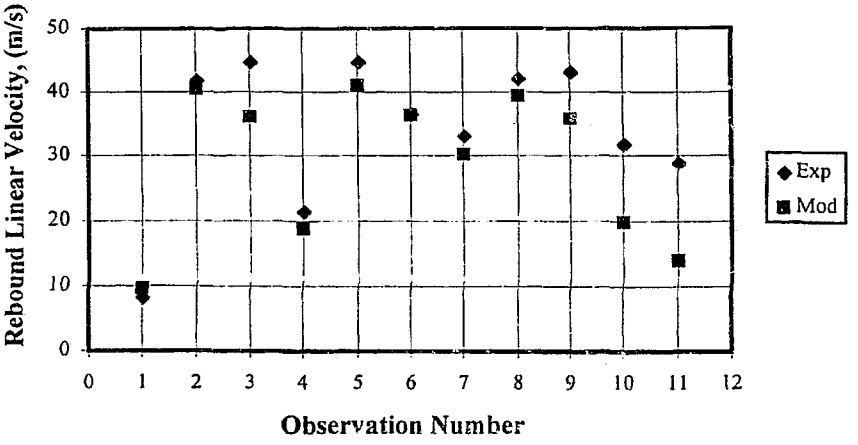

(a)

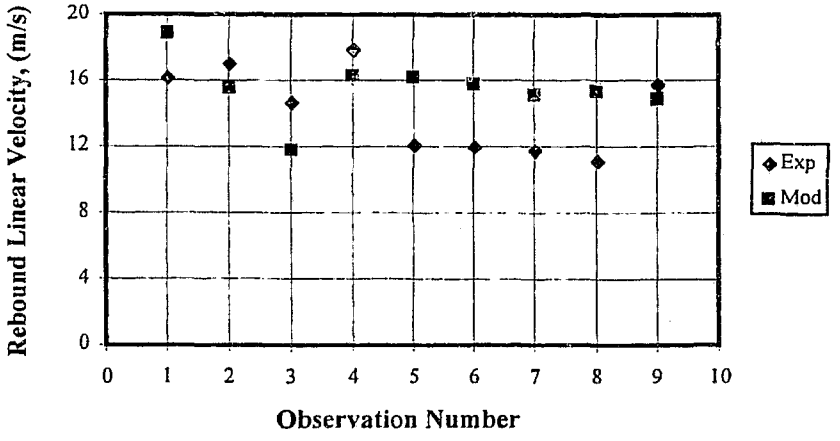

(b)

Fig. 4.25: Comparison of predicted rigid plastic model (Mod) (■) and Experimental, (Exp) (♦) rebound linear velocity, V_r, for A=45° particles, for (a): forward rotating particles, and. (b) backward rotating particles. Data is taken from Tables A.13 and A.15.

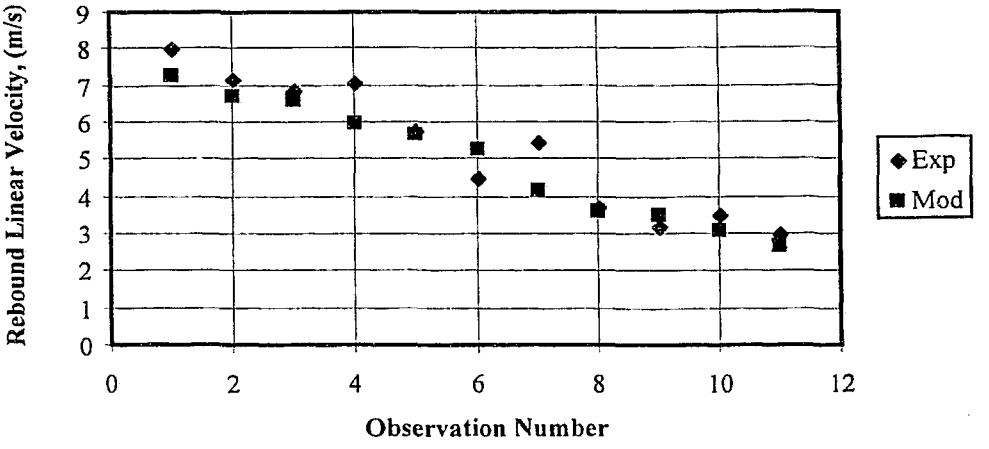

Fig.4.26: Comparison of predicted rigid plastic model (Mod) (■) and Experimental, (Exp) (♦) rebound linear velocity V_r, for forward rotating particles for A=30°. Data is taken from Table A.21.

While the agreement between experiments and predictions, in most cases, was fairly good, the experimental results were higher for both the forward (Fig.4.24a) and backward rotations (Fig.4.24b). This consistency in higher rebound linear velocities for the experimental cases for both the forward and backward rotations could also be seen for the other angularity particles (i.e. A=80°, 45°, 30°) in Figs 4.23, 4.25 and 4.26. The average difference for rebound linear velocity between the experimental and predicted results for all the particle cases was within 20% in both forward and backward rotations, as described in the percentage difference Tables A.2, A.4, A.14, A.16, A.21 and A.23 in the Appendix. The elastic spring back effect described could also be responsible for this discrepancy.

4.5.2 Rebound Rotational Velocity, $\dot{\theta}_r$

Figures 4.27 and 4.29 reveal that the rebound rotational velocity of the particle undergoing forward rotation is considerably higher than in the case of backward rotation. This is because a significant amount of the incident linear kinetic energy is converted to rotational energy, a fact also noted by Hutchings [9], for experiments involving square plates. The sign convention used here is negative for the clockwise rotations; hence a lower value indicates a higher forward rotational velocity.

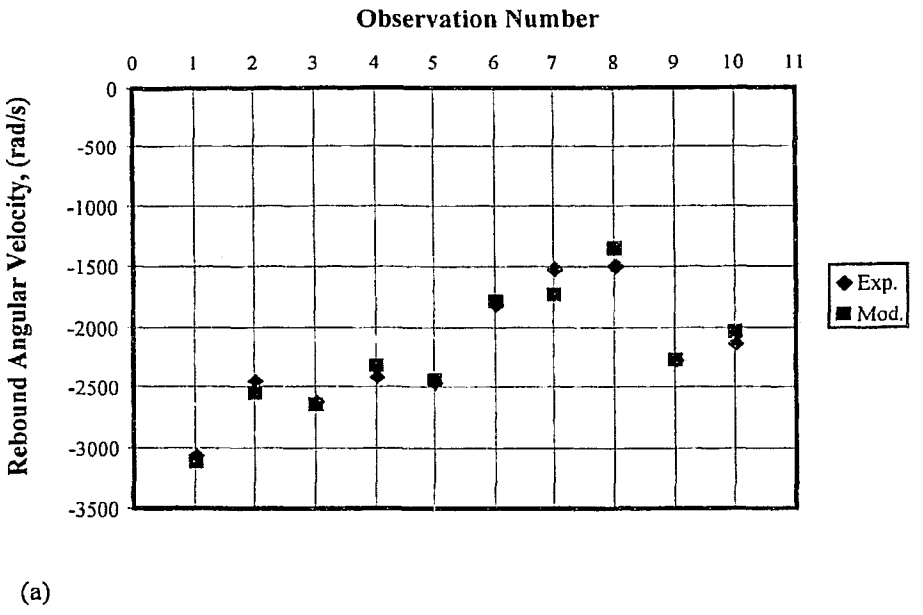

(a)

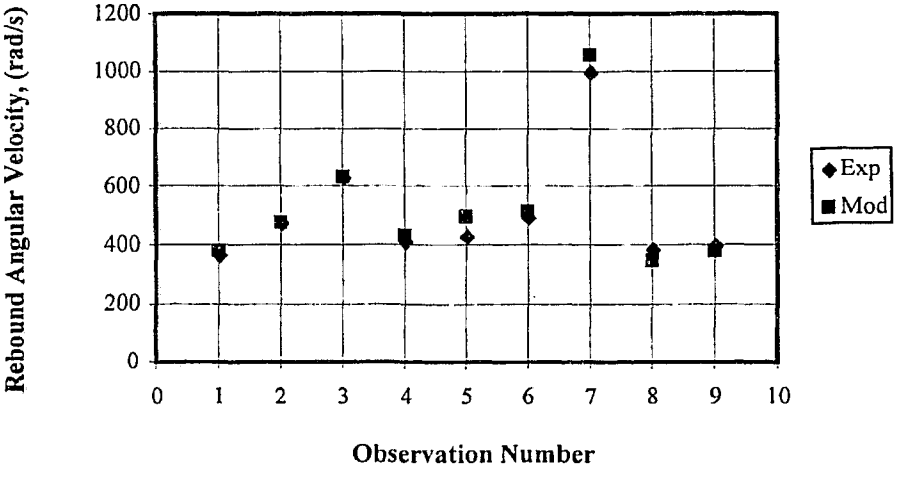

(b)

Fig. 4.27: Comparison of predicted rigid plastic model (Mod) (■) and experimental, (Exp) (♦) rebound angular velocity, for A=60° particles, for (a): forward rotating particles, and. (b) backward rotating particles. Data is taken from Tables A.1 and A.3

For most of the particles undergoing forward rotation, the rebound rotational velocity is generally higher for the experimental cases, as compared to the model predictions, as shown in Figs. 4.27a, 4.28, 4.29a and 4.30. The reason for this could be the influence of lip formation (i.e. pileup material) on the edge of the crater, which creates a resistance force acting on the side face of the particle, resulting in a resistance to its horizontal velocity. This resisting force acting at the side face of the cutting particle induces a couple in the particle with respect to its center of gravity, which increases the tumbling in the forward direction. The model cannot account for the material pile up, and thus this effect is unaccounted for.

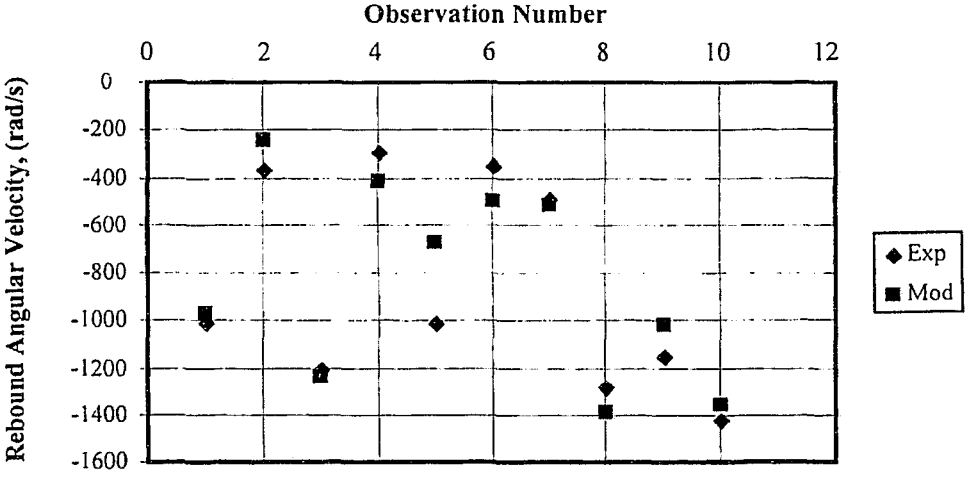

Fig.4.28: Comparison of predicted rigid plastic model, (Mod) (■) and experimental, (Exp) (♦) rebound angular velocity for forward rotating particles for A=80°. Data is taken from Table A.19

For the backward rotation cases, the particle maintained its trajectory, losing some of its incident energy in the formation of the primary crater, and rebounded with a relatively high rebound velocity (see, for example, Figs. 4.27 and 4.29). This resulted in low rebound rotational velocity at the end of secondary impact. For all particles (i.e. A=30°, 60°, 45°, 80°), the experimental results fit well with the predicted results for the forward and backward rotation with the average percentage difference being in the range of 4 - 18% as could be noted from Tables A.2, A.4, A.14, A.16, A.21 and A.23.

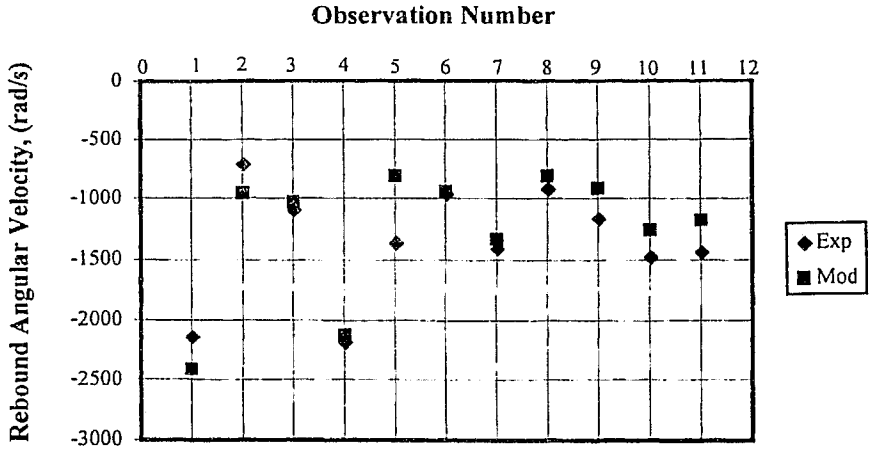

(a)

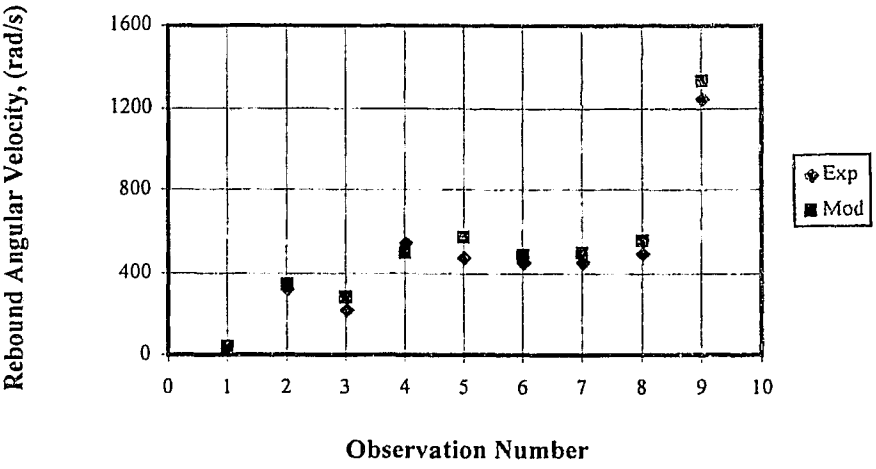

(b)

Fig. 4.29: Comparison of predicted rigid plastic model, (Mod) (■) and Experimental, (Exp) (♦) rebound angular velocity, for A=45° particles, for (a): forward rotating particles, and. (b) backward rotating particles. Data is taken from Tables A.13 and A.15

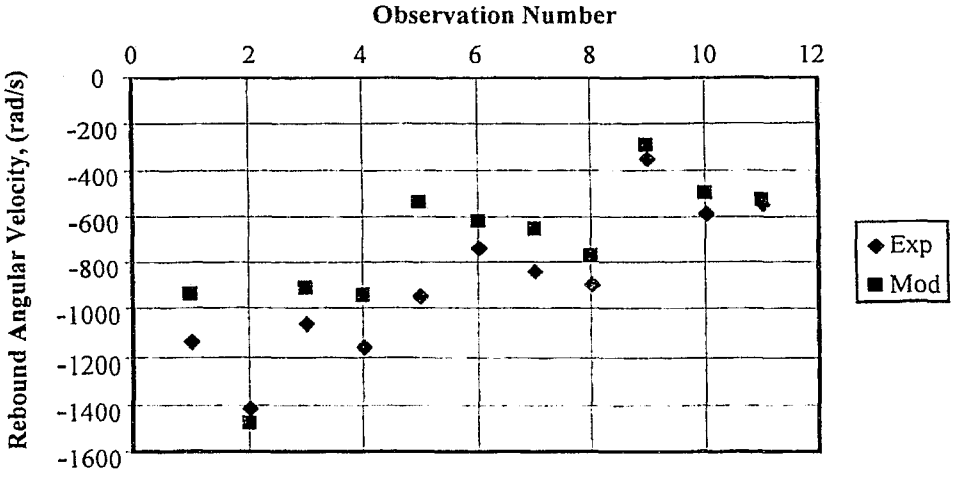

Fig.4.30: Comparison of Rigid plastic model predicted, (Mod) (■) and experimental, (Exp) (♦) rebound angular velocity for forward rotating particles for A=30°. Data is taken from Table A.21

In case of backward rotation (Figs. 4.27b and 4.29b), no consistent trend in difference between predicted and experimental results, in terms of being higher or lower, could be seen. This is most likely due to two effects:

(a) Most of the time, a primary impact was followed by a secondary impact. The model assumes that the particle machined the target surface in a smooth manner, but in reality, the roughened and jagged nature of the crater surface, as seen from the experimental crater profile (Fig. 4.8) influenced the rebound kinematics of the particle.

(b) The tunnelling effect of the leading edge of the particle as it cuts through the target material (as explained in section 4.1.2) and the inconsistencies in the chip break–off, influenced the force acting the on the leading particle edge.

4.5.3 Energy lost in collision (KE_{Loss})

The total energy lost during the collision is of particular importance, as it represents the work done in plastically deforming the target. As seen from Tables A.2, A.4, A.14, A.16, A.21 and A.23, the average percent difference between simulated and

experimental energy loss was 2-8%, for both forwards and backwards rotating particles. In most of the cases (Figs. 4.31-4.35), the model predicts higher energy consumption than the experimental results. This could be possible due to the spring-back effect in the crater (discussed in Section 4.5.1), which has been neglected in the rigid plastic model. As the energy lost in collision depends on the rebound linear velocity, the consumption in cases of experimental results are lower because the rebound linear velocity was found to be greater for experimental results, as is evident from Figs. 4.22-4.24.

Also noteworthy is that the energy losses, when expressed as a percentage of the initial kinetic energy, were greatest in Table A.5; i.e. for experiments conducted close to the transition orientation as compared to conditions which are far from the transition zone for both the forward and backward rotation of the particle (Fig. 4.33). Evidently, the lost energy goes to plastic work in creating the crater, rather than being converted into rebound rotational velocity. Similar behaviour was also noticed from the characteristic curves of Section 4.6.1, where KE_{loss} are higher at critical orientation angle θ_i^{crit} (i.e. orientation angle at transition).

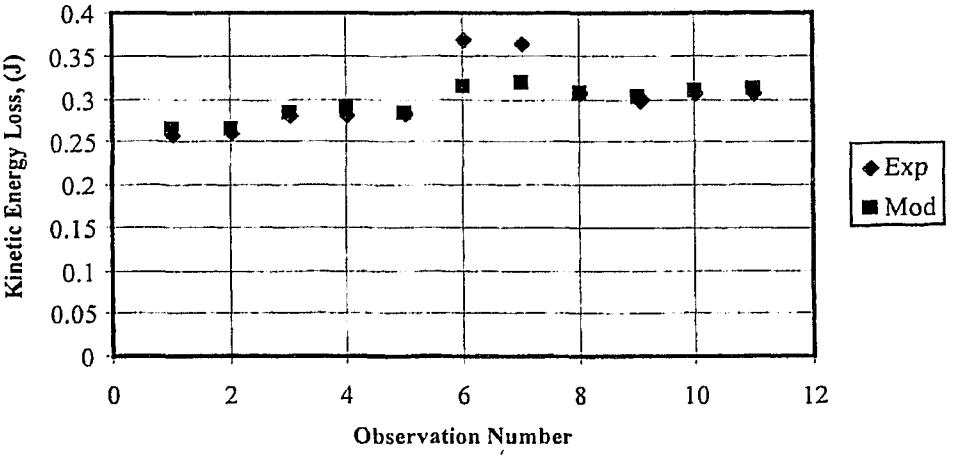

Fig. 4.31: Comparison of predicted rigid plastic model, (Mod) (■) and experimental, (Exp) (♦) Kinetic Energy Loss KE_{loss}, for forward rotating particles for A=30°. Data is taken from Table A.21

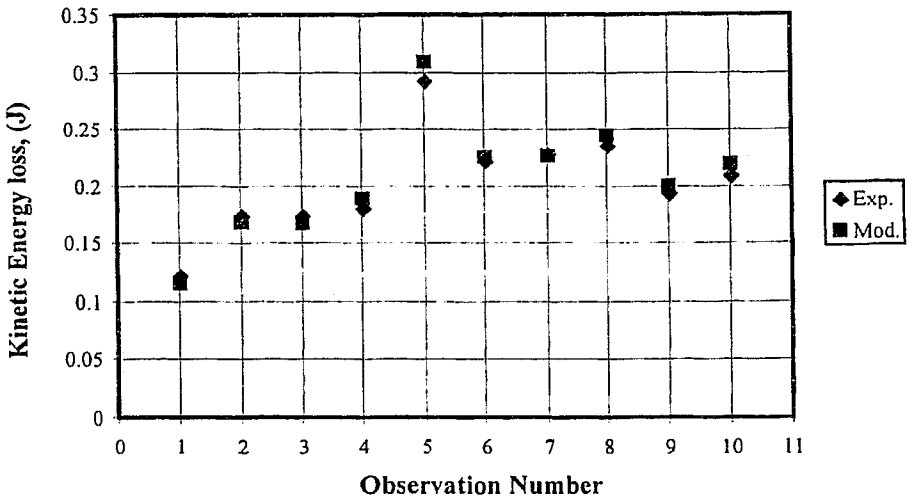

(a)

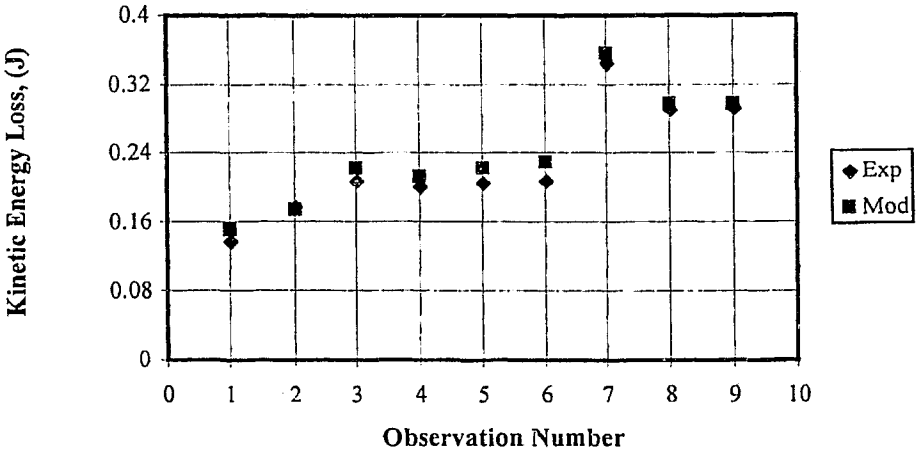

(b)

Fig.4.32: Comparison of predicted rigid plastic model, (Mod) (■) and experimental, (Exp) (♦) Kinetic Energy Loss KE_{loss}, for A=60° particles, for (a): forward rotating particles, and. (b) backward rotating particles. Data is taken from Tables A.1 and A.3

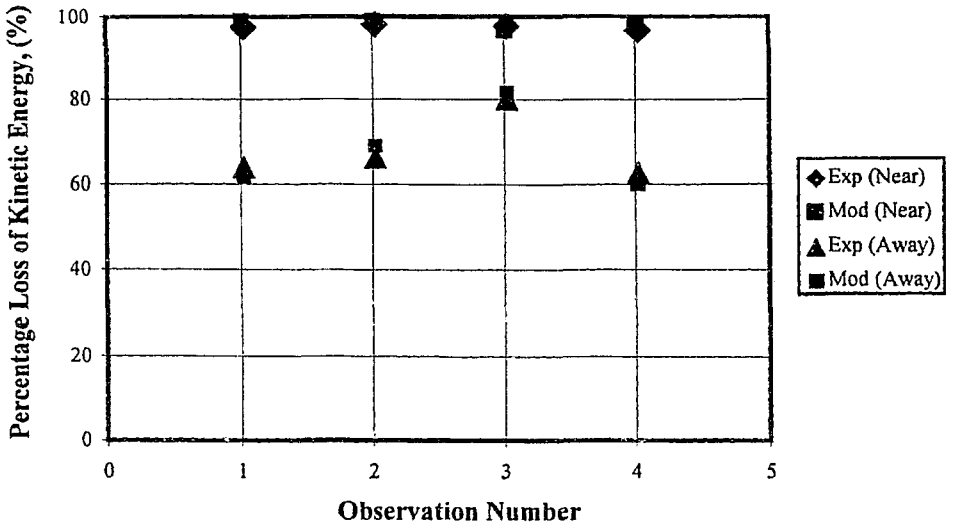

(a)

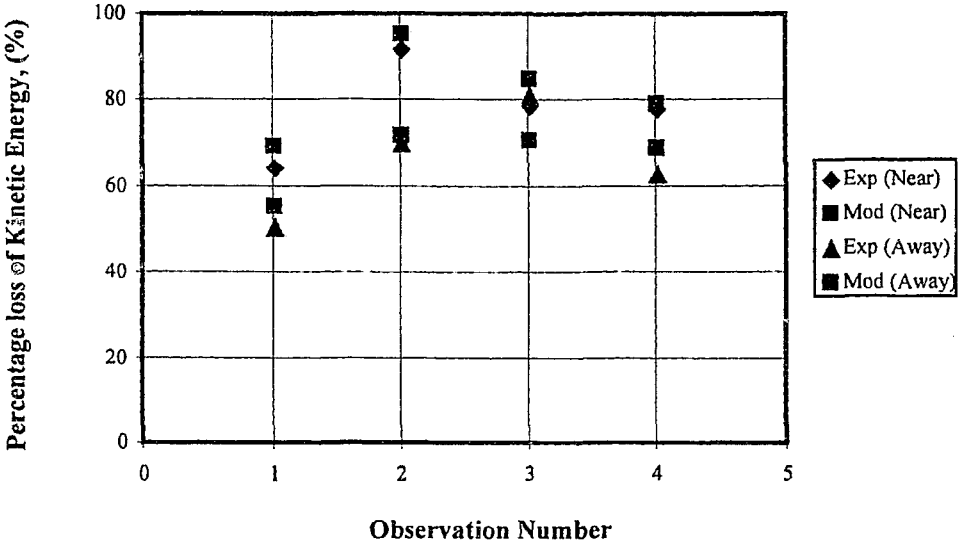

(b)

Fig. 4.33: Comparison of predicted rigid plastic model, (Mod) (■) and experimental, (Exp) (♦) Percentage Loss of Kinetic Energy KE_{loss}, for A=60° particles, for: (a) forward rotating particles for near and away from the transition condition and (b) backward rotating particles for near and away from the transition condition . Data is taken from Tables A.1, A.3, A.5

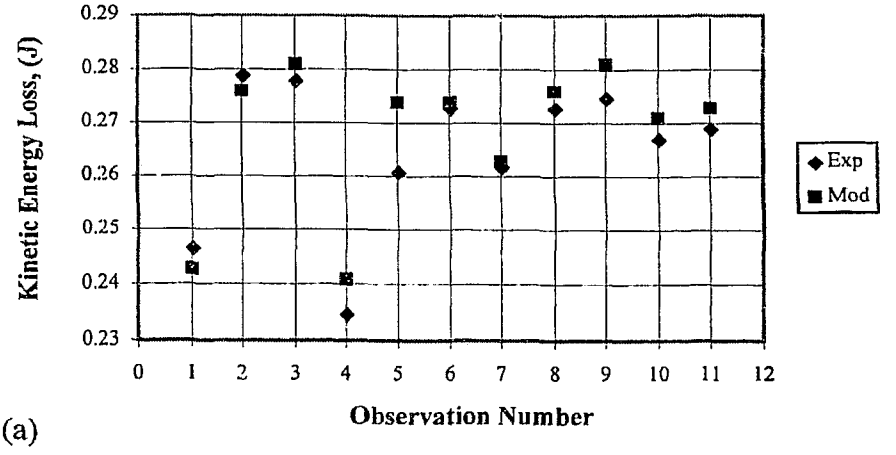

(a)

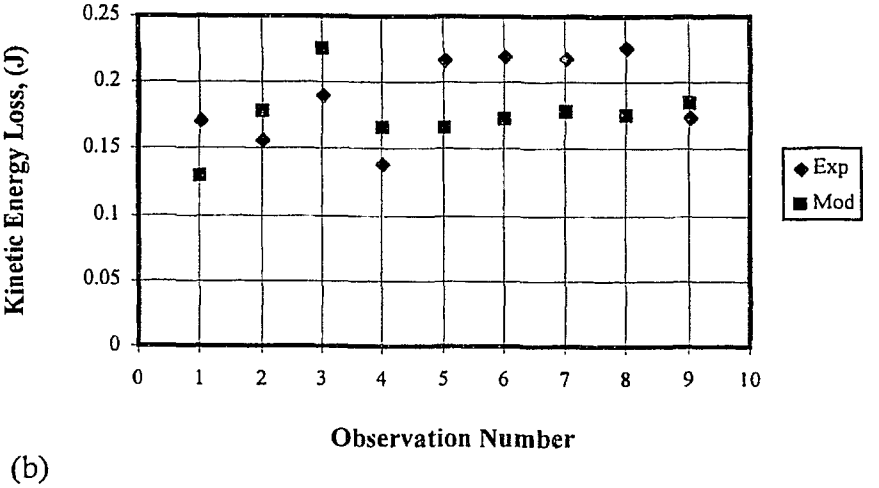

(b)

Fig.4.34: Comparison of predicted rigid plastic model, (Mod) (■) and experimental, (Exp) (♦) Kinetic Energy Loss KE_{loss}, for A=45° particles, for: (a) forward rotating particles, and (b) backward rotating particles. Data is taken from Tables A.13 and A.15.

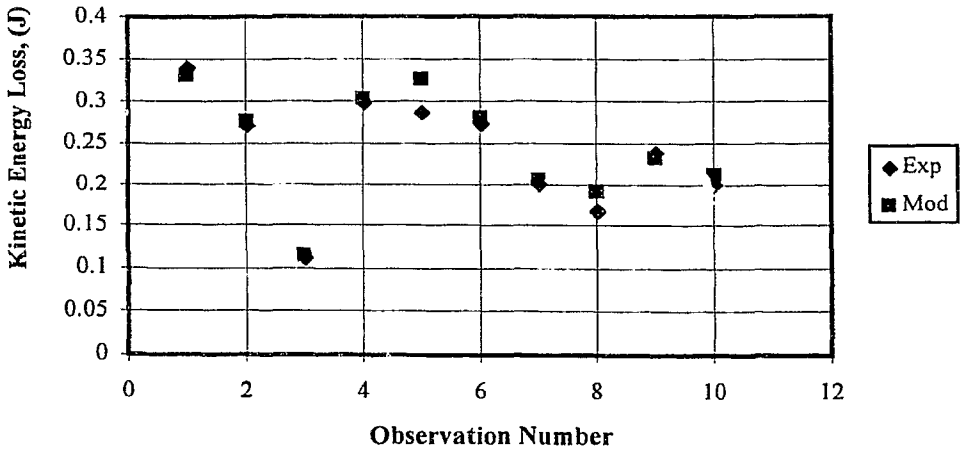

Fig. 4.35: Comparison of predicted rigid plastic model, (Mod) (■) and experimental, (Exp) (♦) Kinetic Energy Loss KE_{loss}, for forward rotating particles for A=80°. Data is taken from Table A.19.

4.5.4 Particle Kinematics at the Transitions from Forwards to Backwards Rotation

To study the eroding particle kinematics in terms of various rebound parameters, the characteristic curves (Figs. 4.36–4.44) were plotted from the data presented in Tables A.7, A.9, A.11 and A.17 for A=60° and A=45° particles. For a given incident angle of attack, incident velocity, and particle angularity, a critical initial orientation angle θ_i^{crit}, exists at which the transition between forward and backward rotation occurs [2, 3]. Near this transition, rebound parameters were found to be extremely sensitive to input conditions. The experimental data of Tables A.1 and A.3 occur relatively far away from this transition orientation angle, while Table A.5 presents data near such critical orientation angles (θ_i^{crit}).

For the entire characteristic curves which involves A=60° and A=30° particles undergoing transition from forward to backward rotation, the behavior of various rebound parameters (i.e. rebound linear velocity, rebound angular velocity, kinetic energy loss) changed at the same critical orientation angle, θ_i^{crit}, for the corresponding identical conditions of impact. The critical orientation angle θ_i^{crit}, was found to be in the range of 43° - 47° for A=60° and 34° for A=45° respectively.

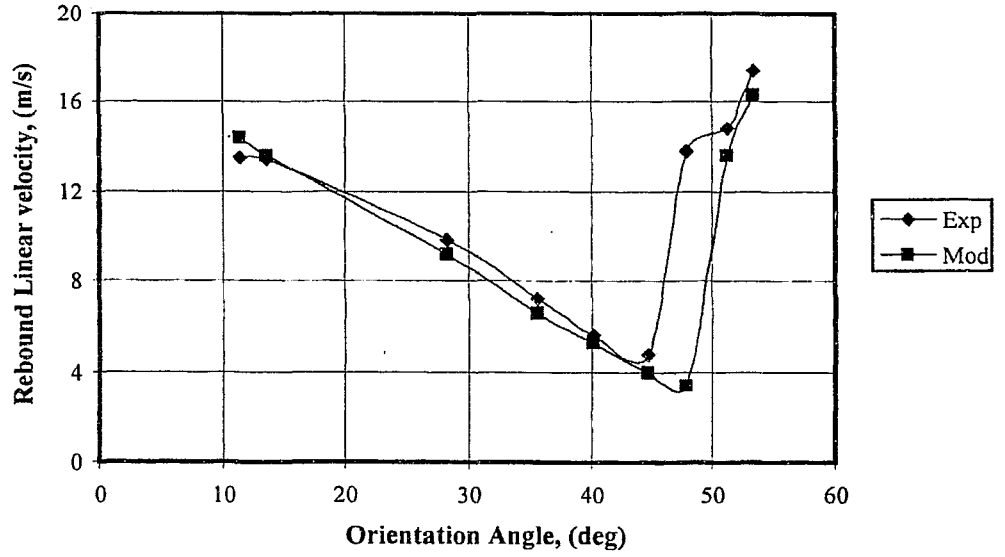

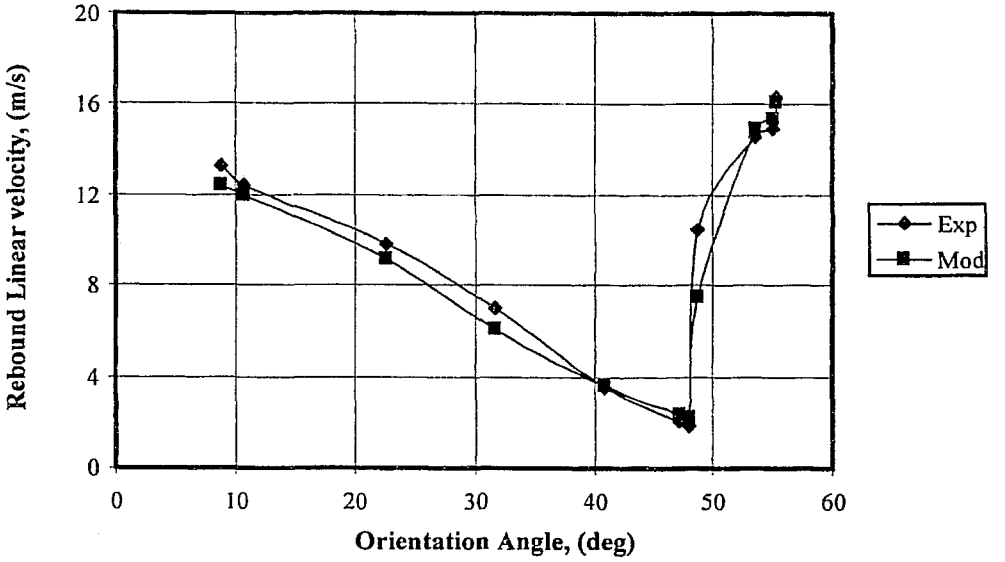

(b)

Fig 4.36: Predicted rigid plastic model (Mod) (■) and experimental (Exp) (♦) rebound linear velocity vs orientation angle for A=60° and V_i=25m/s for: (a) α=33.8° and (b) α=40.8° Data is taken from Tables A.7 and A.9.

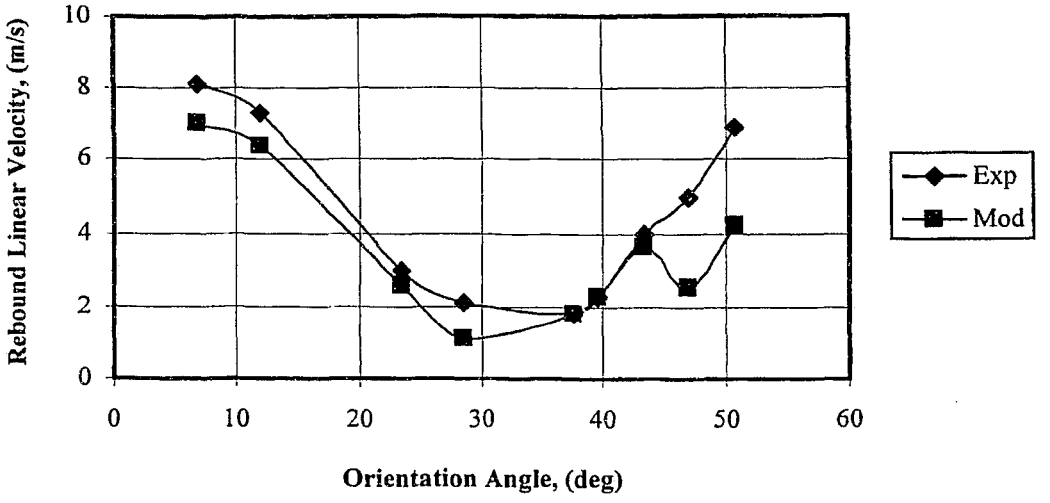

Fig. 4.37: Predicted rigid plastic model (Mod) (■) and experimental (Exp) (♦) rebound linear velocity, V_{reb} vs orientation angle for α=60°, A=60°, and V_i=25m/s. Data is taken from Table A.11.

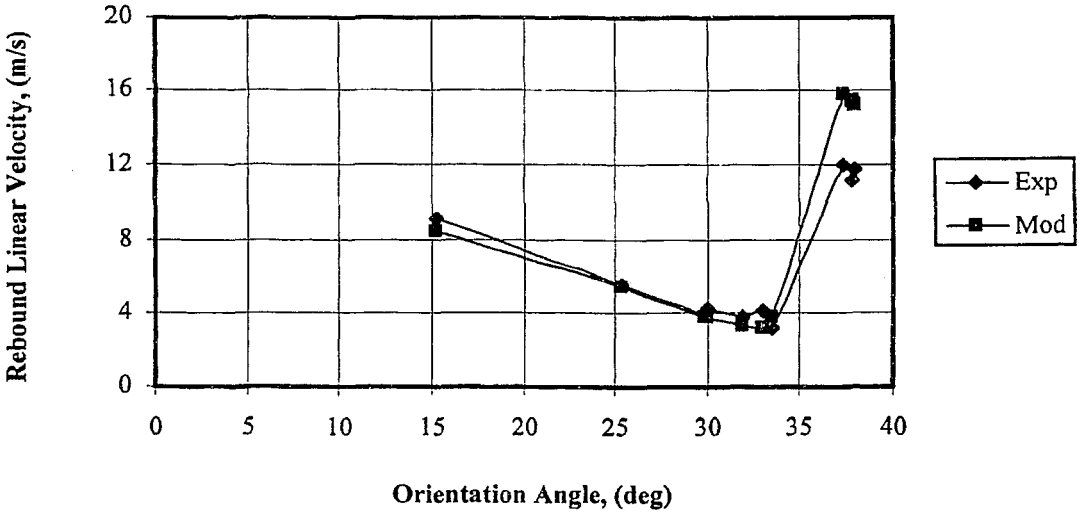

Fig. 4.38: Predicted rigid plastic model (Mod) (■) and experimental (Exp) (♦) rebound linear velocity, vs orientation angle for α=47.5°, A=45° and V_i=25m/s. Data is taken from Table A.17.

(a)

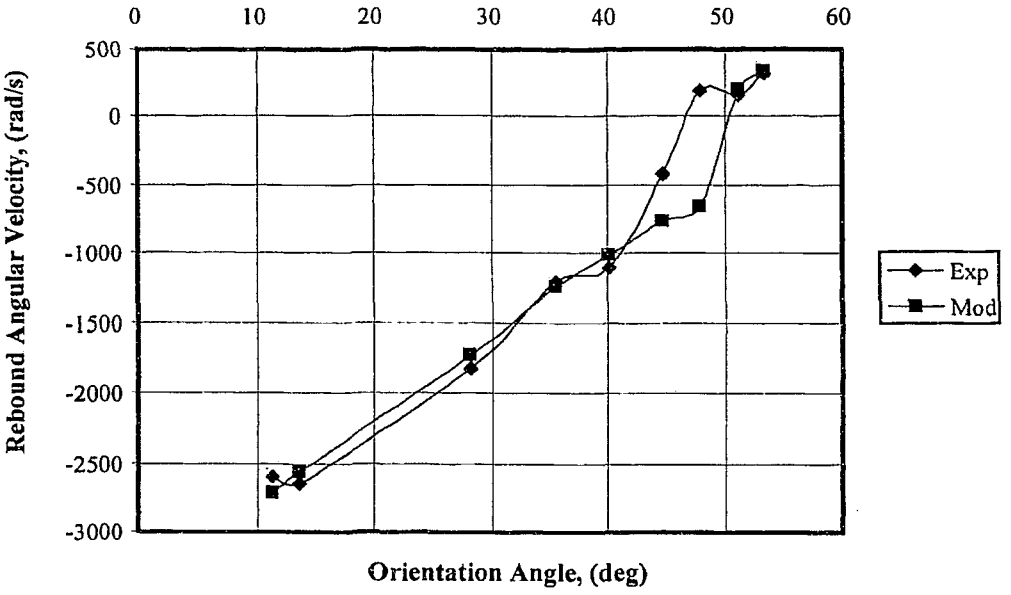

(b)

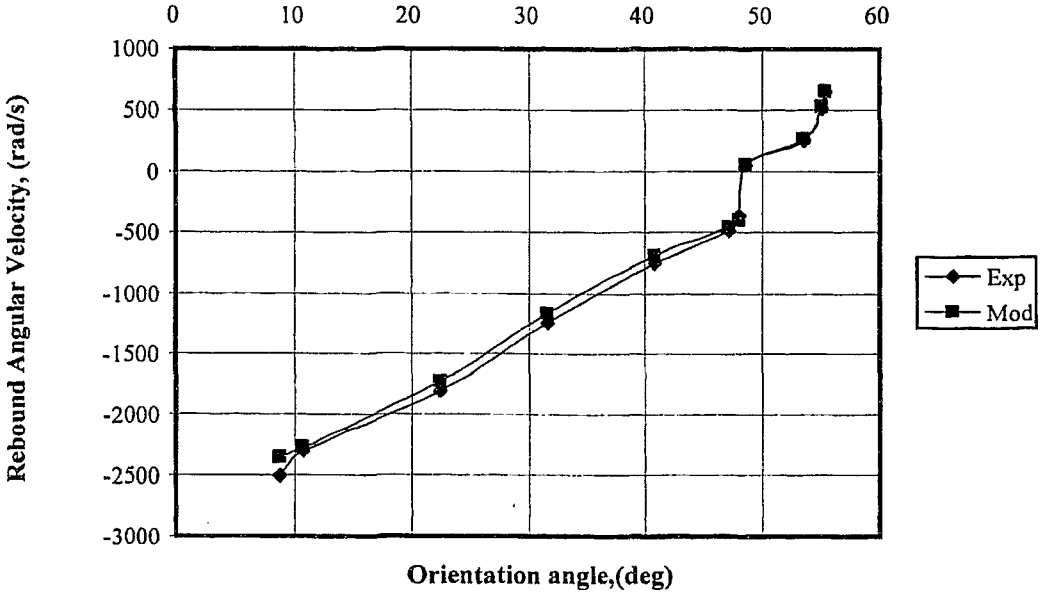

Fig 4.39: Predicted rigid plastic model (Mod) (■) and experimental (Exp) (♦) rebound angular velocity vs orientation angle for A=60°, V_i=25m/s for (a) α=33.8° and (b) α=40.8°. The rotation of the rebounding particle is reversed at the transition. Data is taken from Tables A.7 and A.9.

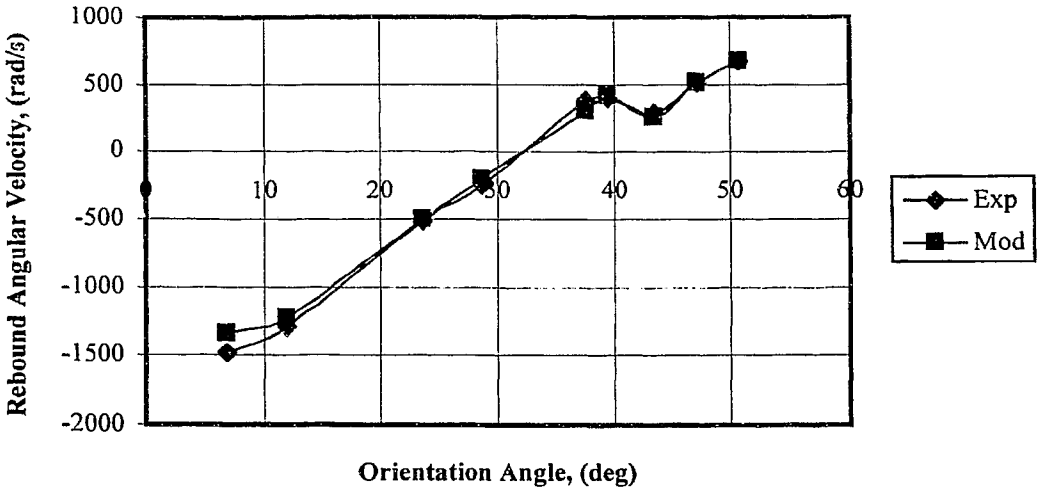

Fig. 4.40: Predicted rigid plastic model (Mod) (■) and experimental (Exp) (♦) rebound angular velocity vs orientation angle for: for α=60°, A=60°, and V_i=25m/s. Data is taken from Table A.11.

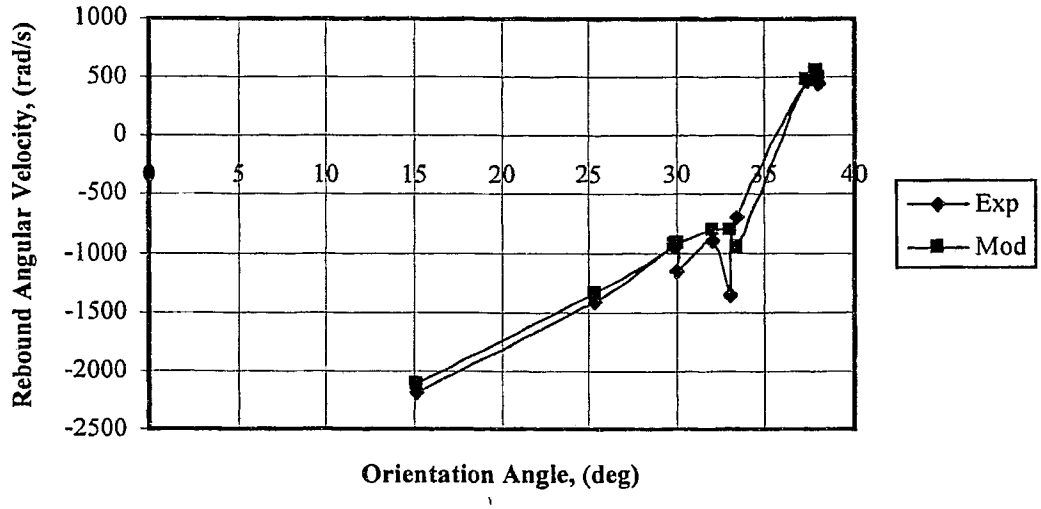

Fig. 4.41: Predicted rigid plastic model (Mod) (■) and experimental (Exp) (♦) rebound angular velocity vs orientation angle for: A=45° and V_i=25m/s. Data is taken from Table A.17.

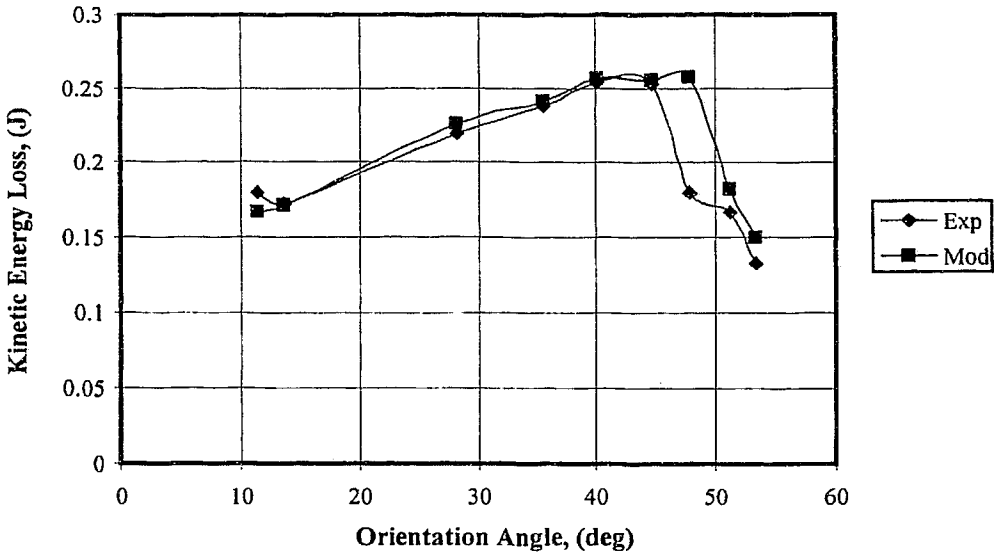

(a)

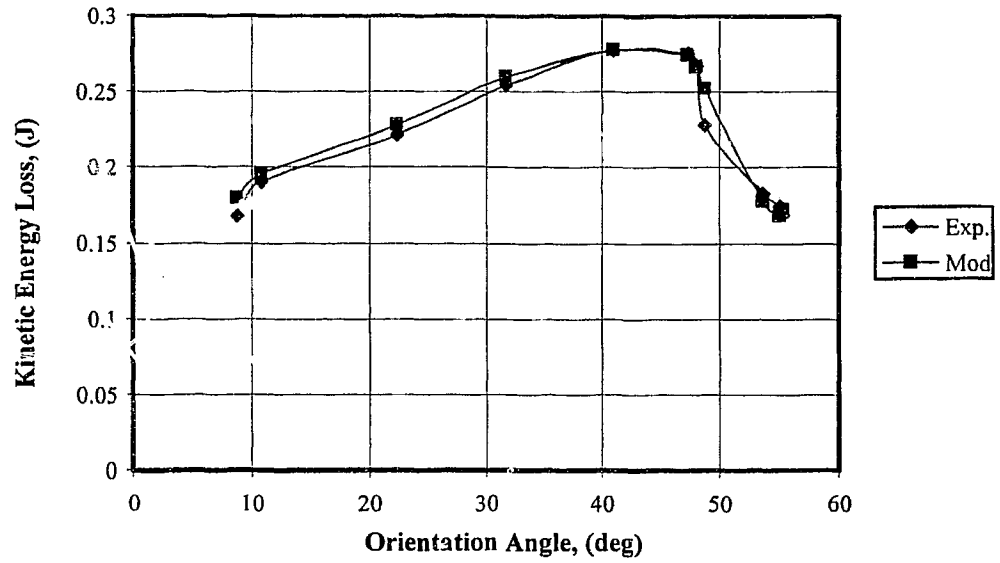

(b)

Fig 4.42: Predicted rigid plastic model (Mod) (■) and experimental (Exp) (♦) kinetic energy loss, vs orientation angle for V_i=25m/s, A=60° for: (a) α=33.8° and (b) α=40.8°. The maximum energy loss occurs at the transition. Data is taken from Tables A.7 and A.9.

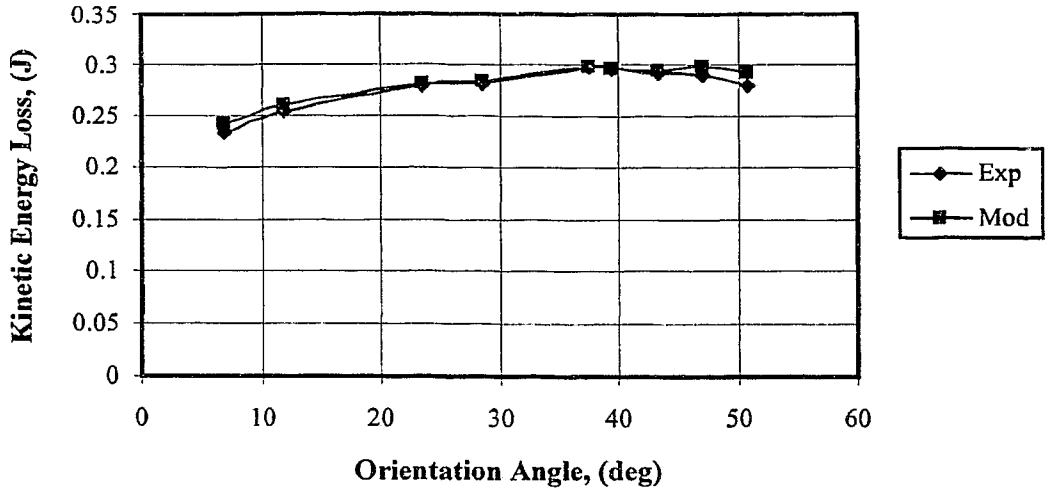

Fig. 4.43: Predicted rigid plastic model (Mod) (■) and experimental (Exp) (♦) kinetic energy loss, vs orientation angle for V_i=25m/s and A=60° Data is taken from Tables A.11.

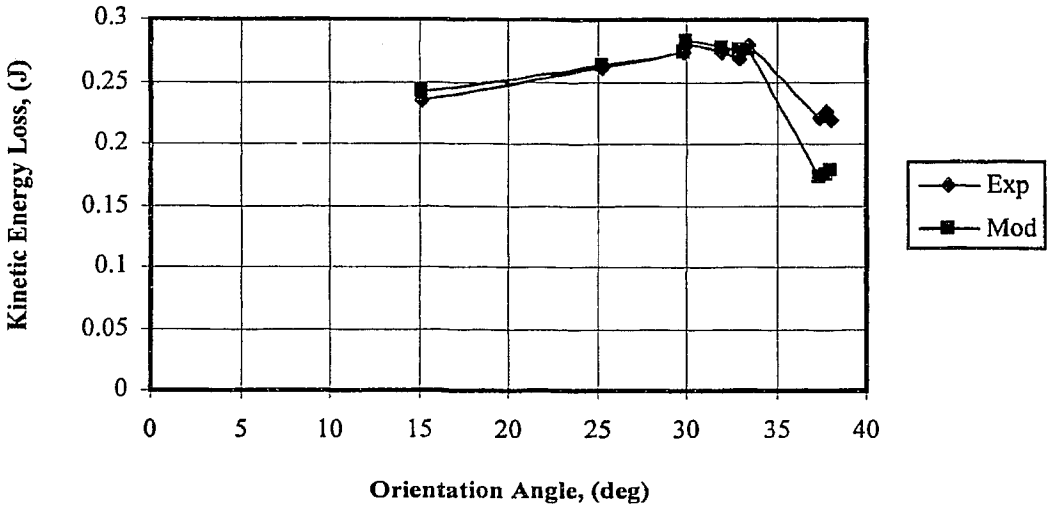

Fig. 4.44: Predicted rigid plastic model (Mod) (■) and experimental (Exp) (♦) kinetic energy loss, vs orientation angle for V_i=25m/s and A=45°. Data is taken from Table A.17.

It is worth noting that the initial rotational velocity did not appear to significantly affect θ_i^{crit}, over the range considered in Tables A.7, A.9, A.11, and A.17, lending credibility to the parametric studies in ref. [3], which neglected its effect. The agreement between experimental and simulated results was very good and in all cases, the model predicted the correct type of impact (i.e. forward or backward).

The behavior of these characteristic curves given in Figs. 4.36 to 4.44 were utilized to support the explanation given for greatest crater volumes occurring at the transition, described in detail in Section 4.6.1.

4.6 Crater Volume: Comparisons between Predicted and Experimental Results

Figs. 4.45 and 4.46 show the comparison of the crater volumes for the model prediction and experimental results for A=80° and A=30° particles for the data taken from Table A.19 and Table A.21 respectively. For both the experimental and the model prediction cases, the particles involving forward rotations, consistencies in overestimation of crater volume by the model predictions could be seen with an average error percentage within 25% (see Tables A.21 and A.23).

Figures 4.47.a and 4.47.b illustrate the typical nature of the crater profile for the experimental and the model predictions in the cases of forward and backward impacts respectively. A good agreement was found in the general shape of the crater profiles except at the crater edges, where the presence of pile up material was found for experimental results. Furthermore, the relative degrees of indentation are lower in the case of experimental results, for both forward and backward rotations. The reason could be the difference in relative energy consumption for plastic deformation, as explained in Section 4.5.1.

The crater length (Fig.4.47b) resulting the experimental case was found to be shorter than the model predicted length. In the majority of the backward rotations, the mechanism of "chip break-off" earlier than when the leading vertex is above the target surface could be experimentally observed, resulting in shorter crater lengths, whereas the model predicted a complete cutting action of the leading edge.

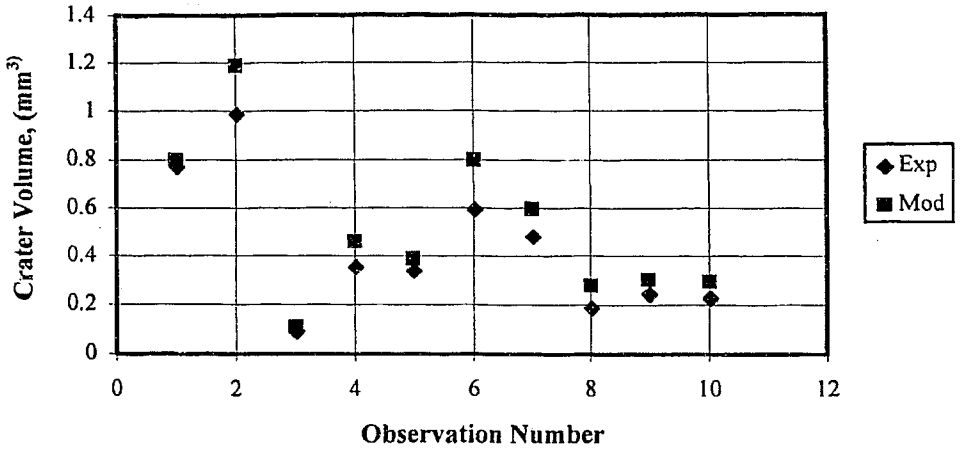

Fig. 4.45: Comparison of predicted rigid plastic model, (Mod) (■) and experimental, (Exp) (♦) crater volume, for forward rotating particles at A=80°.Data is taken from Table A.19.

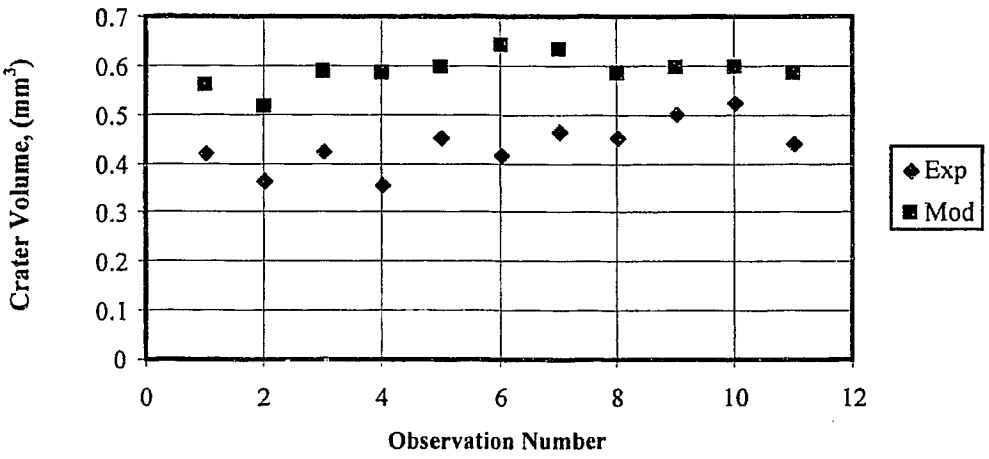

Fig. 4.46: Comparison of predicted rigid plastic model, (Mod) (■) and experimental, (Exp) (♦) crater volume, for forward rotating particles at A=30°.Data is taken from Table A.21.

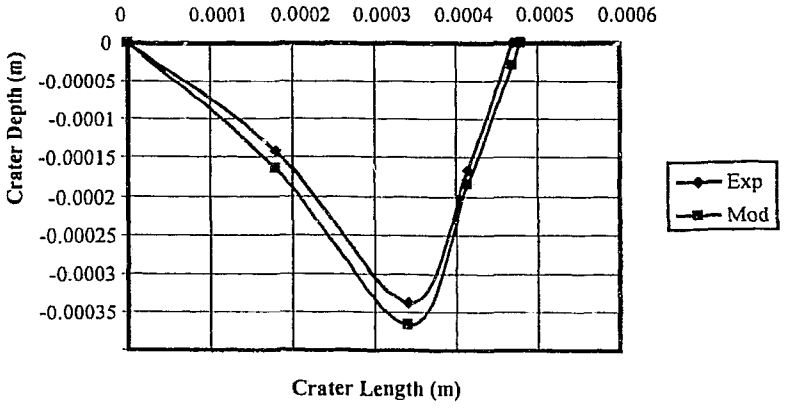

(a)

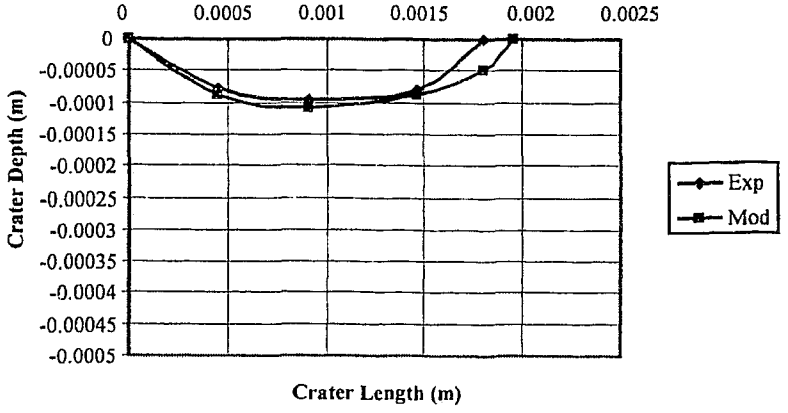

(b)

Fig.4.47: Comparison of experimental, (Exp) and predicted rigid plastic model (Mod) crater profiles. (a) Forward rotation with α =33.7°, θ_i=11.4 °, V_i=25 m/s, $\dot{\theta}_i$ 150 rad/s (b) Backward rotation with α =32°, θ_i=51 °, V_i=25 m/s, $\dot{\theta}_i$ = 209 rad/s.

4.6.1 Crater Volume at Transitions from Forwards to Backwards Rotation

The characteristic curves of Figs. 4.48- 4.51 were plotted to study the effect of orientation angle, θ_i, on the crater volume. To facilitate presentation of the data, the dimensionless parameters π_1 and π_2 from Ref. [3] were introduced. π_1, (eq. 4.7), represents the ratio of the plastic work required to create a crater having the size of the incident particle to the incident kinetic energy of the particle, whereas, π_2 (eq. 4.8) is defined as the ratio of the crater volume to the particle volume (both per unit thickness).

The introduction of the dimensionless parameters, π_1 and π_2, reduced the variable parameters to π_1, α, θ, μ, and A, and the only output parameter was π_2.

$$\pi_1 = \frac{P_d}{\rho V_i^2} \tag{4.7}$$

$$\pi_2 = \frac{A_{cr}}{2h^2 \cos A \sin A} \tag{4.8}$$

The mechanical uncertainty in shooting the particle from the catapult led to the incident velocities varying slightly for each of the impact cases. However, this small change in incident velocity did not significantly affect the particle kinematics and crater volume, hence an average value of incident velocity, V_i =25 m/s was used in calculating the dimensionless parameter, π_1. Substituting the values of dynamic hardness, P_d = 440 MPa, density of particle, ρ = 8028.5 kg/m^3 and average incident velocity, V_i=25 m/s, the dimensionless parameter was calculated to be π_1 =87.68.

Fig. 4.48, Fig. 4.49 and Fig. 4.50 demonstrate the experimental and model predictions of the variation of dimensionless crater volume, π_2, with the orientation angle, θ_i, for an angular particle (A=60°) at three different angles of attack, α=33.8°, 40°, 60°, for constant values of π_1 =87.68 and friction coefficient, μ=0.3. To construct this curve, the model was run for different orientation angle, θ_i, at a constant angle of attack, α, to obtain predicted π_2 values, which where then compared to the corresponding experimental values. The general shape of the curves is maintained in all cases (Fig. 4.32-4.33a), and the peak value of π_2 occurs at almost the same value of θ_i^{crit}, regardless of the angle of attack, α, signifying the importance of orientation angle, θ_i, for material removal.

The maximum amount of material removal (i.e., the crater volume) occurred at the transition points. For all the cases of A=60° particle, the transitions from forward to backward rotation were near to θ_i=45°, where maximum values of π_2 is reported, irrespective of the angle of attack. A higher angle of attack, α, resulted in a larger crater over a wide range of incident orientation angles, θ_i (compare π_2 in Figs 4.48, 4.49 and

4.50). Thus, one would expect maximum material removal at normal incidence. This, however, is not the case. For ductile erosion processes, while the craters are biggest at normal incidence, in most cases, they do not actually result in material removal, but only plowing of the material to the crater edges in the form of lips. Actual material removal occurs when these lips are removed by subsequent impacts. The present model, in its current form, cannot account for these subsequent impacts.

It was also noticed that the behavior of various rebound parameters showed typical trends at the transition that resulted in the greatest crater volumes. This could be explained by considering each parameter individually as described in section 4.5.4 (Figs.4.36-4.44):

a) The magnitude of linear and angular velocities is least at the critical orientation angle θ_i^{crit} (Figs. 4.36-4.41). Thus, at the transition, the particle rotation through the impact is minimized, resulting in a significant amount of kinetic energy consumed in the formation of craters (Figs.4.42- 4.44), as discussed in Section 4.5.4.

b) Furthermore, Figs. 4.36- 4.38 show that a steep rise in the slope of the velocity curve immediately after the transition point results in a rapid decrease in kinetic energy consumed for plastic deformation, which, in turn, leads to a steep reduction in crater volume (Figs. 4.48-4.51).

c) Figs.4.42- 4.44 demonstrate that the kinetic energy loss is greater at the transition between forward and backward rotation as compared to conditions which are far from the transition zone for both the forward and backward rotation of the particle (see the KE_{loss} values away from θ_i^{crit}). Here, the maximum incident kinetic energy is consumed in plastic deformation of the target material leading to greater crater volumes. A similar behaviour was also noticed in section 4.5.3 (Fig. 4.33) for the data points near to the transition orientations as compared to ones away from the transition.

It is consistent that, in all the cases (Figs.4.48-4.51), the experimental π_2 values (i.e. the crater volume) were smaller than the model predicted ones. The reason is same as explained section 4.5.1; i.e. due to the presence of the spring-back effect in the target

material, which leads to higher rebound energy of the particle, resulting in less plastic deformation. It was also noticed that the average percentage difference error in experimental and predicted results for crater volumes decreased with the higher angle of attack (see Tables A.8, A.10, A.12, and A.18). Here, the perpendicular component of velocity vector V_z, of the incident kinetic energy required for plastic deformation is greater, resulting in deeper craters, with increase in area of the contact between the particle and the target. The particle has also less rebound energy and hence a reduced spring-back effect was noticed in the experimental results with higher angles of attack.

It is noteworthy that the maximum error of about 30-50% was reported while measuring the crater volumes at these transitions. This is due to the fact that the erosion process is extremely sensitive to the initial conditions of impact at the transition. The chip formation and break-off, and the resistance to particle motion by the piled up material at the crater edge may be the factors influencing the material removal at these transition orientations.

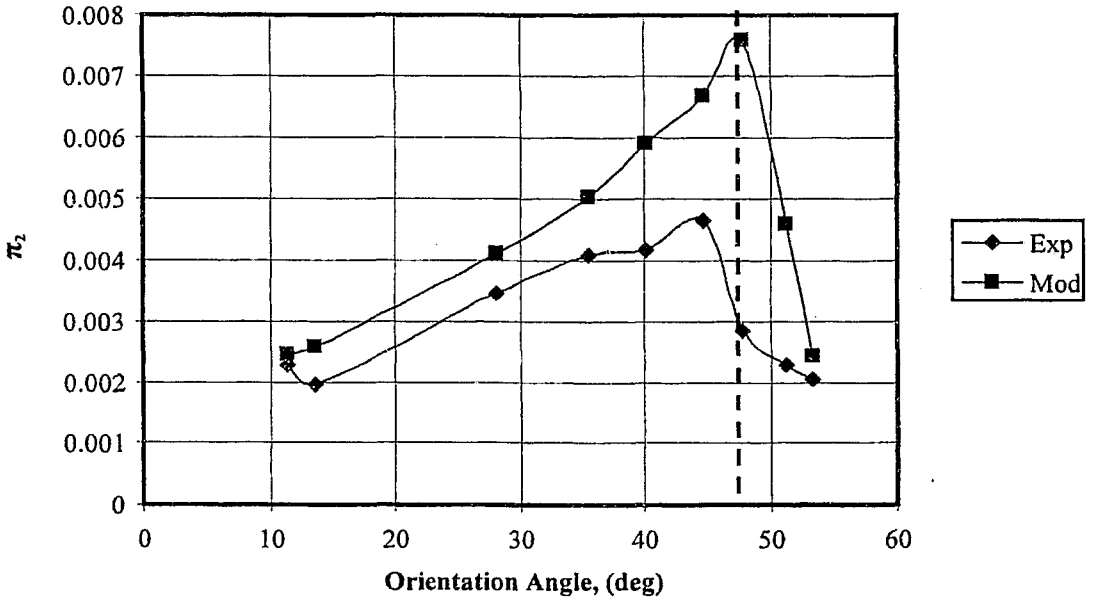

Fig. 4.48: Rigid plastic model predicted (Mod) and experimental (Exp) dimensionless crater volume (π_2) versus orientation angle for α=33.8°, V_i=25m/s, and A=60°. The left side of the dotted line indicates forward rotation and the right side indicates backward rotation of the rebounding particle. Data is taken from Table A.7.

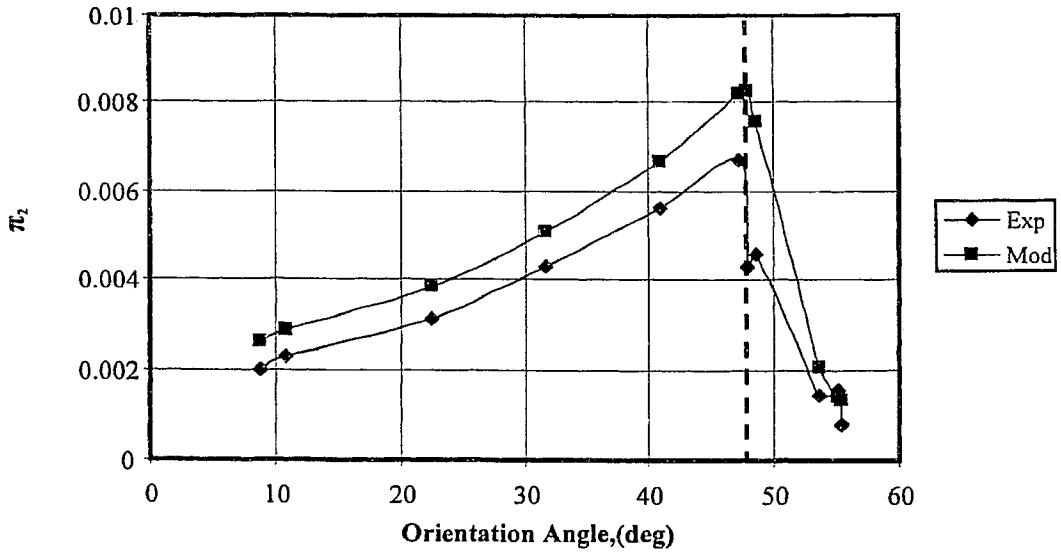

Fig 4.49: Rigid plastic model predicted and experimental dimensionless crater volume (π_2) versus orientation angle for α=40°, Vi=25m/s, and A=60°. The left side of the dotted line indicates forward rotation and the right side indicates backward rotation of the rebounding particle. Data is taken from Table A.9.

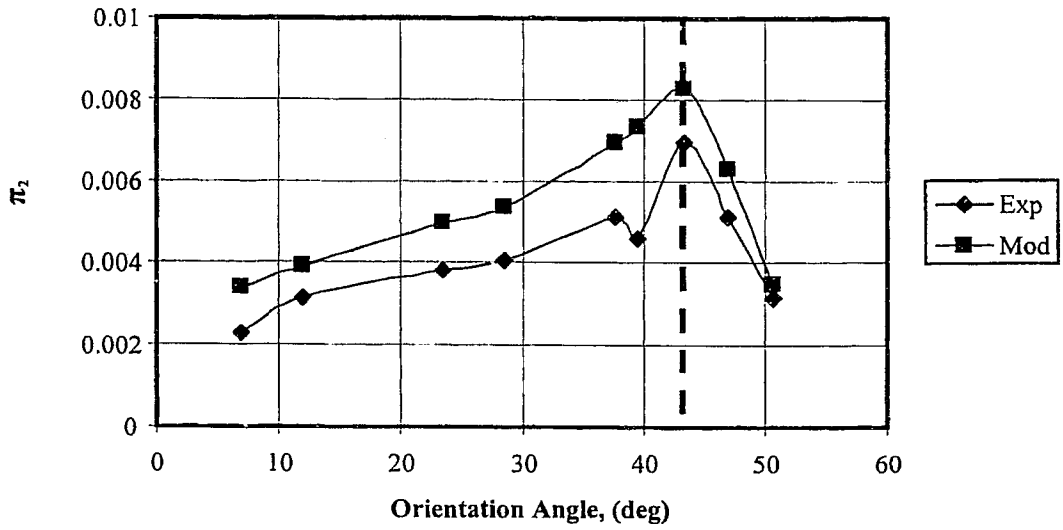

Fig 4.50: Rigid plastic model predicted and experimental dimensionless crater volume (π_2) versus orientation angle for α = 60 °, V_i=25m/s, A=60°. The left side of the dotted line indicates forward rotation and the right side indicates backward rotation of the rebounding particle. Data is taken from Table A.11.

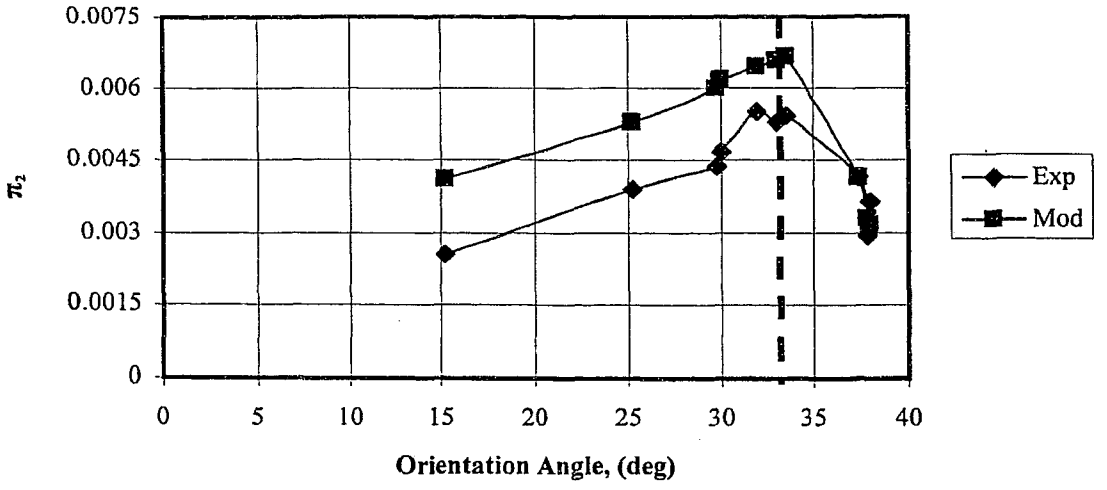

Fig. 4.51: Rigid plastic model predicted and experimental dimensionless crater volume (π_2) versus orientation angle for α=47.5°, A=45° and V_i=25m/s. The left side of the dotted line indicates forward rotation and the right side indicates backward rotation of the rebounding particle. Data is taken from Table A.17.

4.7 Summary:

In this chapter, generally two types of erosion mechanisms were identified, depending on whether the particle rotated forwards or backwards. The forward rotation of the particle plowed material into lips at the crater edge but no target material was actually removed. In the backward rotation, cutting or machining action was observed resulting in removal of chip from the target material.

To define the force resisting the indentation in the target material, a combination of dynamic hardness and coefficient of friction was used. This combination forms the single most important parameter in predicting rebound particle kinematics and removal of material.

The conditions of transition of particle rotation from forwards to backwards and maximum material loss has been described. Overall, it could be concluded that the rigid-plastic model predictions showed excellent agreement with experimental results in almost all the cases of particle kinematics and material loss (i.e. crater volumes).

Chapter-5

Finite Element Analysis of Angular Particle Impacts

In this chapter, a detailed finite element analysis of single angular particle impact is undertaken to study the impact behavior of the angular particles, compare the results with the experimental and rigid-plastic model predictions described in chapter 4, and to shed some light on the tunneling and chip break off phenomena postulated in Section 4.4.3.

5.1 Schematic Modeling of Impact

The schematic diagram of the single angular particle (A=60°) impacting the target material is shown in Fig.5.1. Here, in the 2-D schematic modeling, the plane of the particle and the target is described in the X-Y plane, unlike the Y-Z plane used in the rigid plastic model [2].

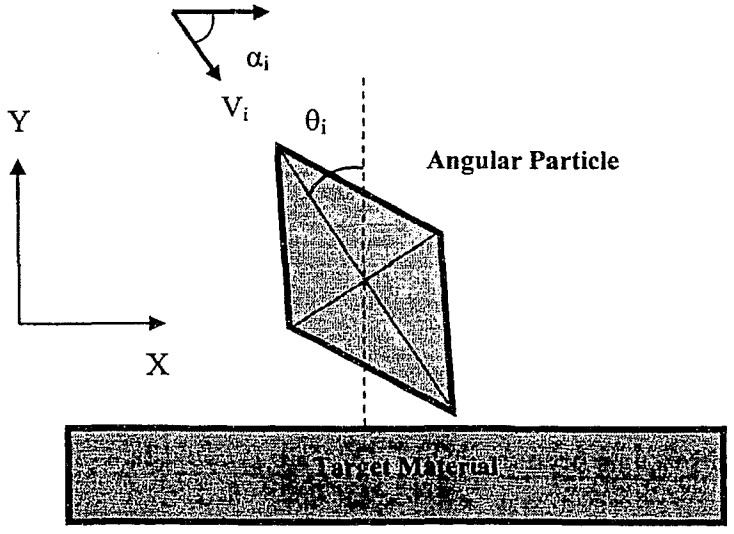

Fig. 5.1: Schematic diagram of single angular particle impact

In this manner, the angular particles (i.e. A=30°, 45°, 80°) could be well represented. The particle is assumed to strike the surface of the target material with its leading edge and rebound. The impact could be characterized by single impact or multiple impacts depending on the incident and the rebound conditions. The particle dimensions and shape were modeled using data presented in section 3.2, chapter 3. A typical mesh used in ANSYS 8.0, is illustrated in Fig. 5.2.

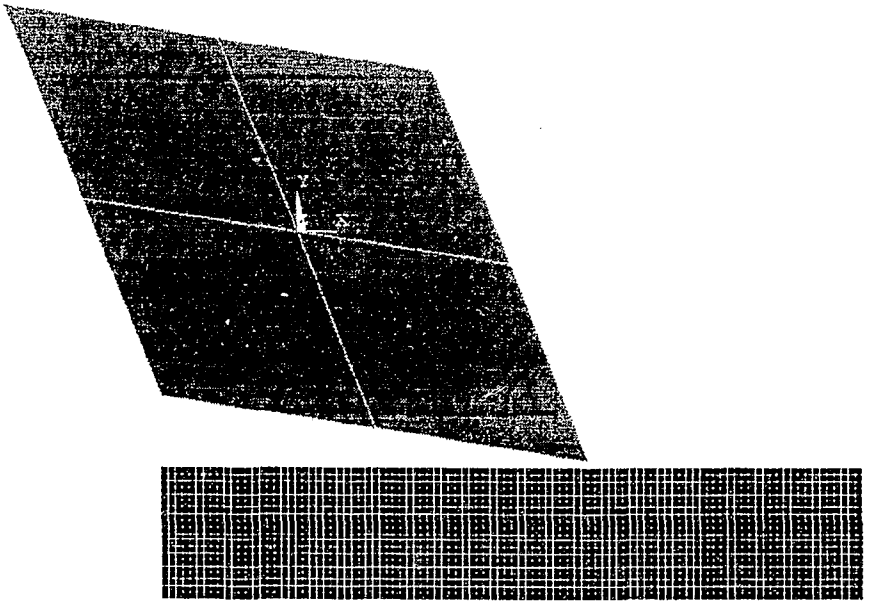

Fig. 5.2: Mesh of single angular particle impacting a target material used in finite element modeling of erosion A=60°

5.2 Finite Element Modeling of Impact

The finite element analysis was accomplished in ANSYS University Research/Ls-Dyna (ANSYS Release 8.0) (Ansys Inc, Canonsburg, USA) in three different stages, as shown in Fig. 5.3, (i) Preprocessing, (ii) Solution (iii) Post Processing.

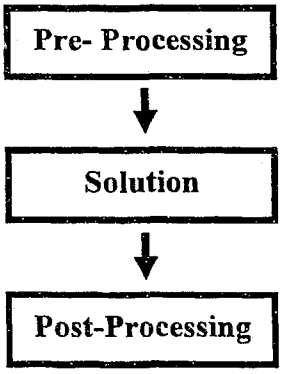

Fig. 5.3: Different steps involved in Finite element Analysis of Single angular particle Impact

5.2.1 Preprocessing Stage

5.2.1.1 Modeling/Meshing/Element Type

This stage involved in defining the element type, material properties and geometric modeling of the angular particle and the target material. The particle and the target are modeled as a 2-D solid in ANSYS-LS-DYNA and the erosion is analyzed per unit thickness of both, the particle and the target. The geometric modeling of angular particle depends on its orientation to the target material, therefore coordinates of the particle vertices were obtained by substituting the particle angularity A, orientation angle θ, and side length h, in the inertial coordinate equation (eq.2.7 section 2.3.1.4, chapter 2). The target was modeled as a rectangle having thickness 3 mm. and varying length.

As this was an explicit dynamic analysis, the element used in defining the particle and the target is a PLANE 162 element. The element used is planer, defined by four nodes, each having six degrees of freedom: translation, velocity, and acceleration in the nodal x and y directions.

After defining the element type, the geometric model of particle and the target were mapped meshed. In the present study, the target material was of prime concern, hence the number of elements used for modeling it varied between 5000-20000 depending on the coarseness or fineness of the mesh. For the particle, the number of

elements was four. In reality, because the particle was treated as rigid (i.e. non-deforming), only one element was required, but four was chosen because it results in a node at the center of the particle, thus facilitating calculations of center of mass rebound velocity.

5.2.1.2 Material Properties

The "rigid –material" model is used for defining the material properties of the angular particle. The input data required for the model are shown in Table 5.1:

Material Properties of Particle	
Density of the mass (DENS)	8025.5 kg/m^3
Modulus of Elasticity (EX)	203 GPa
Poisson's ratio	0.3

Table: 5.1. The material properties of particle. From Ref. [28]

The two constraints parameters defined in this model are: (1) Translational constraint Parameter- Z-displacement (2) Rotational Constraint Parameter- X and Y rotate. Thus the particle was constrained from moving out of the X-Y plane.

"Elastic-Plastic Hydrodynamic model" is used for modeling the target material which undergoes large amounts of strain. The stress-strain behavior can be defined by the data points along the effective true stress vs. true plastic strain curve as shown in Fig. 5.4. The input parameters for the finite element model are: density (DENS), elastic modulus (EX), shear modulus (GXY). The other input parameters that are determined from the perfectly plastic stress- strain curve (Fig. 5.4) for the target material are: σ_0 (initial yield stress), ε_f (failure strain), ε_1-ε_{16} (effective strain data curve values, σ_1-σ_{16} (effective stress data curve values), and C_0-C_6 (linear polynomial equation of state constant). Table 5.2 illustrates the material properties of the target.

Single surface 2D eroding contact was defined between the particle and the target surface. This formulation allows for elements to be removed from the mesh, during the

solution, if the strain in given element reached the prescribed failure strain. Friction can also be modeled, and thus the dynamic coefficient of friction, μ, described in chapter-4 (section 4.3), was employed, depending on the angularity A, of the particle.

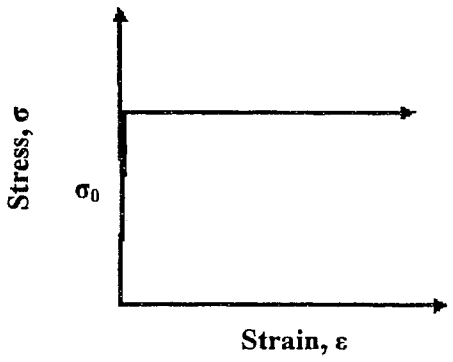

Fig. 5.4: Stress-Strain Curve of perfectly plastic target material.σ_0 represents constant yield stress

Material Properties of Target	
Density (DENS),	2730 kg/m^3
Elastic modulus (EX),	68.9 GPa
Shear modulus (GXY).	25 GPa
σ_0 (initial yield stress)	440 MPa
ε_f (failure strain)	0.3-0.9
ε_1 (effective strain data curve values)	0
ε_2 (effective strain data curve values)	10
σ_1-σ_{16} (effective stress data curve values)	440MPa
C_1 (linear polynomial equation of state constant)	0
C_2 (linear polynomial equation of state constant)	70 GPa
C_3C_6 (linear polynomial equation of state constant)	0

Table: 5.2. Material properties used in elastic- plastic hydrodynamic model to define the target material. From Ref. [28]

5.2.2 Solution Stage

The incident impact parameters are defined in this stage, which include: linear velocity V, resolved in V_x and V_y directions depending on the angle of attack, α, and the angular velocity $\dot{\theta}_i$. The target is constrained at all degrees of freedom, so that it is static with respect to the impacting particle. For the target, the number of elements was varied in the range of 5000-25000 depending on coarse or fine mesh. Finally, the finite element model was solved in time steps of 0.9 μs, with elements numbered in range of 15000-18000, obtain convergence of the solution.

5.2.3 Post-Processing stage

The post processing stage consisted of calculation of the simulated results of the impact. In the present analysis, the parameters undertaken for studies are rebound velocity V_{reb}, and crater dimensions i.e. length and depth of the indentation.

5.3 Initialization of Failure Strain, ε_f

In modeling impacts involving high velocities, investigators [30-32] in the past have studied the variation of failure strain ε_f, of the eroding material with the incident velocity of impacting particles. It was observed that high strain rates influences the failure strain in ductile deformations. Hutchings [1, 9] reported strain rates of about 10^5 to 10^7 /s directly below where the particle impacted the surface. Similarly, high strain rates were also noticed by Sundararajan [18] in his models of plastic deformation zones. Hamouda and Hashmi [30] plotted stress-strain curves for pure Aluminium at high strain rates and demonstrated the difference in flow stress in quasi-static and impact loading conditions. They noticed the presence of higher flow stresses in the range of 400 MPa at high strain rates of 10^5/s corresponding to strain conditions of 0.2 to 1.6. Rupture strains of 70–160% have been found for commercially pure Aluminium [30]. It was reported that, for a fixed wall thickness, the rupture strain increases with the strain rate. Under high strain rate, exceeding 10^5 /s, Aluminium and copper metal cylinders have been found to rupture at 70–160%, and in some cases even up to 300% strain. A detailed finite

element study for the failure strain criterion on alloys of Aluminium was conducted by Rade Vignjevic and co-workers [31]. They reported failure strains in range of 1.00 to 1.25 under the influence of high impact velocities.

Because the strain rates in the presently considered angular particle impacts depended on the number of parameters including particle angularity, and the particular tumbling dynamics of the particle, the failure strain could not be considered constant. At a constant yield stress (i.e. σ_0-σ_{16} = 440 MPa) (see Fig. 5.4), the failure strain ε_f, for the target material was found to vary between 0.3 to 0.9, depending on the particle angularity A, the angle of attack α, and relative velocity vector of the particle edge indenting the target material. This constant yield stress value, (i.e.σ_0-σ_{16} = 440 MPa), corresponds to the dynamic hardness Pd, of the target material defined in section 4.3 (see chapter-4).

Finite element analyses were conducted for a two-dimensional diamond shaped particle (i.e. A=30°, 45°, 60°, 80°), at normal incidence (α=90°) and θ=0°, with no initial rotational velocity, at incident impact conditions identical to the ones used to determine the dynamic hardness in section 4.3 (chapter-4. The dimension of the craters (i.e. crater length and depth) obtained from the finite element model results (see Fig. 5.5) were compared with the experimental and rigid-plastic model results. Good agreement was observed between these results as seen in Table 5.3.

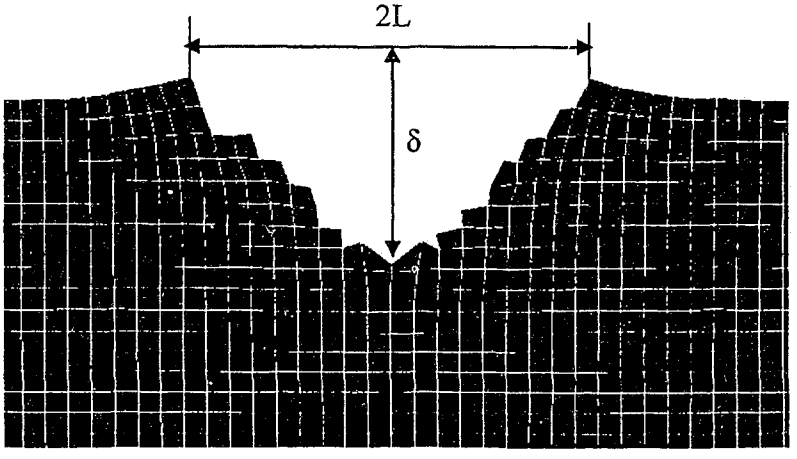

Fig. 5.5: Mesh of a simulated crater formed by A=45° particle impacting at α=90°, θ=0°, V=25m/s and $\dot{\theta}_i$ =0, where 2L and δ represents crater length and depth respectively

It is noted that, at normal angle of attack (i.e. α =90°), the failure strain increased with decrease in particle angularity. Ls-Dyna unfortunately only allows for a single value of failure strain to be prescribed, while different portions of the target would be subjected to different strain rates, so the chosen strains should be regarded as average values for the whole impact. While a highly angular particle would be expected to travel more rapidly during the impact and the material directly below the impacting particle would thus be subjected to a higher strain rate, the material adjacent to the sides of the particle would be subjected to a lower strain rate, as compared to a blunter particle. Apparently the strain rate seen by the sides is more important, overall.

A	Failure Strain ε_f	Experimental		Predicted		FEA	
		δ (mm)	2L (mm)	δ (mm)	2L (mm)	δ (mm)	2L (mm)
30	0.85-0.9	0.2986	1.0340	0.3000	1.0480	0.3050	1.0790
45	0.8-0.85	0.3760	0.7530	0.3860	0.7737	0.3570	0.7692
60	0.8-0.65	0.4685	0.5409	0.4737	0.5472	0.4601	0.5824
80	0.3-0.4	0.7500	0.2640	0.7603	0.2680	0.7480	0.4180

Table 5.3: Comparison of crater dimensions for impact at α=90°. The incident impact conditions are similar to the ones used in measuring dynamic hardness Pd.

5.4 Finite Element Simulation of Forward and Backward Impacts

In the FE studies, similar erosion mechanisms (i.e involving forward and backward rotations) to those reported in chapter-4 occurred. Fig. 5.6 shows finite element simulation of particles involving forward rotation, resulting in deep triangular shaped craters. The target material is ploughed into a lip at the edge of the crater, as seen in Fig. 5.6 (a) and Fig. 5.6 (b). In erosion applications in which particle streams are used, this piled up material is prone to removal by a next incoming particle, as discussed in section 4.1(chapter 4).

In the simulation of impacts involving backward rotations (Fig. 5.7), machining

and/or cutting of the target material, leading to formation of a long and shallow crater, was observed. The material loss occurs in form machined metal chips, ejected from the target material (Fig. 5.7 (b)). As reported in Section 4.1.2, the backward rotations involved multiple impacts, where the primary impact was followed by a secondary one. Fig. 5.7 (a) and Fig. 5.7 (b) demonstrate the sequence of primary and secondary impacts, where the first impacts is a pure machining action by the leading 60° vertex as the particle rotates backwards, followed almost immediately by a secondary impact (backwards rotating) by the adjacent 120° vertex. The bulk material loss occurs at the primary impact, leading to formation of larger craters in both length and depth, than the secondary impact.

Also from the Section 4.1.2, it was noted that, for backwards rotation of highly angular particles, the particle appeared to tunnel under the target, and it was postulated that, the machined chip would, in some cases, break off prior to completion of the cutting action. This theory of appears to be well supported by similar observations demonstrated in Fig. 5.8, which shows the particle with high angularity (i.e. A>45°) tending to "tunnel" below the surface, when launched at shallow incidence (Fig. 5.8 (a)). It can be seen that both the leading edges of the impacting particle vertex are below the undisturbed surface. Tunneling action is predominant in cases of high angularity particles such as A=80°, which has a capability to indent deep into the target (Fig. 5.9). At some subsequent time step during the impact, the particle rotates further and tends to "pry off" a chip of material, leading to break-off from the target (Fig. 5.8 (b)). Thus the collision kinematics is very sensitive at this point of chip break–off, which significantly affects the prediction of the orientation angle θ_{adj} for the onset of secondary impact (see Table A.23 and A.30 in appendix). The solution to this problem for use of the rigid plastic model discussed in Section 4.4.3; i.e. adjusting the initial orientation angle (θ_{adj}) for the secondary impact, is well supported by the finite element analysis results demonstrated in Fig. 5.7(b). This figure show a larger orientation angle (θ_{adj} >-30°), than would have been predicted by assuming the chip stayed attached for the duration of the impact.

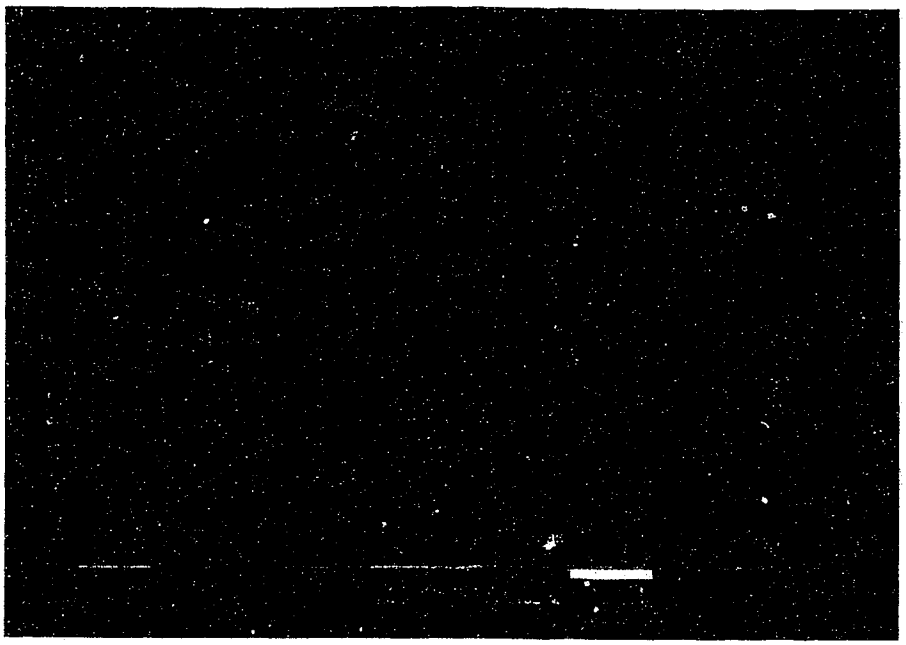

(a)

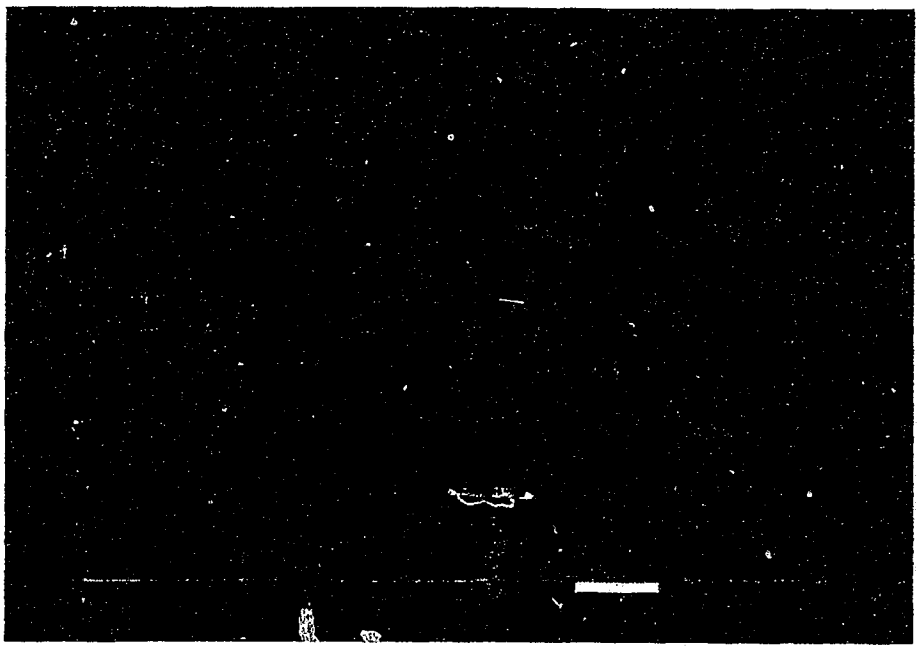

(b)

Fig. 5.6: Finite element simulation of forward rotating particles for: (a) A=45° particle and (b) A=30° particle. Note the material pileup at the crater

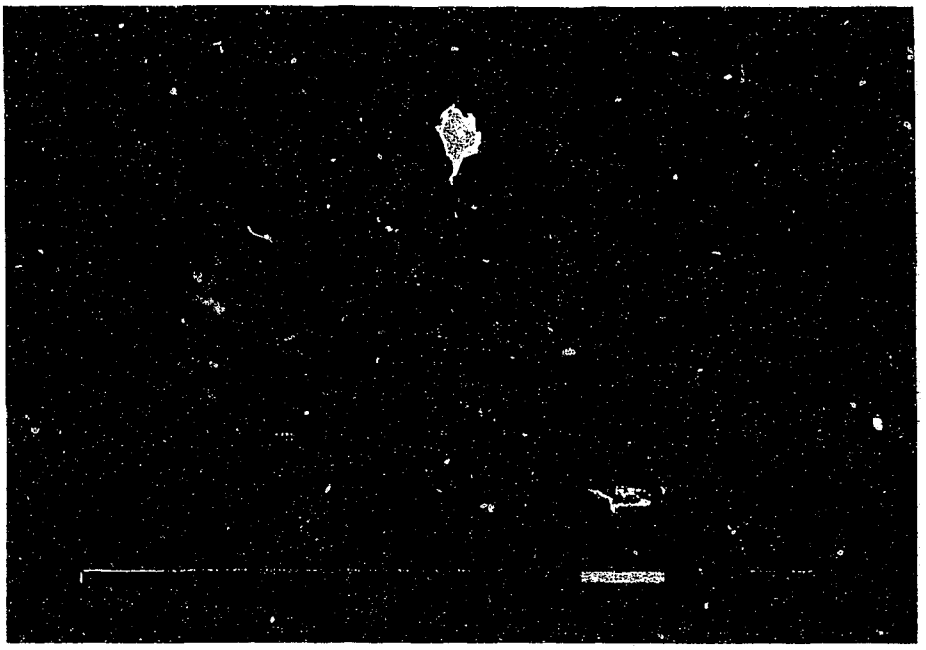

(a)

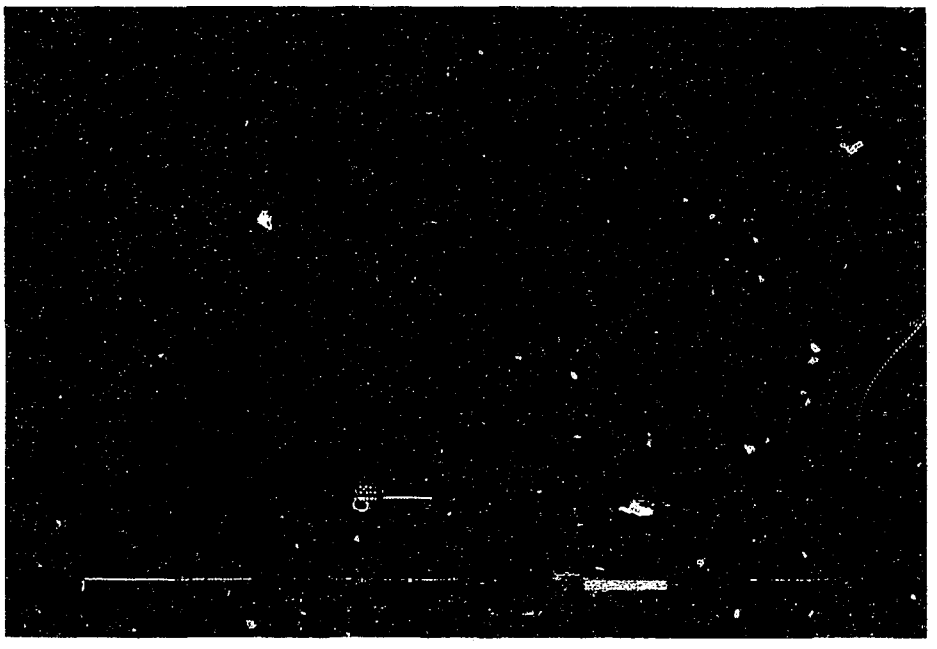

(b)

Fig. 5.7: Finite element simulation of A=60° particle undergoing a backward rotation: (a) The onset of primary impact by the leading edge, (b) the secondary impact by the adjacent edge particle. Material loss in form of metal chips can be clearly seen in (b). Contours are von Misses stresses in Pa.

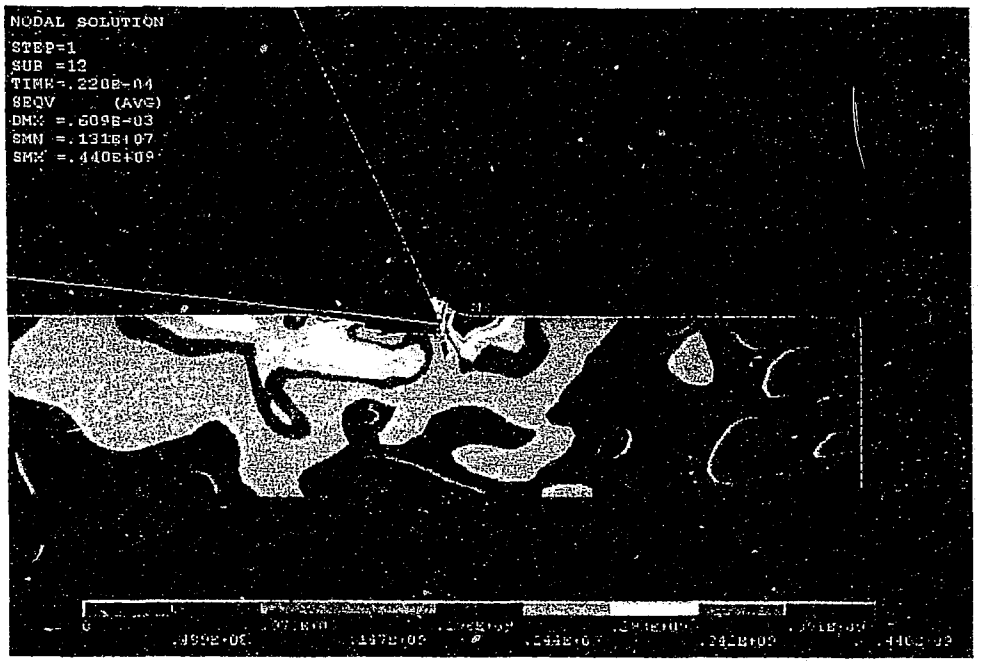

(a)

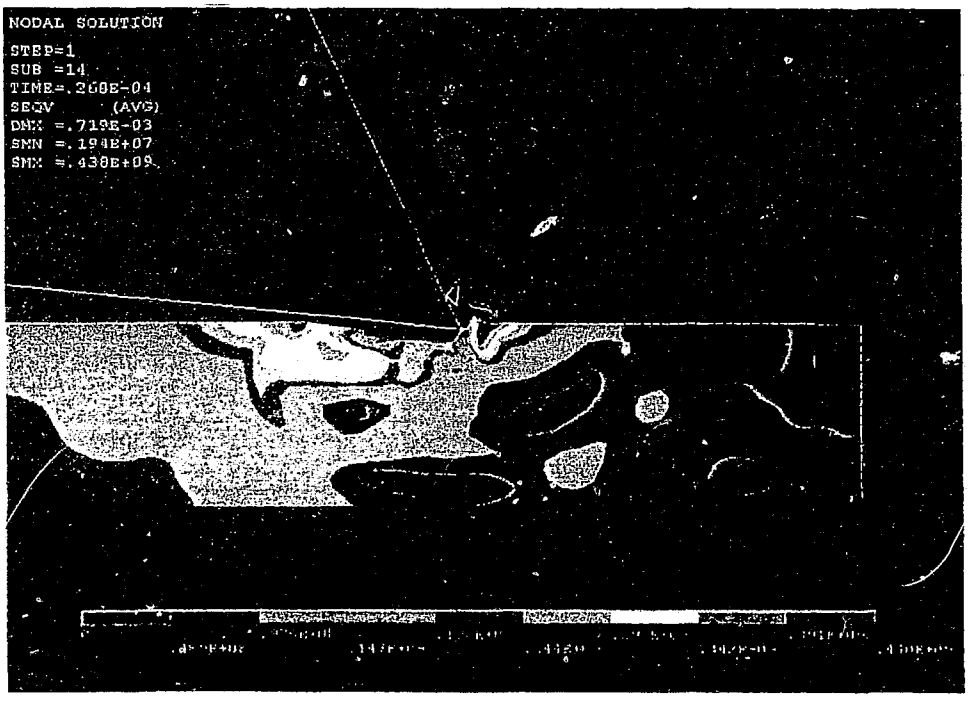

(b)

Fig. 5.8: Finite element simulation of A=60° particle undergoing a backward rotation: (a): Particle "tunnels" below the surface of the target material, (b) Chip "break-off" prior to completion of the cutting action. Contours are von Misses stresses in Pa.

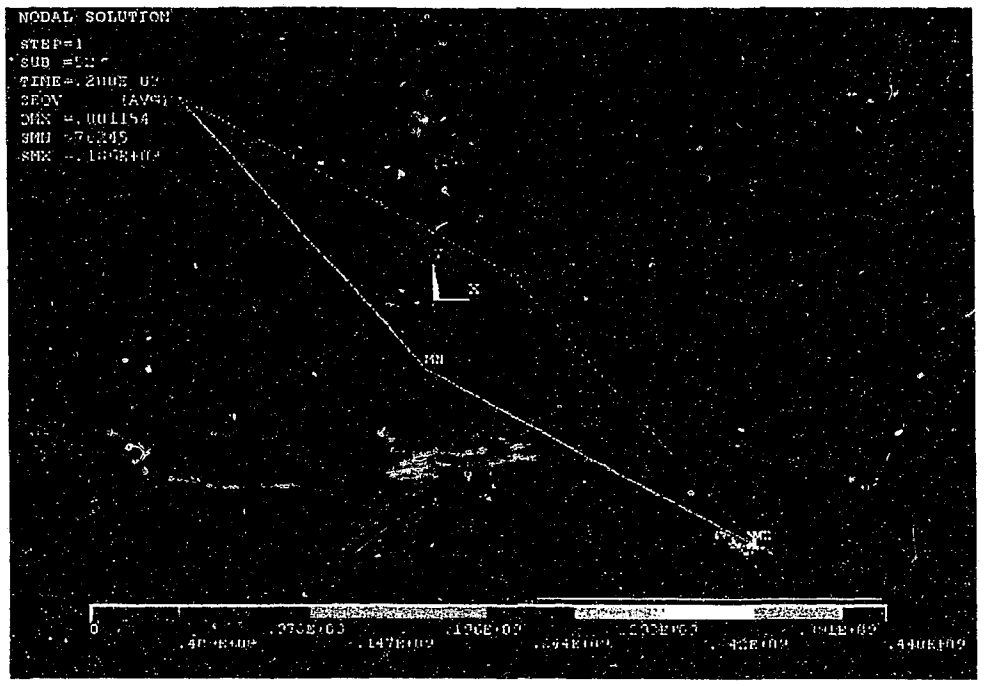

Fig. 5.9: Finite element simulation of A=80° particle "tunnelling" deep inside the target surface.

5.5 Comparison of Finite Element Analysis Results with Experimental and Rigid-Plastic Model Predictions

In this section the finite element analysis results are obtained for various impact conditions for particles with various angularities, and compared with the experimental and model predicted data from chapter 4 .The tables and graphs illustrate the comparison of data. In general, a good agreement is found between the simulated, experimental and finite element analysis results. Because the particular elements chosen in the finite element analysis do not directly give rotational rebound velocity and rebound angle, these quantities are not presented. To measure the crater volumes, the X-Y coordinates of the crater points was plotted in sigma plots (Systat Software Inc Point Richmond, CA) and the area under the curve was directly calculated to give the area of the crater which was multiplied by the respective particle width to give crater volume. Nevertheless, rebound

effectiveness of the finite element method in simulating the impacts. This is borne out by the good agreement of these parameters with experiments.

5.5.1 Rebound Velocity (V_r)

Table 5.2 illustrates the average difference of rebound velocities (V_{reb}) between simulated, experimental and finite element analysis results. A good agreement (i.e. average difference within 15%) is found between the experimental and the finite element results for the general cases of forward and backward rotations, which validates the assumptions made in the finite element model, in particular for dynamic hardness Pd=440MPa (i.e. yield stress σ_0) and failure strain ε_f as described in section 5.2.1.2. Furthermore, the average differences were within 20% in both the cases of A=60° and A= 45° (Table A.23 and Table A.25).

In most of the data in Table-A.23, Table A.25, and Table A.27 (see appendix), it is noteworthy that finite element model results for rebound velocities were higher than the rigid-plastic model predictions for both the cases of forward and backward rotations. However in comparison to the experimental results, it underestimated the rebound velocities. This can be partially explained, based on the elastic and pileup effects discussed in Section 4.5, chapter 4. The finite element model is able to predict the ploughed material at the edge of the craters, as seen in Fig. 5.6.a and Fig. 5.6.b, resulting in an increase in instantaneous contact area between the leading edge of the particle and the target material. This increase in area induces an additional force (and thus velocity) component normal to the surface, which is unaccounted for in the rigid plastic model. In most of the cases, the finite element results are nearer to the experimental results as compared to the rigid plastic model predictions. This is most likely due to the ability of the finite element model to explicitly treat erosion, tunnelling, and chip break off effects. This further adds more credibility to the finite element model selection for the finite element analysis and the respective assumptions made in the model.

Furthermore, the finite element model was able to successfully predict the type of rotation and rebound velocities for impacts at the sensitive transition range, where the particle undergoes transition from forward to backward rotation as defined in section

4.5.4. From the Tables A.26 and A.28, the highest percentage error in the range of 20-30% was reported for impacts near the transition, where, as noted in Chapter 2, the dynamics are very sensitive to the incident parameters.

5.5.2 Crater Dimensions and Volume: Comparison of results between Experimental, Rigid-Plastic Model and Finite Element Analysis

Fig. 5.10 illustrates a typical crater profile predicted by rigid plastic model and finite element model for A=60° particle at identical incident impact conditions. Similarly good results were found for most of the other impact conditions involving forward and backward rotation, and at the transition, but are not presented.

Fig. 5.11 illustrates the crater profile dimensions obtained from experimental, rigid plastic model and finite element analysis results for cases of both forward and backward rotating impacts. Excellent agreement was found for the general shape of the crater profiles, except at the crater edges where the presence of piled up material existed for the experimental and finite element model cases. For simplicity, in Fig. 5.12, the pileup was not plotted.

Finite element analyses were conducted for typical impacts involving both forward and backward rotations and compared with the experimental and rigid-plastic model predictions, as shown in Tables A.23, A.25, A.27, A.29, and A.30. Tables A.24, A.26, and A.28 illustrate the average percentage difference between the crater dimensions. Comparison of crater length (2L) between the finite element model predictions and experimental results did not reveal any clear trend; however in majority of the cases the finite element model overestimated the crater depth δ. This overestimation was also reported for crater volume predictions by the rigid-plastic model, and is probably owing to elastic spring back effects discussed in Section 4.5.4. However, the agreement between the finite element model prediction and experimental result is reasonable, with an average error percentage within 25%.

The crater volume characteristic curves were plotted for A=60° (Fig. 5.12.a) and A=45° (Fig. 5.12.b) particles involved in transition from forward to backward rotation,

from the results of finite element analysis to predict the critical orientation angles (θ_i^{crit}).

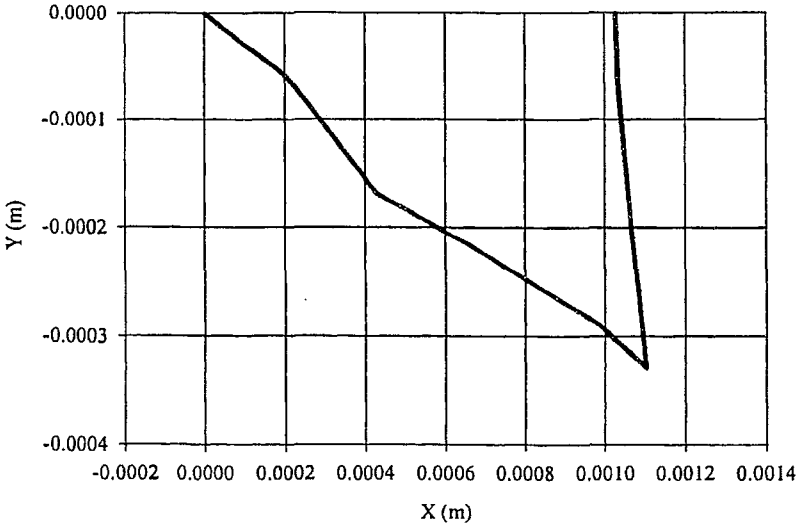

(a)

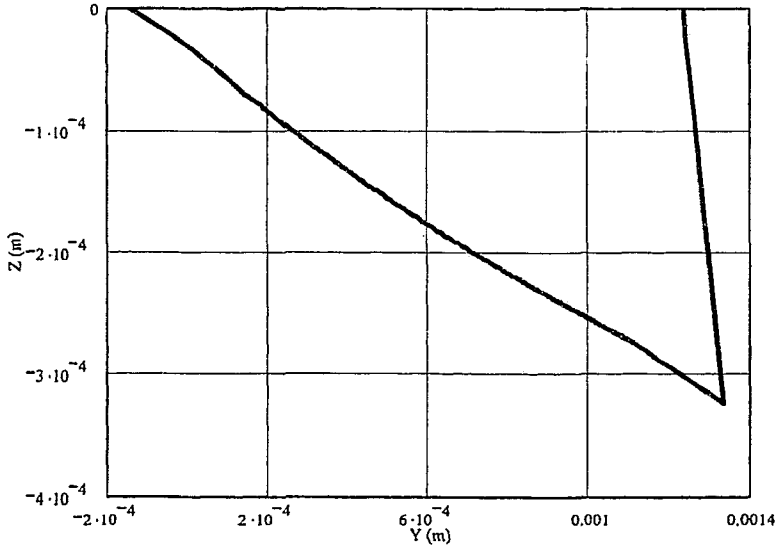

(b)

Fig. 5.10: Crater profile predicted by: (a) finite element model and (b) rigid-plastic model for A=60° particle undergoing forward rotation. The incident impact conditions are: α=33.9°, θ_i=44.71°, V_i=24.4 m/s, $\dot{\theta}_i$ = -170 rad/s

Similar characteristic curve plots were presented in section 4.6.1(chapter 4) for the rigid-plastic model alone. It was seen that at the same critical orientation angles (θ_i^{crit}), the finite element model successfully predicted the transition of the particle from forward to backward rotation.

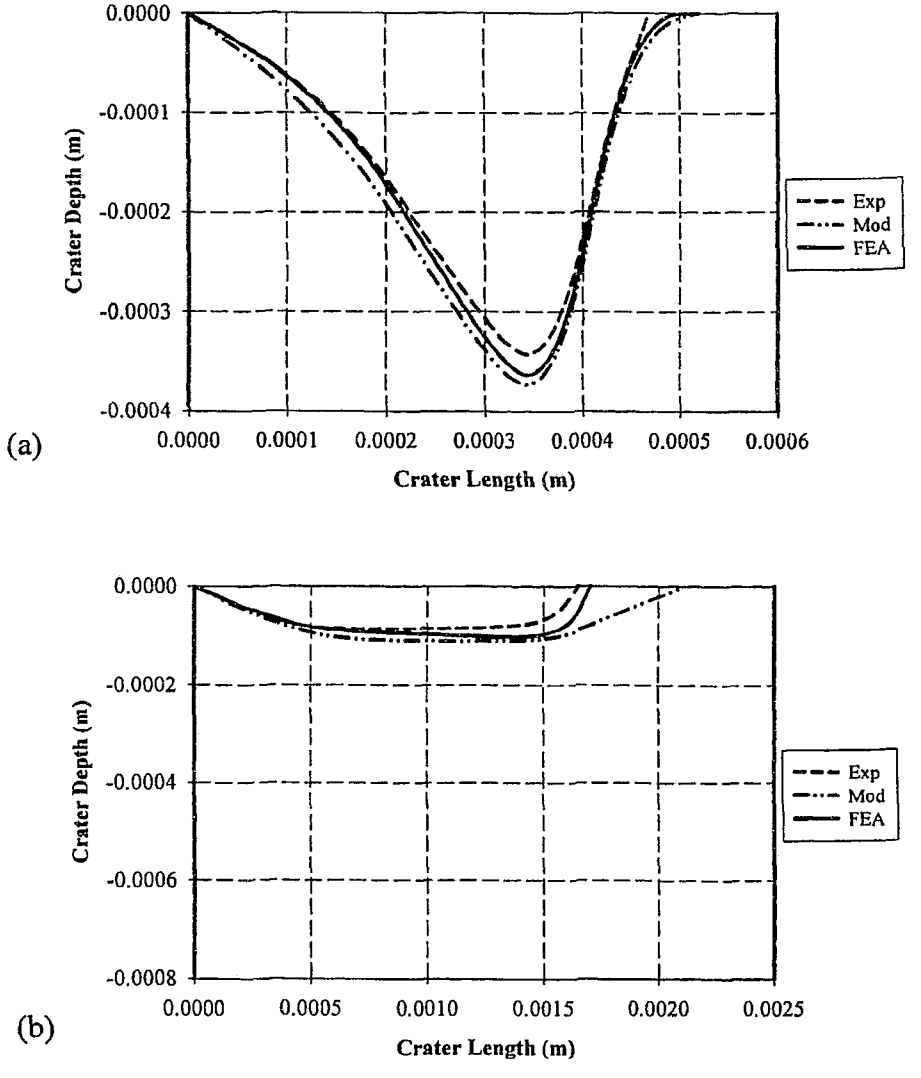

Fig.5.11: Comparison of experimental, rigid-plastic model and finite element model analysis results of crater profiles involving: (a) Forward and (b) Backward rotations. The incident conditions are: (a) α =33.7°, θ_i=11.4 °, V_i=25 m/s, $\dot{\theta}_i$ = 150 rad/s and (b) α =32°, θ_i=51 °, V_i=25 m/s, $\dot{\theta}_i$ = 209 rad/s

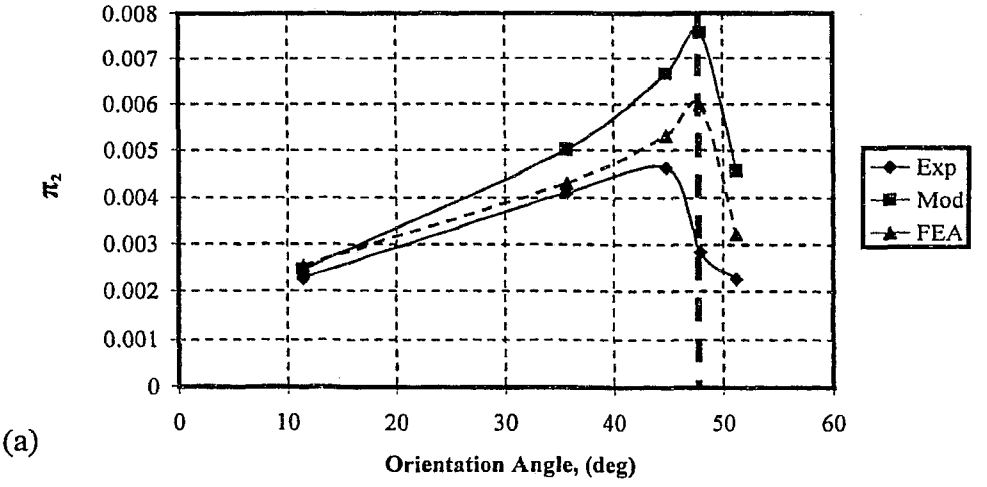

(a)

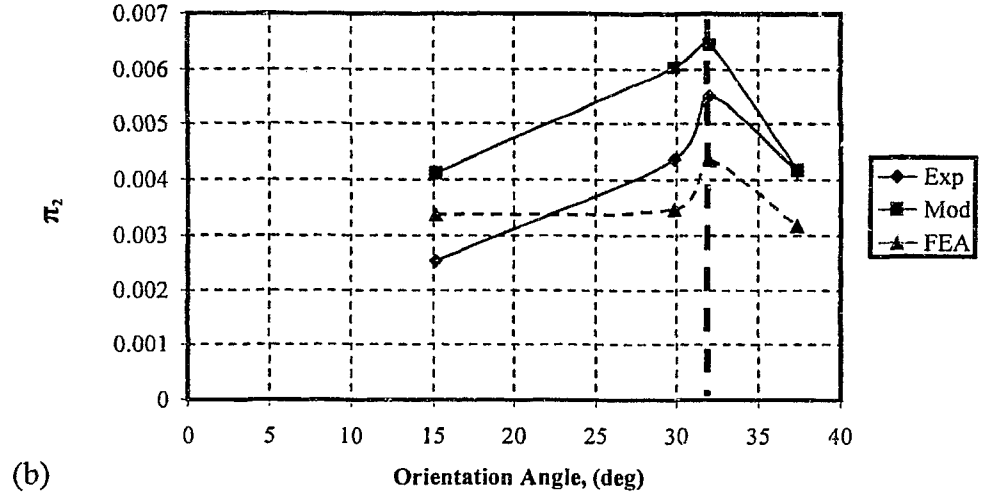

(b)

Fig 5.12: Orientation Angle vs. Dimensionless Crater Volume (π_2) for A=60° particle (Fig 5.13 (a) and A=45° particle (Fig.5.13.b).The data is taken from Table A.29 and Table A.30 respectively The left side of the vertical line indicates forward rotation and the right side indicates backward rotation of the rebounding particle.

5.6 Summary:

The failure strain is the single most important parameter responsible for erosion of the target material, is a function of indentation velocity and depends on the angularity of the particle. The finite element model predicts erosion mechanisms similar to chapter 4 and showed excellent agreement with the experimental results including successful prediction of the transition and conditions of maximum material loss. This adds further credibility in selection of finite element model to simulate erosion mechanisms involving angular particles and the relevant assumptions of failure strains and dynamic hardness.

Chapter-6

Conclusions and Recommendations

6.1 Conclusions

The main conclusions of this thesis can be summarized as follows:

- An experimental apparatus consisting of a catapult-type particle launcher and a high speed digital camera was described and used to measure incident and rebound parameters for impacts of well defined hardened angular steel particles against soft aluminum alloy targets.

- Experimental results were obtained for symmetric angular particles of known shape, size and density colliding with a plastic target (i.e. Aluminium 3003) at arbitrary incident velocity, orientation, and angle of attack.

- Experimental results revealed that, both ploughing resulting from forward rotating particles, and machining, resulting from backwards rotating particles, was identified as the primary erosion mechanisms. The craters formed by the forward rotations were short and deep, whereas the craters formed by the backward rotations were long and shallow. In most of the cases, the backward rotation resulted in multiple impacts; with the leading edge impacting first, followed by the adjacent edge.

- In contrast to previous work with square particles [9], the backward rotating particles were not found to machine a chip to complete removal leaving a smooth cut profile. Instead, the chip was often found to break off prior to completion of the machining action. This is because angular particles, in contrast to square particles, tend to "tunnel" below the surface and "pry out", rather than cut, a chip. The collision kinematics is very sensitive at this point of "chip break–off", which

significantly affects the prediction of orientation angle for the onset of secondary impact. The adjustments to the orientation angle made in the secondary impact cases were well supported by the finite element model predictions which demonstrated "tunneling" and "chip break-off" mechanisms and higher orientation angles for secondary impact.

- Infinite combinations of dynamic hardness and friction coefficient could be obtained to define the resistance of the plastic flow field to indentation in the target material below the impact. Both the strain rate induced by the impacting angular particle, and the friction coefficient, at the contact depend on the local velocity of indentation. Hence, in dynamic impact conditions, no constant value of dynamic hardness could be defined for a type of material, for arbitrary friction coefficients and indentation velocities. In the present study, the value of dynamic hardness was fixed for all the experimental conditions and the friction coefficient was adjusted to match the experimental results. Furthermore, model predictions were also obtained by keeping friction coefficient constant and varying the dynamic hardness. It is noteworthy that no considerable differences between the results were found.

- The experimental data was compared to the predictions of rigid-plastic model developed by Papini and Spelt [2, 3], and finite element model, and very good agreement was found with respect to the collision kinematics, energy losses, crater dimensions and volume of material removed by single angular rigid particle impacting the plastic target. The agreement confirms the validity of the rigid-plastic model and finite element model.

- The rigid-plastic and finite element models were also able to accurately predict the critical orientation angle which defines, for a given incident angle of attack, the transition from forward to backward rotation. This adds further credibility to the rigid-plastic model assumptions and the relative assumptions made in the finite element model. The maximum crater volume occurs at this (θ_i^{crit}). This is supported by the actual data obtained showing maximum energy consumption at

the transition responsible for maximum plastic deformation. Furthermore, for the same orientation angle at identical conditions of impact, the crater volume increases with the increases in angle of attack.

- The spring back effect in the target material and the material pile up at the crater edges is believed to be responsible for discrepancies in the experimental results and model predictions for rebound velocity, rebound angle and crater volumes. The finite element model was able to account for the effects of material pile up, but spring-back was unaccounted for.
- The failure strain criterion significantly influenced the finite element modeling of the erosion mechanism. Because the strain rates in the presently considered angular particle impacts depended on the number of parameters including particle angularity, and the particular tumbling dynamics of the particle, the failure strain could not be considered constant. While a highly angular particle would be expected to travel more rapidly during the impact and the material directly below the impacting particle would thus be subjected to a higher strain rate, the material adjacent to the sides of the particle would be subjected to a lower strain rate, as compared to a less angular particle. Apparently the strain rate seen by the sides is more important, overall.

6.2 Contributions

The main contributions from this work are:

- Experimental set-up and design of the catapult apparatus to launch angular particles with known incident parameters such that the collision occurs in a single (2D) plane. Such experiments have never before been successfully performed.
- Identification of tunneling and chip break-off phenomena in the impacts of highly angular particles. Such behaviour has never been reported before.
- Modeling and fixing the combination of dynamic hardness and friction coefficient for particles with various angularities when impacting a particular material (3003 series aluminum alloy).

- Calculation of particle trajectories, determination of incident orientation angle and orientation angle adjustment for the onset of next impact in multiple impact cases.
- Finite element modeling of single angular particle impacts.
- Introduction of replica casting technique using rubber to measure crater profiles
- Comparison of the experimental data with the predictions of rigid-plastic and finite element model

6.3 Recommendations for Future Work:

- Only one material with one velocity was used in the present work, it would be interesting to explore different materials, differently sized particles, and higher impact velocities. This would verify the dimensional analysis of Papini and Spelt [2, 3], who found the problem would scale.
- Experiments involving backward rotation of 30° and 80° particles are extremely difficult to perform due to difficulties in obtaining 2D planar impacts. Such impacts would, nonetheless, provide useful data.
- The effect of initial rotational velocity is currently a subject of debate in the literature. Use of the rigid plastic and FE models, with verifying experiments could shed some light on this important area. However, modifications to the catapult setup would have to be made so that appreciable rotational velocities could be introduced.
- More finite element analysis work to study rebound angle and rebound angular velocity would give more credibility to its effectiveness.

References

1) I. M. Hutchings, Mechanisms of the erosion of metals by solid particles, Erosion: Prevention and Useful Applications, ASTM STP664, W. F. Adler, Ed., American Society for Testing and Materials , (1979), 59-76.
2) M. Papini and J. K. Spelt, Impact of rigid angular particles with fully plastic targets- Part I: Analysis, International Journal of Mechanical Sciences 42, No. 5 (2000), 991-1006.
3) M. Papini, and J. K. Spelt, Impact of rigid angular particles with fully plastic targets- Part II: Parametric study of erosion phenomena, International Journal of Mechanical Sciences 42, No. 5 (2000), 1007-1025.
4) G. L. Sheldon, and I. Finnie, Trans. ASME J. Eng. Ind., 88 (1966), 393-400.
5) A.W. Ruff, and S.M. Wiederhorn, Erosion by Solid Particle Impact, Treatise on Material Science and Technology, (1979), Vol. 16, 69-126.
6) G. L. Sheldon, Trans. ASME J. Basic Eng., (1970), Vol. 92, 619-626.
7) D. Aquaro, and E. Fontani, Erosion of Ductile and Brittle Materials Meccanica 36 (2001), 651–661.
8) A. G. Evans, M. E Gulden, and M. E Rosenblatt, Proc. R. Soc. London Ser, A 361 (1978), 343-365.
9) I. M. Hutchings, Deformation of metal surfaces by the oblique impact of square plates, International Journal of Mechanical Science, 19 (1977), 45-52.
10) I.M. Hutchings, R. E. Winter, and J. E. Field, Solid particle erosion of metals: the removal of surface material by spherical projectiles, Proceedings of the Royal Society of London, A348 (1976), 379.
11) I.M. Hutchings, N. H. Macmillan, and D. R. Rickerby, Further studies of the oblique impact of a hard sphere against a ductile solid, International Journal of Mechanical Science, 23 (11) (1981), 639-646.
12) I. Finnie, The mechanism of erosion of ductile metals, Proc. 3rd U.S. Nat. Congress of Applied Mechanics, (1958), 527-532.

13) I. Finnie, Erosion of surfaces by solid particles, Wear, 3 (1960), 87-103.

14) G. Sundararajan and P. G. Shewmon, The oblique impact of a hard ball against ductile, semi-infinite, target materials- experiment and analysis, Int. J. Impact Engnrg, 6 (1) (1987), 3-22.

15) Y. Tirupataiah, B. Venkataraman, and G. Sundararajan, The nature of the elastic rebound of a hard ball impacting on ductile, metallic target materials, Materials Science and Engineering, A24 (1990), 133-140.

16) M. Papini and J.K. Spelt, The plowing erosion of organic coatings by spherical particles, Wear, 222 (1998), 38-48.

17) Y.I.Oka, H.Ohnogi, T.Hosokawa, M.Matsumura, The impact angle dependence of erosion damage caused by solid particle impact, Wear, 203-204 (1997), 573-579.

18) G. Sundararajan, The depth of the plastic deformation beneath eroded surfaces: The influence of impact angle and velocity, particle shape and material properties, Wear, I49 (1991), 129-153.

19) G.L. Sheldon, and A. Kanhere, An Investigation of impingement erosion using single particles, Wear 21 (1972) 195-208.

20) D. G. Rickersby and N. H. MacMillan, On the oblique impact of a rigid sphere against a rigid plastic solid, International Journal of Mechanical Science.22 (1980),491-494.

21) R. E. Winter and I.M. Hutchings, Solid Particle Erosion Studies using single Angular Particles, Wear, 29 (1974) 181-194.

22) Y. Tirupataiah and G. Sundararajan, A dynamic indentation technique for the characterization of the high strain rate plastic flow behaviour of ductile metals and alloys, J. Mech. Phys. Solids, 39 (2) (1991), 243-271.

23) J.E. Goodwin, W. Sage, G.P. Tilly, Study of Erosion by Solid Particles, Proc. Of Inst. of Mech. Eng., Vol. 184, (1969-70), 279-291.

24) J. G. A, Bitter, A Study of Erosion Phenomena, Part I and Part II, Wear, Vol. 6 (1963), 5-21 and 169-190.

25) G.L. Sheldon, and I. Finnie, Trans., ASME J. Eng. Ind., (1966), 88, 393-400.

26) Kosel, H. Thomas, Solid Particle Erosion, ASM Handbook, Vol. 18, 199-213.

27) S. Dhar, T. Krajac, D. Ciampini and M. Papini, Erosion mechanisms due to impact of single angular particles, invited paper for ICEAW II, Cambridge, UK, to appear in Wear,(2004).

28) Alan V. Levy, Solid particle erosion and erosion-corrosion of materials, ASM International, (1995).

29) ASM Metals Handbook, Ninth Edition, Vol. 1, Properties and Selection, (1990), 639-663.

30) A.M.S Hamouda and M.S.J Hashmi, Mechanical properties of aluminium metal matrix composites under impact loading, Journal of Materials Processing Technology, 56, (1996), 743-756.

31) Manjit Singh, H.R. Suneja, M.S. Bola, S. Prakash, Dynamic tensile deformation and fracture of metal cylinders at high strain rates, International Journal of Impact Engineering, 27 (2002), 939–954.

32) Rade Vignjevic, Kevin Hughes and Emma A.Taylor, Finite Element Modeling of Failure of a Multi-Material target Due to High Velocity Space Debris impacts, Space Debris 2 (2002), 41–50.

Appendix

Incident Parameters						Rebound Parameters							
						Experimental				Predicted			
Obs.No	α_i (°)	θ_i (°)	V_i (m/s)	$\dot{\theta}_i$ (rad/s)	KE_i (J)	α_r (°)	V_r (m/s)	$\dot{\theta}_r$ (rad/s)	KE Loss (J)	α_r (°)	V_r (m/s)	$\dot{\theta}_r$ (rad/s)	KE Loss (J)
1	29	7.0	24.3	-50	0.266	6	16.0	-3060	0.122	6	16.4	-3110	0.116
2	30	18.9	24.5	-90	0.270	22	13.2	-2440	0.174	19	13.4	-2550	0.169
3	34	12.5	24.8	165	0.277	15	13.4	-2620	0.175	13	14.0	-2640	0.168
4	43	9.8	24.6	-80	0.272	15	12.8	-2400	0.181	12	12.2	-2310	0.189
5	46	12.4	29.8	-170	0.400	18	14.0	-2450	0.293	16	12.7	-2430	0.309
6	50	12.0	24.7	-50	0.275	18	9.8	-1800	0.222	15	9.4	-1785	0.226
7	58	4.8	24.6	-40	0.272	17	9.0	-1510	0.229	9	9.0	-1720	0.227
8	62	6.9	24.6	-30	0.272	20	8.1	-1480	0.236	12	7.0	-1340	0.245
9	*60	-6.2	24.6	-100	0.272	18	11.8	-2260	0.194	19	11.1	-2260	0.201
10	*68	-21.0	25.4	-40	0.290	34	12.1	-2120	0.210	34	11.3	-2030	0.220

Table A.1 - Experimental and predicted results for impacts involving forward rotating particles (A=60 °). Each row represents the average of at least 3 experiments. *The last row indicates a particle that has impacted three times i.e. multiple impacts

Incident Parameters						Rebound Parameters			
						Percentage Error (%)			
Obs.No	**α_i (°)**	**θ_i (°)**	**V_i (m/s)**	**$\dot{\theta}_i$ (rad/s)**	**KE_i (J)**	**α_r (°)**	**V_r (m/s)**	**$\dot{\theta}_r$ (rad/s)**	**KE Loss (J)**
1	29	7	24.3	-50	0.266	0.00	2.44	1.61	5.17
2	30	18.9	24.5	-90	0.27	15.79	1.49	4.31	2.96
3	34	12.5	24.8	165	0.277	15.38	4.29	0.76	4.17
4	43	9.8	24.6	-80	0.272	25.00	4.92	3.90	4.23
5	46	12.4	29.8	-170	0.4	12.50	10.24	0.82	5.18
6	50	12	24.7	-50	0.275	20.00	4.26	0.84	1.77
7	58	4.8	24.6	-40	0.272	88.89	0.00	12.21	0.88
8	62	6.9	24.6	-30	0.272	66.67	15.71	10.45	3.67
9	*60	-6.2	24.6	-100	0.272	5.26	6.31	0.00	3.48
10	*68	-21	25.4	-40	0.29	0.00	7.08	4.43	4.55
Average Percentage Error (%)						$25^{(\dagger)}$	5.6	4	3.6

Table A.2 – Calculation of error percentage for experimental and predicted for impacts involving forward rotation for A=60° particle. Each column in the rebound parameters represents the average percentage error.

Notes: Sample calculation of average percentage error:

$$^{(\dagger)}\ \frac{1}{n}\sum_{i=1}^{n}\left[\left|\frac{\alpha_{r(Model)}-\alpha_{r(Experiment)}}{\alpha_{r(Model)}}\right|*100\right]$$

Incident Parameters						Rebound Parameters			
						Percentage Error (%)			
Obs.No	α_i (°)	θ_i (°)	V_i (m/s)	$\dot{\theta}_i$ (rad/s)	KE_i (J)	α_r (°)	V_r (m/s)	$\dot{\theta}_r$ (rad/s)	KE Loss (J)
1	34	53.5	24.6	70	0.272	140.00	4.88	2.63	8.61
2	40	54.7	25.1	100	0.284	166.67	1.29	0.00	1.71
3	44	51.5	25.7	-30	0.297	114.29	10.32	0.00	6.70
4	46	49.5	25	-50	0.281	136.36	6.45	5.31	4.72
5	49	47.0	25.5	-28	0.293	100.00	12.20	13.48	7.62
6	51	47.0	25.8	70	0.300	133.33	12.70	3.10	9.57
7	53	47.6	30.0	40	0.405	114.29	14.29	5.66	3.35
8	60	38.6	25.9	-150	0.302	6.54	5.00	10.00	2.33
9	60	45.2	26.0	-50	0.304	7.50	50.00	5.26	2.00
Average Percentage Error (%)						102(†)	13	5	5

Table A.4 – Calculation of error percentage for experimental and predicted results involving backwards rotation of particles (multiple impacts) for A=60° particle. Each column in the rebound parameters represents the average percentage error.

(†) see notes presented below Table A.2

Incident Parameters						Rebound Parameters									
						Experimental				Predicted					
Obs.No	α_i (°)	θ_i (°)	V_i (m/s)	$\dot{\theta}_i$ (rad/s)	KE_i (J)	α_r (°)	V_r (m/s)	$\dot{\theta}_r$ (rad/s)	KE Loss (J)	α_r (°)	V_r (m/s)	$\dot{\theta}_r$ (rad/s)	KE Loss (J)	θ^{crit} (°)	Type
1	34	46.3	24.7	180	0.275	51	2.9	-350	0.27	53	3.9	-740	0.267	50	Forward
2	33	51	24.6	239	0.272	12	14.6	140	0.176	5	13.5	200	0.19		Backward
3	36	48	24.6	80	0.277	45	3.8	-410	0.27	56.5	3	-567	0.272	49.3	Forward
4	36	50.5	24.8	66	0.277	3.2	15	450	0.175	5.5	13.7	594	0.192		Backward
5	40	47.6	24.7	40	0.271	55	2	-290	0.268	59	2.3	-420	0.268	48.3	Forward
6	40	49	24.9	40	0.279	18	11.4	80	0.221	6	9.5	220	0.238		Backward
7	44	44	24.5	40	0.27	50	1.8	-230	0.268	53	2.1	-400	0.268	47.3	Forward
8	45	48	24.7	120	0.275	12	6.9	240	0.253	8	5.2	220	0.263		Backward

Table A.5 - Experimental and predicted results for impacts near a transition from forward to backward rotation of A=60° particle. θ_i^{crit} is the predicted critical initial orientation angle for the transition from forward to backward rotation. Each row represents the average of at least 3 experiments.

Incident Parameters						Rebound Parameters				
							Percentage Error (%)			
Obs.No	α_i (°)	θ_i (°)	V_i (m/s)	$\dot{\theta}_i$ (rad/s)	KE_i (J)	Type	α_r (°)	V_r (m/s)	$\dot{\theta}_r$ (rad/s)	KE Loss (J)
1	34	46.3	24.7	180	0.275	Forward	3.77[(†)]	25.64	52.70	1.12
2	33	51	24.6	239	0.272	Backward	140.00	8.15	30.00	7.37
3	36	48	24.6	80	0.277	Forward	20.35	26.67	27.69	0.74
4	36	50.5	24.8	66	0.277	Backward	41.82	9.49	24.24	8.85
5	40	47.6	24.7	40	0.271	Forward	6.78	13.04	30.95	0.00
6	40	49	24.9	40	0.279	Backward	200.00	20.00	63.64	7.14
7	44	44	24.5	40	0.27	Forward	5.66	14.29	42.50	0.00
8	45	48	24.7	120	0.275	Backward	50.00	32.69	9.09	3.80

Table A.6- Calculation of error percentage for experimental and predicted for impacts near a transition from forward to backward rotation for A=60° particle. Each column in the rebound parameters represents the absolute error percentage measured

(†) see notes presented below Table A.2

Incident Parameters				Rebound Parameters											
				Experimental						Predicted					
θ_i (°)	V_i (m/s)	$\dot{\theta}_i$ (rad/s	KE_i (J)	α_r (°)	V_r (m/s)	$\dot{\theta}_r$ (rad/s)	KE Loss (J)	Cr. Vol.[1] mm^3	π_2	α_r (°)	V_r (m/s)	$\dot{\theta}_r$ (rad/s	KE Loss (J)	Cr. Vol.[1] mm^3	π_2
11.42	25.0	150	0.2782	14.48	13.5	-2599	0.1793	0.2560	0.00228	11.89	14.4	-2718	0.1665	0.2754	0.00246
13.68	24.7	180	0.2705	14.49	13.4	-2650	0.1718	0.2200	0.00196	14.41	13.6	-2564	0.1711	0.2890	0.00258
28.20	24.7	120	0.2716	32.40	9.8	-1820	0.2200	0.3900	0.00348	30.90	9.2	-1733	0.2259	0.4630	0.00413
35.60	24.4	155	0.2646	42.40	7.2	-1210	0.2379	0.4600	0.00410	39.56	6.6	-1249	0.2411	0.5640	0.00503
40.12	24.7	189	0.2716	43.12	5.6	-1100	0.2542	0.4700	0.00419	45.04	5.3	-1007	0.2562	0.6640	0.00592
44.71	24.4	160	0.2644	38.95	4.8	-423	0.2537	0.5200	0.00464	50.70	4.0	-764	0.2557	0.7490	0.00668
47.89	24.4	170	0.2644	10.81	3.8	196	0.1796	0.3200*	0.00285	55.49	3.4	-651	0.2581	0.8500*	0.00758
51.19	24.4	260	0.2645	7.54	14.8	164	0.1666	0.2560*	0.00228	5.13	13.6	205	0.1821	0.5130*	0.00458
53.40	24.5	73	0.2681	12.46	17.4	326	0.1324	0.2300*	0.00205	4.51	16.3	330	0.1494	0.2734*	0.00244

Table A.7- Experimental and predicted results for impacts involving transition of rotation from forward to backward rotation of A=60° particle at an average angle of attack, α = 33.8 °. Each row represents the average of at least 3 experiments. The crater volume marked as (*) represents the volume of only the primary crater.

[1] Cr. Vol. (mm^3) - Crater Volume

Incident Parameters				Rebound Parameters					
				Percentage Error (%)					
θ_i (°)	V_i (m/s)	$\dot{\theta}_i$ (rad/s)	KE_i (J)	α_r (°)	V_r (m/s)	$\dot{\theta}_r$ (rad/s)	KE Loss (J)	Cr. Vol.[1] mm^3	π_2
11.42	25	150	0.2782	21.78(†)	6.25	4.38	7.69	7.04	7.32
13.68	24.7	180	0.2705	0.56	1.47	3.35	0.41	23.88	24.03
28.2	24.7	120	0.2716	4.85	6.52	5.02	2.61	15.77	15.74
35.6	24.4	155	0.2646	7.18	9.09	3.12	1.33	18.44	18.49
40.12	24.7	189	0.2716	4.26	5.66	9.24	0.78	29.22	29.22
44.71	24.4	160	0.2644	23.18	20.00	44.63	0.78	30.57	30.54
47.89	24.4	170	0.2644	80.52	305.88	130.11	30.41	62.35	62.40
51.19	24.4	260	0.2645	46.98	8.82	20.00	8.51	50.10	50.22
53.4	24.5	73	0.2681	176.27	6.75	1.21	11.38	15.87	15.98

Table A.8- Calculation of error percentage for experimental and predicted results for impacts involving transition of rotation from forward to backward rotation of A=60° particle at an average angle of attack, α = 33.8 °. Each row represents the average of at least 3 experiments. The crater volume marked as (*) represents the volume of only the primary crater.

[1] Cr. Vol. (mm^3) - Crater Volume
(†) see notes presented below Table A.2

Incident Parameters				Rebound Parameters											
				Experimental						Predicted					
θ_i (°)	V_i (m/s)	$\dot{\theta}_i$ (rad/s)	KE_i (J)	α_r (°)	V_r (m/s)	$\dot{\theta}_r$ (rad/s)	KE Loss (J)	Cr. Vol.[1] mm^3	π_2	α_r (°)	V_r (m/s)	$\dot{\theta}_r$ (rad/s)	KE Loss (J)	Cr. Vol.[1] mm^3	π_2
8.79	24.30	-98	0.2629	13.21	13.28	-2500	0.1676	0.2240	0.00200	10.30	12.40	-2349	0.1796	0.2900	0.00259
10.80	24.80	-53	0.2738	17.04	12.41	-2305	0.1910	0.2560	0.00228	12.80	12.01	-2274	0.1957	0.3208	0.00286
22.50	24.80	-45	0.2738	28.40	9.80	-1820	0.2221	0.3500	0.00312	25.40	9.20	-1740	0.2280	0.4300	0.00384
31.70	25.10	-60	0.2804	40.10	7.00	-1244	0.2545	0.4800	0.00428	36.24	6.10	-1166	0.2602	0.5700	0.00508
40.89	25.27	41	0.2842	52.00	3.53	-750	0.2772	0.6300	0.00562	47.80	3.60	-683	0.2772	0.7500	0.00669
47.25	24.97	35	0.2775	54.30	2.10	-488	0.2749	0.7520	0.00671	57.90	2.40	-451	0.2744	0.9190	0.00820
48.00	24.58	48	0.2689	55.47	1.87	-363	0.2670	0.4800	0.00428	59.47	2.22	-397	0.2663	0.9270	0.00827
48.65	24.97	52	0.2775	19.97	10.50	54	0.2284	0.5120	0.00457	4.32	7.50	57	0.2525	0.8500	0.00758
53.59	24.98	83	0.2778	16.85	14.56	264	0.1832	0.1600	0.00143	5.63	14.98	268	0.1777	0.2300	0.00205
55.10	24.82	105	0.2742	14.07	14.93	521	0.1743	0.1760	0.00157	5.44	15.40	528	0.1679	0.1582	0.00141
55.34	25.47	116	0.2888	16.93	16.31	650	0.1692	0.0900	0.00080	5.52	16.08	652	0.1726	0.1510	0.00135

Table A.9- Experimental and predicted results for impacts involving transition of rotation from forward to backward rotation of A=60° particle at an average angle of attack, $\alpha = 40.8$ °. Each row represents the average of at least 3 experiments.

[1] Cr. Vol. (mm^3) - Crater Volume

Incident Parameters				Rebound Parameters					
				Percentage Error (%)					
θ_i (°)	V_i (m/s)	$\dot{\theta}_i$ (rad/s)	KE_i (J)	α_r (°)	V_r (m/s)	$\dot{\theta}_r$ (rad/s)	KE Loss (J)	Cr. Vol.[1] mm^3	π_2
8.79	24.3	-98	0.2629	28.25(†)	7.10	6.43	6.68	22.76	22.78
10.8	24.8	-53	0.2738	33.13	3.33	1.36	2.40	20.20	20.28
22.5	24.8	-45	0.2738	11.81	6.52	4.60	2.59	18.60	18.75
31.7	25.1	-60	0.2804	10.65	14.75	6.69	2.19	15.79	15.75
40.89	25.27	41	0.2842	8.79	1.94	9.81	0.00	16.00	15.99
47.25	24.97	35	0.2775	6.22	12.50	8.20	0.18	18.17	18.17
48	24.58	48	0.2689	6.73	15.77	8.56	0.26	48.22	48.25
48.65	24.97	52	0.2775	362.27	40.00	5.26	9.54	39.76	39.71
53.59	24.98	83	0.2778	199.29	2.80	1.49	3.10	30.43	30.24
55.1	24.82	105	0.2742	158.64	3.05	1.33	3.81	11.25	11.35
55.34	25.47	116	0.2888	206.70	1.43	0.31	1.97	40.40	40.74

Table A.10- Calculation of error percentage for experimental and predicted results for impacts involving transition of rotation from forward to backward rotation of A=60° particle at an average angle of attack, α = 40.8 °. Each row represents the average of at least 3 experiments. The crater volume marked as (*) represents the volume of only the primary crater.

[1.] Cr. Vol. (mm^3) - Crater Volume
(†) see notes presented below Table A.2

Incident Parameters				Rebound Parameters											
				Experimental						Predicted					
θ_i (°)	V_i (m/s)	$\dot{\theta}_i$ (rad/s)	KE_i (J)	α_r (°)	V_r (m/s)	$\dot{\theta}_r$ (rad/s)	KE Loss (J)	Cr. Vol.[1] mm^3	π_2	α_r (°)	V_r (m/s)	$\dot{\theta}_r$ (rad/s)	KE Loss (J)	Cr. Vol.[1] mm^3	π_2
6.90	24.6	-27	0.2694	20.20	8.1	-1480	0.2346	0.2560	0.00228	11.51	7.0	-1339	0.2426	0.3800	0.00339
11.90	25.2	-120	0.2827	15.87	7.3	-1287	0.2549	0.3520	0.00314	16.80	6.4	-1222	0.2603	0.4400	0.00393
23.50	25.3	-85	0.2849	38.78	3.0	-514	0.2803	0.4300	0.00384	31.90	2.6	-493	0.2812	0.5600	0.00500
28.60	25.3	-100	0.2838	38.40	2.1	-247	0.2817	0.4580	0.00409	42.53	1.1	-195	0.2832	0.6000	0.00535
37.66	25.9	-128	0.2991	160.00	1.8	379	0.2973	0.5760	0.00514	-30.39	1.8	302	0.2973	0.7800	0.00696
39.50	25.9	-167	0.2991	165.00	2.3	406	0.2964	0.5120	0.00457	-25.55	2.3	414	0.2963	0.8190	0.00731
43.44	25.9	-89	0.2991	27.98	4.0	294	0.2917	0.7800	0.00696	-13.82	3.6	252	0.2932	0.9260	0.00826
47.02	26.0	-14	0.3009	36.50	5.0	514	0.2891	0.5760	0.00514	-26.28	2.5	515	0.2974	0.7042	0.00628
50.76	26.1	53	0.3021	32.73	6.9	662	0.2797	0.3520	0.00314	19.20	4.2	670	0.2928	0.3900	0.00348

Table A.11- Experimental and predicted results for impacts involving transition of rotation from forward to backward rotation of A=60° particle at an average angle of attack, α = 60 °. Each row represents the average of at least 3 experiments. The crater volume marked as (*) represents the volume of only the primary crater.

[1.] Cr. Vol. (mm^3) - Crater Volume

Incident Parameters				Rebound Parameters					
				Percentage Error (%)					
θ_i (°)	V_i (m/s)	$\dot{\theta}_i$ (rad/s)	KE_i (J)	α_r (°)	V_r (m/s)	$\dot{\theta}_r$ (rad/s)	KE Loss (J)	Cr. Vol.[1] mm^3	π_2
6.9	24.6	-27	0.2694	75.50(†)	15.71	10.53	3.30	32.63	32.74
11.9	25.2	-120	0.2827	5.54	14.06	5.32	2.07	20.00	20.10
23.5	25.3	-85	0.2849	21.57	15.38	4.26	0.32	23.21	23.20
28.6	25.3	-100	0.2838	9.71	90.91	26.67	0.53	23.67	23.55
37.66	25.9	-128	0.2991	626.49	0.00	25.50	0.00	26.15	26.15
39.5	25.9	-167	0.2991	745.79	0.00	1.93	0.03	37.48	37.48
43.44	25.9	-89	0.2991	302.46	11.11	16.67	0.51	15.77	15.74
47.02	26	-14	0.3009	238.89	100.00	0.19	2.79	18.21	18.15
50.76	26.1	53	0.3021	70.47	64.29	1.19	4.47	9.74	9.77

Table A.12- Calculation of error percentage for experimental and predicted results for impacts involving transition of rotation from forward to backward rotation of A=60° particle at an average angle of attack, α = 60.0 °. Each row represents the average of at least 3 experiments. The crater volume marked as (*) represents the volume of only the primary crater.

[1.] Cr. Vol. (mm^3) - Crater Volume
(†) see notes presented below Table A.2

Incident Parameters						Rebound Parameters							
						Experimental				Predicted			
Obs.No	α_i (°)	θ_i (°)	V_i (m/s)	$\dot{\theta}_i$ (rad/s)	KE_i (J)	α_r (°)	V_r (m/s)	$\dot{\theta}_r$ (rad/s)	KE Loss (J)	α_r (°)	V_r (m/s)	$\dot{\theta}_r$ (rad/s)	KE Loss (J)
1	35.31	28.0	25.6	-364	0.301	35.49	8.25	-2135	0.2468	28.72	9.7	-2412	0.243
2	45.53	33.5	25.3	-430	0.285	41.9	3.22	-700	0.279	40.7	3.84	-946	0.276
3	47.62	30.2	25.6	-327	0.292	45.0	4.75	-1086	0.278	36.3	4.20	-1030	0.281
4	47.65	15.2	25.3	-250	0.285	21.5	9.10	-2187	0.235	18.7	8.41	-2119	0.241
5	48.00	33.0	25.1	-430	0.281	45.0	5.64	-1360	0.261	41.0	3.20	-800	0.274
6	48.15	29.8	25.2	-261	0.283	36.7	3.87	-947	0.273	36.6	3.83	-940	0.274
7	48.22	25.3	25.1	-288	0.281	33.4	5.50	-1409	0.262	30.5	5.35	-1332	0.263
8	48.50	32.0	25.2	-336	0.283	42.3	4.10	-900	0.273	39.4	3.27	-798	0.276
9	49.00	30.0	25.5	-250	0.290	43.2	4.89	-1150	0.275	36.0	3.70	-910	0.281
10	60.33	15.0	25.4	-318	0.287	32.0	5.60	-1482	0.267	19.8	5.01	-1264	0.271
11	68.06	10.7	25.4	-421	0.287	29.0	5.12	-1440	0.269	14.0	4.70	-1176	0.273

Table A.13 - Experimental and predicted results for impacts involving forward rotating particles for A=45° particle. Each row represents the average of at least 3 experiments.

Incident Parameters						Rebound Parameters			
						Percentage Error (%)			
Obs.No	α_i (°)	θ_i (°)	V_i (m/s)	$\dot{\theta}_i$ (rad/s)	KE_i (J)	α_r (°)	V_r (m/s)	$\dot{\theta}_r$ (rad/s)	KE Loss (J)
1	35.31	28	25.6	-364	0.301	23.57	14.95	11.48	1.56
2	45.53	33.5	25.3	-430	0.285	16.15	2.95	26.00	1.09
3	47.62	30.2	25.6	-327	0.292	13.10	23.97	5.44	1.07
4	47.65	15.2	25.3	-250	0.285	8.20	14.97	3.21	2.49
5	48.00	33	25.1	-430	0.281	76.25	9.76	70.00	4.74
6	48.15	29.8	25.2	-261	0.283	1.04	0.27	0.74	0.36
7	48.22	25.3	25.1	-288	0.281	2.80	9.51	5.78	0.38
8	48.50	32	25.2	-336	0.283	25.38	7.36	12.78	1.09
9	49.00	30	25.5	-250	0.29	32.16	20.00	26.37	2.14
10	60.33	15	25.4	-318	0.287	11.78	61.62	17.25	1.48
11	68.06	10.7	25.4	-421	0.287	8.94	107.14	22.45	1.47
Average Percentage Error (%)						20(†)	24	18	1.6

Table A.14– Calculation of error percentage for experimental and predicted for impacts involving forward rotating particles (A=45°) Each column in the rebound parameters represents the average percentage error.

1. Cr. Vol. (mm^3) - Crater Volume
(†) see notes presented below Table A.2

Incident Parameters						Rebound Parameters								
						Experimental				Predicted				
Obs.No	α_i (°)	θ_i (°)	V_i (m/s)	$\dot{\theta}_i$ (rad/s)	KE_i (J)	α_r (°)	V_r (m/s)	$\dot{\theta}_r$ (rad/s)	KE Loss (J)	α_r (°)	V_r (m/s)	$\dot{\theta}_r$ (rad/s)	KE Loss (J)	θ_{adj} (°)
1	35.56	39.86	25.5	-147	0.2895	5.97	16.2	45	0.1727	6.80	18.9	47	0.1305	-42.23
2	37.50	36.45	25.4	-362	0.2875	9.15	17.1	329	0.1568	7.24	15.6	347	0.1789	-43.75
3	41.64	35.12	25.4	-291	0.2878	6.80	14.7	221	0.1915	7.20	11.8	285	0.2254	-43.80
4	42.53	37.12	25.3	-265	0.2855	13.87	18.0	550	0.1404	10.22	16.3	498	0.1666	-42.92
5	46.22	38.20	25.3	-253	0.2842	14.00	12.2	480	0.2173	11.07	16.2	573	0.1665	-43.20
6	46.41	37.40	25.3	-348	0.2852	14.40	12.0	460	0.2206	10.06	15.8	493	0.1735	-43.00
7	46.84	38.00	25.2	-361	0.2819	14.50	11.8	455	0.2194	12.90	15.2	500	0.1784	-43.00
8	47.40	37.82	25.2	-315	0.2834	13.50	11.2	500	0.2269	11.20	15.4	558	0.1766	-43.00
9	49.18	36.48	25.5	-411	0.2899	28.09	15.8	1248	0.1746	16.80	15.0	1330	0.1850	-44.83

Table A.15 - Experimental and predicted results for impacts involving backwards rotating particles (multiple impacts) for A=45° particle. Note the adjustment on the orientation angle, θ_{adj} (°) for the secondary impact. Each row represents the average of at least 3 experiments.

Incident Parameters						Rebound Parameters			
						Percentage Error (%)			
Obs.No	α_i (°)	θ_i (°)	V_i (m/s)	$\dot{\theta}_i$ (rad/s)	KE_i (J)	α_r (°)	V_r (m/s)	$\dot{\theta}_r$ (rad/s)	KE Loss (J)
1	35.56	39.86	25.5	-147	0.2895	12.21	14.29	4.26	32.34
2	37.5	36.45	25.4	-362	0.2875	26.38	9.62	5.19	12.35
3	41.64	35.12	25.4	-291	0.2878	5.56	24.58	22.46	15.04
4	42.53	37.12	25.3	-265	0.2855	35.71	10.43	10.44	15.73
5	46.22	38.2	25.3	-253	0.2842	26.47	24.69	16.23	30.51
6	46.41	37.4	25.3	-348	0.2852	43.14	24.05	6.69	27.15
7	46.84	38	25.2	-361	0.2819	12.40	22.37	9.00	22.98
8	47.4	37.82	25.2	-315	0.2834	20.54	27.27	10.39	28.48
9	49.18	36.48	25.5	-411	0.2899	67.20	5.33	6.17	5.62
Average Percentage Error (%)						27.6(†)	18	10	21

Table A.16 – Calculation of Error percentage for experimental and predicted results involving backwards rotating particles (multiple impacts) of A=45°. Each column in the rebound parameters represents the average percentage error.

1. Cr. Vol. (mm^3) - Crater Volume
(†) see notes presented below Table A.2

Incident Parameters				Rebound Parameters											
				Experimental						Predicted					
θ_i (°)	V_i (m/s)	$\dot{\theta}_i$ (rad/s)	KE_i (J)	α_r (°)	V_r (m/s)	$\dot{\theta}_r$ (rad/s)	KE Loss (J)	Cr. Vol.[1] mm^3	π_2	α_r (°)	V_r (m/s)	$\dot{\theta}_r$ (rad/s)	KE Loss (J)	Cr. Vol.[1] mm^3	π_2
15.20	25.3	-250	0.285	21.50	9.1	-2187	0.2353	0.2820	0.00254	18.75	8.4	-2119	0.2415	0.4556	0.00411
25.30	25.1	-288	0.281	33.40	5.5	-1409	0.2622	0.4312	0.00389	30.50	5.4	-1332	0.2635	0.5870	0.00529
29.85	25.2	-261	0.283	36.72	3.9	-947	0.2739	0.4844	0.00437	36.62	3.8	-940	0.2741	0.6682	0.00603
30.00	25.5	-250	0.290	43.20	4.2	-1150	0.2786	0.5208	0.00470	36.00	3.7	-910	0.2817	0.6862	0.00619
32.00	25.2	-336	0.283	42.30	3.8	-900	0.2744	0.6110	0.00551	39.41	3.3	-798	0.2765	0.7145	0.00644
33.00	25.1	-430	0.281	45.00	4.1	-1360	0.2686	0.5900	0.00532	41.00	3.2	-800	0.2747	0.7311	0.00659
33.50	25.3	-430	0.285	41.97	3.2	-700	0.2791	0.6030	0.00544	40.77	3.8	-946	0.2760	0.7400	0.00667
37.40	25.3	-348	0.285	14.40	12.0	460	0.2203	0.4604	0.00415	10.06	15.8	493	0.1732	0.4637	0.00418
37.82	25.2	-315	0.283	13.50	11.2	500	0.2265	0.3254	0.00293	11.20	15.4	558	0.1763	0.3664	0.00330
38.00	25.2	-361	0.282	14.50	11.8	455	0.2195	0.4018	0.00362	12.90	15.2	500	0.1785	0.3507	0.00316

Table A.17- Experimental and predicted results for impacts involving transition of rotation from forward to backward rotation of A=45° particle at an average angle of attack, $\alpha = 47.5$ °. Each row represents the average of at least 3 experiments.

[1.] Cr. Vol. (mm^3) - Crater Volume

Incident Parameters				Rebound Parameters					
				Percentage Error (%)					
θ_i (°)	V_i (m/s)	$\dot{\theta}_i$ (rad/s)	KE_i (J)	α_r (°)	V_r (m/s)	$\dot{\theta}_r$ (rad/s)	KE Loss (J)	Cr. Vol.[1] mm^3	π_2
15.2	25.3	-250	0.285	14.67(†)	8.33	3.21	2.57	38.10	38.20
25.3	25.1	-288	0.281	9.51	1.85	5.78	0.49	26.54	26.47
29.8	25.2	-261	0.283	0.27	2.63	0.74	0.07	27.51	27.53
30.0	25.5	-250	0.29	20.00	13.51	26.37	1.10	24.10	24.07
32.0	25.2	-336	0.283	7.33	15.15	12.78	0.76	14.49	14.44
33.0	25.1	-430	0.281	9.76	28.13	70.00	2.22	19.30	19.27
33.5	25.3	-430	0.285	2.94	15.79	26.00	1.12	18.51	18.44
37.4	25.3	-348	0.285	43.14	24.05	6.69	27.19	0.71	0.72
37.8	25.2	-315	0.283	20.54	27.27	10.39	28.47	11.19	11.21
38.0	25.2	-361	0.282	12.40	22.37	9.00	22.97	14.57	14.56

Table A.18- Calculation of Error percentage for experimental and predicted results for impacts involving transition of rotation from forward to backward rotation of A=45° particle at an average angle of attack, $\alpha = 47.5$ °. Each row represents the average of at least 3 experiments. The crater volume marked as (*) represents the volume of only the primary crater.

[1.] Cr. Vol. (mm^3) - Crater Volume
(†) see notes presented below Table A.2

Incident Parameters						Rebound Parameters									
						Experimental					Predicted				
Obs. No	α_i (°)	θ_i (°)	V_i (m/s)	$\dot{\theta}_i$ (rad/s)	KE_i (J)	α_r (°)	V_r (m/s)	$\dot{\theta}_r$ (rad/s)	KE Loss (J)	Crater Volume (mm^3)	α_r (°)	V_r (m/s)	$\dot{\theta}_r$ (rad/s)	KE Loss (J)	Crater Volume (mm^3)
1	24.0	44.6	26.3	-924	0.398	26.8	9.2	-1004	0.34	0.7732	51.6	10.0	-961	0.332	0.7971
2	38.3	50.0	22.3	-465	0.280	30.7	3.5	-361.5	0.272	0.9894	63.9	2.6	-238	0.276	1.1921
3	38.3	10.9	19.7	-834	0.225	31.2	13.0	-1200	0.115	0.0969	12.7	12.8	-1235	0.117	0.1113
4	50.0	30.9	23.6	-465	0.315	53.4	5.0	-286	0.300	0.3627	41.5	4.3	-415	0.303	0.4650
5	30.0	47.0	25.2	-546	0.359	36.2	10.5	-1009	0.287	0.3467	57.2	7.0	-670	0.327	0.3940
6	35.0	45.0	23.0	-423	0.298	50.1	6.2	-346	0.275	0.5973	55.8	5.2	-497	0.280	0.7964
7	44.0	34.0	23.8	-323	0.225	45.9	6.0	-487	0.202	0.4920	41.6	5.4	-515	0.206	0.6000
8	28.0	22.0	24.1	-421	0.328	28.3	15.9	-1276	0.169	0.1909	25.1	14.3	-1382	0.193	0.2766
9	46.0	14.7	23.3	-330	0.306	22.1	9.5	-1143	0.241	0.2498	19.7	10.5	-1018	0.233	0.3046
10	33.0	19.3	24.6	-450	0.341	28.7	14.5	-1421	0.202	0.2350	22.9	14.0	-1350	0.212	0.2937

Table A.19 - Experimental and predicted results for impacts involving forward rotating particles (A=80 °). Each row represents the average of at least 3 experiments.

Incident Parameters						Rebound Parameters				
						Percentage Error (%)				
Obs.No	α_i (°)	θ_i (°)	V_i (m/s)	$\dot{\theta}_i$ (rad/s)	KE_i (J)	α_r (°)	V_r (m/s)	$\dot{\theta}_r$ (rad/s)	KE Loss (J)	Crater Volume (mm^3)
1	24.0	44.6	26.3	-924	0.398	8.18	4.4	48.06	2.37	3.00
2	38.3	50.0	22.3	-465	0.28	37.7	51.6	51.89	1.48	17.00
3	38.3	10.9	19.7	-834	0.225	1.51	2.83	146.21	1.61	13.00
4	50.0	30.9	23.6	-465	0.315	16.2	31.08	28.58	0.89	22.00
5	30.0	47.0	25.2	-546	0.359	49.6	50.6	36.75	12.24	12.00
6	35.0	45.0	23.0	-423	0.298	20.5	30.38	10.22	1.93	25.00
7	44.0	34.0	23.8	-323	0.225	11.1	5.44	10.34	1.72	18.00
8	28.0	22.0	24.1	-421	0.328	11.1	7.67	12.66	12.48	31.00
9	46.0	14.7	23.3	-330	0.306	9.4	12.28	12.11	3.55	18.00
10	33.0	19.3	24.6	-450	0.341	3.7	5.26	25.03	4.9	20.00
Average Percentage Error (%)						38.1(†)	16.9	20.1	4.3	17.9

Table A.20– Calculation of Error percentage for experimental and predicted for impacts involving forward rotating particles (A=80°). Each column in the rebound parameters represents the average percentage error.

Incident Parameters						Rebound Parameters									
						Experimental					Predicted				
Obs. No	α_i (°)	θ_i (°)	V_i (m/s)	$\dot{\theta}_i$ (rad/s)	KE_i (J)	α_r (°)	V_r (m/s)	$\dot{\theta}_r$ (rad/s)	KE Loss (J)	Crater Volume (mm^3)	α_r (°)	V_r (m/s)	$\dot{\theta}_r$ (rad/s)	KE Loss (J)	Crater Volume (mm^3)
1	55.9	14.0	25.5	-100.0	0.293	43.2	8.0	-1134.0	0.260	0.4232	36.5	7.3	-934.0	0.266	0.5643
2	57.8	9.6	25.5	-120.0	0.293	32.3	7.2	-1411.0	0.263	0.3646	25.0	6.7	-1480.0	0.266	0.5209
3	60.3	12.2	26.2	-150.0	0.308	45.8	6.9	-1055.0	0.283	0.4252	34.3	6.6	-905.0	0.286	0.5906
4	62.3	10.8	26.2	-112.0	0.310	38.8	7.1	-1156.0	0.283	0.3579	31.8	6.0	-940.0	0.291	0.5867
5	64.7	12.7	25.9	-282.0	0.302	42.3	5.8	-940.0	0.284	0.4563	38.8	5.7	-540.0	0.286	0.6004
6	67.2	10.8	27.0	-235.0	0.382	48.0	4.5	-730.0	0.371	0.4174	35.4	5.3	-618.0	0.315	0.6422
7	70.9	8.0	27.3	-87.3	0.382	55.0	5.5	-830.4	0.366	0.4649	30.8	4.2	-648.0	0.319	0.6368
8	72.9	6.0	26.5	-87.5	0.316	47.2	3.7	-892.0	0.307	0.4533	25.1	3.6	-769.0	0.308	0.5887
9	73.3	8.9	26.2	-78.0	0.310	42.9	3.2	-345.0	0.304	0.5048	37.7	3.5	-288.0	0.304	0.6010
10	75.3	6.6	26.5	-108.0	0.316	31.0	3.5	-585.0	0.309	0.5262	31.0	3.1	-498.0	0.310	0.5979
11	77.2	5.2	26.4	-103.0	0.314	30.7	3.0	-543.0	0.309	0.4406	27.6	2.7	-527.0	0.312	0.5875

Table A.21 - Experimental and predicted results for impacts involving forward rotating particles (A=30°). Each row represents the average of at least 3 experiments.

Incident Parameters						Rebound Parameters				
						Percentage Error (%)				
Obs.No	α_i (°)	θ_i (°)	V_i (m/s)	$\dot{\theta}_i$ (rad/s)	KE_i (J)	α_r (°)	V_r (m/s)	$\dot{\theta}_r$ (rad/s)	KE Loss (J)	Crater Volume (mm^3)
1	55.9	14.0	25.5	-100.0	0.293	18.41	9.59	21.41	2.26	25.00
2	57.8	9.6	25.5	-120.0	0.293	29.20	8.23	4.66	1.13	30.00
3	60.3	12.2	26.2	-150.0	0.308	33.53	5.03	16.57	1.05	28.00
4	62.3	10.8	26.2	-112.0	0.310	21.86	18.67	22.98	2.75	39.00
5	64.7	12.7	25.9	-282.0	0.302	9.02	1.75	74.07	0.70	24.00
6	67.2	10.8	27.0	-235.0	0.382	35.59	15.09	18.12	17.78	35.00
7	70.9	8.0	27.3	-87.3	0.382	78.57	31.57	28.15	14.73	27.00
8	72.9	6.0	26.5	-87.5	0.316	88.20	2.49	15.99	0.32	23.00
9	73.3	8.9	26.2	-78.0	0.310	13.79	7.43	19.79	0.00	16.00
10	75.3	6.6	26.5	-108.0	0.316	0.00	12.90	17.47	0.32	12.00
11	77.2	5.2	26.4	-103.0	0.314	11.09	11.11	3.04	0.96	25.00
Average Percentage Error (%)						30.8(†)	11.8	22	3.8	25.8

Table A.22– Calculation of Error percentage for experimental and predicted for impacts involving forward rotating particles (A=30°). Each column in the rebound parameters represents the average percentage error.

1. Cr. Vol. (mm^3) - Crater Volume
(†) see notes presented below Table A.2

Incident Parameters						Rebound Parameters											
						Experimental				Predictions				FEA			
							Crater				Crater				Crater			
Obs No.	A (deg)	α_i (°)	θ_i (°)	V_i (m/s)	$\dot{\theta}_i$ (rad/s)	V (m/s)	2L mm	δ mm	Vol. mm^3	V (m/s)	2L mm	δ mm	Vol. mm^3	V (m/s)	2L mm	δ mm	Vol. mm^3	Type of Rotation
1	60	58.6	4.6	24.6	-40	9.0	0.440	0.418	0.332	9.0	0.490	0.435	0.354	8.9	0.415	0.355	0.290	Forward
2	60	29.0	7.0	24.3	-50	16.0	0.378	0.260	0.142	16.3	0.429	0.315	0.190	15.2	0.404	0.279	0.161	Forward
3	60	34.0	46.3	24.7	180	2.9	1.040	0.229	0.751	3.9	1.300	0.294	0.850	3.8	0.954	0.260	0.794	Forward
4	45	45.5	33.5	25.3	-430	2.9	1.194	0.156	0.421	3.5	1.730	0.165	0.741	3.1	1.426	0.188	0.554	Forward
5	45	68.1	10.7	25.4	-421	5.1	0.721	0.350	0.430	4.1	0.839	0.380	0.480	5.1	0.647	0.321	0.355	Forward
6	30	64.8	12.7	25.9	-282	5.8	1.150	0.210	0.506	5.6	1.300	0.270	0.615	5.9	1.200	0.245	0.562	Forward
7	30	72.9	6.0	26.5	-88	3.7	1.178	0.312	0.578	3.7	1.181	0.319	0.613	4.4	1.107	0.304	0.536	Forward
8	80	24.0	44.6	26.3	-924	9.2	0.624	0.720	0.760	10.0	0.600	0.832	0.809	5.7	0.816	0.756	0.956	Forward
9	80	38.3	50.0	22.3	-465	3.5	0.693	0.480	0.710	2.5	0.730	0.710	1.008	4.0	0.712	0.590	0.820	Forward
10*	45	35.6	39.9	25.5	-147	16.2	0.723	0.085	0.187	18.9	1.039	0.071	0.219	19.3	0.510	0.098	0.158	Backward
11*	45	49.2	36.5	25.5	-411	15.8	2.100	0.114	0.581	15.0	3.000	0.120	0.610	12.0	1.500	0.170	0.450	Backward
12*	60	44.0	51.5	25.7	-30	13.9	1.421	0.114	0.298	12.6	1.900	0.131	0.390	14.2	1.100	0.145	0.335	Backward

Table A.23 – Finite Element Analysis (FEA), experimental and Rigid-plastic model results for impacts involving both forward and backward rotation of particles. Each row represents the average of at least 3 experiments. *In the last 3 rows, measurement of crater dimensions resulted from the primary impacts only.

Obs. No	Average Error Percentage Difference (%)							
	Velocity		Crater Length (2L)		Crater Depth (δ)		Crater Volume (mm^3)	
	Exp.-FEA[1]	Model-FEA[2]	Exp.-FEA	Model-FEA	Exp.-FEA	Model-FEA	Exp.-FEA	Model-FEA
1	1.01	0.56	6.15	18.21	17.68	22.47	14.82	22.18
2	5.54	7.59	6.39	6.34	6.81	13.05	11.90	17.97
3	22.63	2.63	9.01	36.27	11.92	13.08	5.39	7.05
4	6.45	13.55	16.27	21.32	17.20	12.42	24.01	33.72
5	0.39	19.29	11.44	29.68	9.03	18.38	21.13	35.21
6	1.07	4.25	4.17	8.33	14.29	10.20	9.96	9.43
7	16.48	16.03	6.41	6.68	2.63	4.80	7.84	14.40
8	60.73	74.30	23.53	26.47	4.76	10.05	20.50	15.38
9	12.06	37.69	2.67	2.53	18.64	20.34	13.41	22.93
10	15.93	1.92	41.76	103.73	13.27	28.06	18.35	38.61
11	31.67	25.00	40.00	100.00	32.94	29.41	29.11	35.56
12	2.11	11.27	29.18	72.73	21.38	9.86	11.04	16.42
Average Error Percentage Difference	14.67‡	17.84‡	16.42	36.02	14.21	16.01	15.62	22.40

Table A.24 – Calculation of error percentage difference between experimental, FEA, and rigid- plastic models involving data from Table A.23.

Notes: The average percentage difference measured is given by

[1] For average percentage difference between Experimental and FEA results, (Exp.-FEA) = abs [Experimental -FEA)/FEA *100]
[2] For average percentage difference between Model and FEA results, (Mod-FEA) = abs [Model -FEA)/FEA *100]

‡ The approx error percentage difference (%) given in column#2 and column#3 is calculated as:

$$\frac{1}{n}\sum_{i=1}^{n}(Exp - FEA) \qquad \text{(b)}\ \frac{1}{n}\sum_{i=1}^{n}(Mod - FEA)$$

Incident Parameters					Rebound Parameters												
					Experimental				Predictions				FEA				
						Crater				Crater				Crater			
Obs No.	α_i (°)	θ_i (°)	V_i (m/s)	$\dot{\theta}_i$ (rad/s)	V (m/s)	2L mm	δ mm	Vol. mm^3	V (m/s)	2L mm	δ mm	Vol. mm^3	V (m/s)	2L mm	δ mm	Vol. mm^3	Type of Rotation
1	33.8	11.4	25.0	150	13.5	0.513	0.343	0.256	14.4	0.524	0.374	0.275	13.5	0.518	0.363	0.268	Forward
2	33.8	35.6	24.4	155	7.2	0.790	0.395	0.460	6.6	0.840	0.405	0.564	7.4	0.790	0.396	0.483	Forward
3	33.8	44.7	24.4	160	4.8	1.104	0.315	0.520	4.0	1.380	0.325	0.749	4.0	1.031	0.323	0.596	Forward
4	33.8	47.9	24.4	170	3.8	1.500	0.155	0.320	3.4	1.840	0.244	0.850	3.2	1.100	0.209	0.670	Forward
5*	33.8	51.2	24.4	260	14.8	1.600	0.086	0.250	13.6	2.108	0.108	0.510	14.6	1.700	0.100	0.360	Backward

Table A.25 – Finite Element Analysis (FEA), experimental and rigid-plastic model results for A=60° particle involved in transition from forward to backward rotation. *The last row indicates the measurement of crater dimensions resulted from the primary impact only.

Obs. No	Average Percentage Difference (%)							
	Velocity		Crater Length (2L)		Crater Depth (δ)		Crater Volume (mm^3)	
	Exp.-FEA[1]	Model-FEA[2]	Exp.-FEA	Model-FEA	Exp.-FEA	Model-FEA	Exp.-FEA	Model-FEA
1	0.00	6.67	0.97	1.16	5.51	3.03	4.48	2.61
2	2.70	10.81	0.00	6.33	0.25	2.27	4.76	16.77
3	20.00	0.00	7.08	33.85	2.48	0.62	12.75	25.67
4	18.75	6.25	36.36	67.27	25.84	16.75	52.24	26.87
5*	1.37	6.85	5.88	24.00	14.00	8.00	30.56	41.67
Average Error Percentage Difference	8.56‡	6.12‡	10.06	26.52	9.62	6.13	20.96	22.72

Table A.26- Calculation of error percentage difference between experimental and FEA (finite element model) results and rigid- plastic model and FEA results involving data from Table A.25. *The last row indicates the measurement of crater dimensions resulted from the primary impact only.

The average percentage difference measured is given by

[1] For average percentage difference between Experimental and FEA results, (Exp.-FEA) = abs [Experimental -FEA)/FEA *100]
[2] For average percentage difference between Model and FEA results, (Mod-FEA) = abs [Model -FEA)/FEA *100]

‡ The approx error percentage difference (%) given in column#2 and column#3 is calculated as:

$$\frac{1}{n}\sum_{i=1}^{n}(Exp-FEA) \qquad \text{(b)}\ \frac{1}{n}\sum_{i=1}^{n}(Mod-FEA)$$

Incident Parameters					Rebound Parameters												
					Experimental				Predictions				FEA				
						Crater				Crater				Crater			
Obs No.	α_i(°)	θ_i(°)	V_i (m/s)	$\dot{\theta}_i$ (rad/s)	V (m/s)	2L mm	δ mm	Vol. mm^3	V (m/s)	2L mm	δ mm	Vol. mm^3	V (m/s)	2L mm	δ mm	Vol. mm^3	Type of Rotation
1	47.5	15.2	25.3	-250	9.1	0.623	0.299	0.282	8.4	0.833	0.355	0.456	8.1	0.647	0.318	0.372	Forward
2	47.5	29.9	25.2	-261	3.9	0.689	0.267	0.484	3.8	1.038	0.270	0.668	3.7	0.653	0.259	0.383	Forward
3	47.5	32.0	25.2	-336	3.8	1.490	0.198	0.611	3.3	1.660	0.215	0.715	5.4	0.967	0.252	0.480	Forward
4*	47.5	37.4	25.3	-348	12.0	0.956	0.101	0.460	15.8	1.120	0.112	0.464	16.4	0.820	0.114	0.350	Backward

Table A.27 – Finite Element Analysis (FEA), experimental and rigid-plastic model results for A=45° particle involved in transition from forward to backward rotation. *In the last row, measurement of crater dimensions resulted from the primary impact only.

Obs. No	Average Percentage Difference (%)							
	Velocity		Crater Length (2L)		Crater Depth (δ)		Crater Volume (mm^3)	
	Exp.-FEA[1]	Model-FEA[2]	Exp.-FEA	Model-FEA	Exp.-FEA	Model-FEA	Exp.-FEA	Model-FEA
1	12.90	4.22	11.87	17.82	6.04	11.64	24.09	22.64
2	5.41	2.70	5.54	7.20	3.09	4.25	11.85	27.89
3	29.37	38.66	22.13	26.23	21.51	14.68	11.09	24.45
4*	26.96	3.83	16.61	36.59	11.32	1.67	31.54	32.49
Average Error Percentage Difference	18.66‡	12.35‡	14.04	21.96	10.49	8.06	19.64	26.87

Table A.28- Calculation of error percentage difference between experimental, FEA, and rigid- plastic models involving data from Table A.27.
* In the last row, measurement of crater dimensions resulted from the primary impact only.

See notes presented below Table. A.26

Incident Parameters					Rebound Parameters						
					Experiment		Predicted		FEA		
Obs No.	α_i (°)	θ_i (°)	V_i (m/s)	$\dot{\theta}_i$ (rad/s)	Vol. mm^3	π_2	Vol. mm^3	π_2	Vol. mm^3	π_2	Type of Rotation
1	33.8	11.4	25.0	150	0.256	0.0022	0.275	0.0024	0.286	0.0026	Forward
2	33.8	35.6	24.4	155	0.460	0.0041	0.564	0.0050	0.483	0.0043	Forward
3	33.8	44.7	24.4	160	0.520	0.0046	0.749	0.0066	0.596	0.0053	Forward
4#	33.8	47.8	24.4	170	0.320	0.0028	0.850	0.0075	0.670	0.0060	Forward
5*	33.8	51.1	24.4	260	0.256	0.0022	0.513	0.0045	0.360	0.0032	Backward

Table A.29 –Crater volume results for experimental, rigid-plastic model, and Finite Element Analysis (FEA) for A=60° particle involved in an impact close to the transition from forward to backward rotation.

Data for particle at the transition

* Measurement of crater dimensions resulted from the primary impact only.

Incident Parameters					Rebound Parameters						
					Experiment		Predicted		FEA		
Obs No.	α_i (°)	θ_i (°)	V_i (m/s)	$\dot{\theta}_i$ (rad/s)	Vol. mm^3	π_2	Vol. mm^3	π_2	Vol. mm^3	π_2	Type of Rotation
1	47.5	15.2	25.3	-250	0.282	0.0025	0.4556	0.0041	0.3715	0.0034	Forward
2	47.5	29.8	25.2	-261	0.484	0.0043	0.6682	0.0060	0.3825	0.0035	Forward
3	47.5	32.0	25.2	-336	0.611	0.0055	0.7145	0.0064	0.4800	0.0043	Forward
4*	47.5	37.4	25.3	-348	0.460	0.0041	0.4637	0.0041	0.3500	0.0032	Backward

Table A.30 –Crater volume results for Experimental, rigid-plastic model and Finite Element Analysis (FEA) results for A=45° particle involved in an impact close to the transition from forward to backward rotation.

*Measurement of crater dimensions resulted from the primary impact only.